HZG REPORT 2011-5 // ISSN 2191-7833

Modeling of deformation-induced twinning and dislocation slip in Magnesium using a variationally consistent approach

(Von der Technischen Fakultät der Christian-Albrechts-Universität zu Kiel als Dissertation angenommene Arbeit)

M. Homayonifar

wissen
schafft
nutzen

Helmholtz-Zentrum
Geesthacht
Zentrum für Material- und Küstenforschung

HZG REPORT 2011-5

Modeling of deformation-induced twinning and dislocation slip in Magnesium using a variationally consistent approach

(Von der Technischen Fakultät der Christian-Albrechts-Universität zu Kiel als Dissertation angenommene Arbeit)

M. Homayonifar

Helmholtz-Zentrum Geesthacht
Zentrum für Material- und Küstenforschung GmbH | Geesthacht | 2011

Die HZG Reporte werden kostenlos abgegeben.
HZG Reports are available free of charge.

Anforderungen/Requests:

Helmholtz-Zentrum Geesthacht
Zentrum für Material- und Küstenforschung GmbH
Bibliothek/Library
Max-Planck-Straße 1
21502 Geesthacht
Germany
Fax.: +49 4152 87-1717

Druck: HZG-Hausdruckerei

Als Manuskript vervielfältigt.

ISSN 2191-7833

Helmholtz-Zentrum Geesthacht
Zentrum für Material- und Küstenforschung GmbH
Max-Planck-Straße 1
21502 Geesthacht
www.hzg.de

Abstract

The present thesis is concerned with the analysis of micromechanical deformation systems of single crystal magnesium. For this purpose, a variationally consistent approach based on energy minimization is proposed. It is suitable for the modeling of crystal plasticity at finite strains including phase transition associated with deformation-induced twinning. The method relies strongly on the variational structure of crystal plasticity theory, i.e., an incremental minimization principle can be derived which allows to determine the unknown slip rates by computing the stationary conditions of a pseudo-potential. Phase transition associated with twinning is modeled in a similar fashion. More precisely, a solid-solid phase transition corresponding to twinning is assumed, if this is energetically favorable. Accordingly, two models for twinning phase transition are proposed. Within the first model, twinning phase transition is approximated by means of a pseudo-dislocation. The deformation induced by twinning is decomposed into the reorientation of the crystal lattice and pure shear strain. The latter is assumed to be governed by means of a standard Schmid-type plasticity law, while the reorientation of the crystal lattice is applied when the part of the Helmholtz energy characterizing the pseudo-dislocation system reaches a certain threshold value. Furthermore, a novel and more physically realistic model is developed by which the microstructure of twinning (twinning lamellas) and the related plastic shear strain are obtained from relaxing a certain energy potential. This local model is based on the sequential lamination of the deformation field. Moreover, a size effect is accounted for by considering the twinning interface energy. The proposed models are calibrated for single crystal magnesium by means of the channel die test. Comparisons of the predicted numerical results to their experimental counterparts show that the novel models are able to capture the characteristic mechanical response of magnesium very well.

Kurzfassung

Das Ziel der vorliegenden Arbeit ist die mikromechanische Beschreibung von Magnesium. Hierzu werden verschiedene variationell konsistente Ansätze basierend auf Energieprinzipien vorgeschlagen. Beide dieser Ansätze beschreiben Versetzungen mittels der Kristallplastizität. Im Gegensatz dazu unterscheiden sich die Methoden bezüglich der Modellierung verformungsinduzierter Zwillingsbildung signifikant. Im Rahmen des ersten Modells wird die Deformation, welche zu einer Zwillingsbildung korrespondiert, in der ersten Phase durch eine Scherdeformation und in der zweiten Phase durch eine Reorientierung des Kristallgitters zerlegt. Im Gegensatz hierzu werden beide Mechanismen (Scherdeformation und Reorientierung des Kristallgitters) im zweiten Ansatz simultan betrachtet. Darüber hinaus erlaubt das zweite erweiterte Modell, die Mikrostruktur vorherzusagen, welche mit der Zwillingsbildung einhergeht (z.B. die Dicke der Lamellen). Dadurch ist es möglich, einen Größeneffekt vom Typ Hall-Petch konsistent in das Modell zu integrieren.

Acknowledgments

The current thesis is the report of the research which was carried out from June 2008 until September 2010 at GKSS research centre in Geesthacht. This could not have been accomplished within this short period of time without the smart supervision, extensive support and help of my supervisor, Prof. Jörn Mosler. I would like to express my sincere gratitude to him.

I am indebted to Dr. Dirk Steglich and Prof. Wolfgang Brocks who introduced me to the field of materials modeling and simulation. I deeply appreciate their support, help and trust.

During my research at Institute of Material Research, I had the chance to meet other outstanding scientists, discuss with them and learn many essential concepts which are implicitly contributed in this thesis. I thank Prof. Norbert Huber, Dr. Erica Lilleodden, Dr. Jan Bohlen and Dr. Dietmar Letzig.

I would like to thank all members of the department of simulation of solids and structures and appreciate their help, specially Mr. Mintesnot Nebebe Mekonen, Dr. Ingo Scheider, Dr. Olaf Kintzel, Dr. Radan Radulovic, Mr. Shehzad Saleem Khan and Dr. Serkan Ertürk.

I am also grateful to the examination committee, Prof. Andreas Menzel, Prof. Otto T. Bruhns, Prof. Klaus Rätzke and Prof. Franz Faupel.

Last but not least, I thank my family and specially my wife Maryam, whose support, encouragement and understanding were the spiritual potentials of doing this work.

Contents

1 Introduction

During the early years of the twenty-first century, the efficiency of energy consumption has become more important than ever before, given the demand for energy has been increased tremendously. While renewable sources of energy are under investigation, advances in the structural design and materials make it possible to spend less energy for the same duty. Particularly, in transportation industries, e.g. urban transportation, aerospace and street vehicles, the application of lighter and more durable materials becomes highlighted. Aluminum, titanium and magnesium have been successfully used in aerospace industries. However, the fact that these materials have been considered being expensive has tended to obscure their importance in car production industries. The cost of production is a relative value and hence, the increase in price of energy and a simultaneous reduction in the cost of massive production of magnesium (compared to polymer based composites) make it a prospective candidate to be extensively used in modern cars.

Magnesium challenges aluminum with regard to the relative strength. However, since the discovery of the magnesium element, it was observed that pure magnesium bears a significant chemical potential. For instance, at room temperature it reacts easily with oxygen and hence its applications have been limited to non-engineering structures, e.g. the traditional magnesium fire starter. In sharp contrast to the chemical properties, the physical properties of magnesium are favorable for alloying purpose. Zinc, zirconium, cerium, silver and aluminum are widely used to stabilize and enhance the chemical and mechanical properties of magnesium alloys. Though die cast and sand cast magnesium products satisfy their service requirements, wrought products such as extruded profiles and rolled sheets are also necessary in car production.

The application of wrought magnesium alloys necessitates a comprehensive knowledge about the behavior of such materials during forming processes and their final performance under service load. While the former process is associated with plastic properties, the latter is usually related to reversible elastic deformation. Most of such processes are also visible in pure magnesium. Since this is a less complicated material system, it will be considered in what follows. The material response of single crystal magnesium, in turn, is directly originated from micro-scale phenomena where a complex set of deformation systems governs the overall macro-scale plastic deformation. In general, dislocation slip and deformation-induced twinning contribute to plastic deformation

in magnesium. Unlike traditional aluminum alloys and a wide variety of steels, both mechanisms can have a significant influence on the overall plastic deformation. Most of currently available and frequently used models for irreversible deformations in metals deal with either dislocation slip or deformation-induced twinning. In the present work, novel numerical models are proposed such that both deformation mechanisms are unified in one integrated approach. One advantage of such kind of model is that the instantaneous hardening transition in magnesium can be described. Moreover, while the robustness of the proposed model is taken as a key parameter, the thermodynamical consistency is assured by using a variational energy minimization method. Moreover, the twinning microstructure is analyzed – particularly, the evolution of twinning lamellas.

1.1 State of the art

1.1.1 Experimental observations

In contrast to aluminum with face-centered cubic (FCC) crystal structure and iron with body-centered cubic (BCC) structure, the HCP crystal structure of magnesium has a reduced number of energetically favorable dislocation systems. More precisely, considering a reference lattice axial ratio of c/a = 1.633, magnesium with c/a=1.624 falls into the so-called *transition class*, refer to Christian & Mahajan (1995). The small difference to the reference lattice results in a complex mechanical interplay between dislocation slip and deformation-induced twinning. This has been observed in several experiments, see Hauser et al. (1955); Reed-Hill & Robertson (1957b); Yoshinaga & Horiuchi (1963); Tegart (1964); Wonsiewicz & Backofen (1967); Roberts & Partridge (1966); Obara et al. (1973) and Ando & Tonda (2000).

Although some of the characteristic deformation modes in single crystal magnesium are reasonably well understood such that the basal systems $\langle 11\bar{2}0\rangle\{0001\}$ (Miller-Bravais indexing system for HCP lattices) and the prismatic systems $\langle 11\bar{2}0\rangle\{\bar{1}100\}$ are mostly responsible for plastic deformation, many questions are still open and controversially discussed in the literature. For instance, although it is commonly accepted that twinning is activated in single crystal magnesium at the planes $\{\bar{1}012\}$ under tensile loading in $\langle 10\bar{1}1\rangle$ direction, not much is known about the opposite loading direction. According to Wonsiewicz & Backofen (1967), twinning has been observed in this case as well. However, pyramidal slip on the system $\langle 11\bar{2}3\rangle\{11\bar{2}2\}$ has also been frequently reported, see Obara et al. (1973); Lilleodden (2010).

While only little information is available about the qualitative mechanical response, even less is known about the quantitative behavior of single crystal

magnesium. One effective way to get some further insight is provided by the so-called *channel die test*, see Wonsiewicz & Backofen (1967); Kelley & Hosford (1968) (cf. Sue & Havner (1984)). By using different crystal orientations within that test, classes of specific deformation systems can be enforced allowing to compute the respective hardening behavior (resolved shear stress vs. strain). However, except for rather simple deformation modes showing only a small number of active slip systems, significant further research is still required. For instance, it is completely unknown for complex loading conditions, whether the twinned domain inherits dislocations corresponding to the initial phase, or if only a certain part of them is transformed.

1.1.2 Numerical models

An effective constitutive framework suitable for the modeling of dislocation slip was presented in the pioneering works Hill (1966); Rice (1971); Asaro & Rice (1977): *crystal plasticity theory*. In the late 90s, a variationally consistent reformulation of that theory was elaborated in Ortiz & Repetto (1999) (see also Carstensen et al. (2002); Miehe & Lambrecht (2003); Mosler & Bruhns (2009b)). This thermodynamically sound approach represents the foundation for the novel model which is discussed in the present thesis. In contrast to conventional plasticity-like models, the approach advocated in Ortiz & Repetto (1999) allows to compute unknown dislocation slip rates by minimizing a certain energy functional. Considering rate-independent problems, this potential turns out to be the stress power. In addition to its physical and mathematical elegance, the model proposed in Ortiz & Repetto (1999) shows also some numerical advantages. For instance, the determination of the set of active slip systems (see Peirce et al. (1982)) is naturally included within the aforementioned optimization problem and thus, a visco-plastic-type relaxation such as utilized in Asaro (1983); Asaro & Needleman (1985) or other sophisticated regularization techniques similar to those in Schmidt-Baldassari (2003); McGinty & McDowell (2006); Zamiri et al. (2007); Graff et al. (2007) can often be avoided.

Nowadays, a large number of (local) crystal plasticity theories suitable for the analysis of dislocation slip can be found in the literature. The reader is referred to Roters et al. (2010) for a recent overview. The opposite is true for the modeling of deformation-induced twinning and the coupling of the aforementioned deformation modes. Early attempts to combine twinning with dislocation slip were based on the concept of *pseudo-dislocation* (also referred to as PD-twinning), see e.g. Chin (1975) and references cited therein. Conceptually, only the plastic shear strain caused by twinning has been accounted within such approaches.

First ideas related to the modeling of the reorientation of the crystal lattice due to deformation-induced twinning were addressed in Van Houtte (1978). Physically more sound descriptions of twinning as a kind of phase transformation can be credited to the work Ericksen (1979). Therein, phase transformation is modeled by means of the theory of invariance groups of atomic lattices and the energy associated with their distortion, cf. Rajagopal & Srinivasa (1995). An elegant approximation of the kinematics associated with twinning goes back to James (1981), where Hadamard-like compatibility conditions were derived, see also Pitteri (1985); Ball & James (1987). According to James (1981), the deformation shows a weak discontinuity (discontinuous strain field) at the twin symmetry plane. More precisely, the deformation gradients on both sides of that plane differ from one another by a rank-one second-order tensor, cf. James (1981). As a consequence, twinning can be considered as a certain rank-one convexification (Ortiz & Repetto, 1999; Carstensen et al., 2002). This framework is nowadays well established for mechanical problems involving phase transformation. A typical example is the martensitic phase transformation occurring in shape memory alloys (Ball & James, 1987; Simha, 1997; Mueller, 1999; Idesman et al., 2000; James & Hane, 2000; Mielke et al., 2002). In these works, the aforementioned transition is modeled by means of a rank-one convexification. Physically speaking, phase decomposition occurs within the cited models, if this is energetically favorable. Preliminary ideas to translate the underlying ideas into the modeling of deformation-induced twinning can be found in Kochmann & Le (2009).

1.2 Scope of the thesis

Within the present thesis, a thermodynamically consistent model suitable for the analysis of the fully coupled problem of dislocation slip and twinning is advocated. Though the discussed framework can be applied to a broad range of different materials, the focus is on magnesium. In line with Ortiz & Repetto (1999) and Kochmann & Le (2009), the proposed approach is based on energy minimization, i.e., that particular combination between deformation-induced twinning and dislocation slip is chosen which minimizes the stress power. However, and in sharp contrast to Kochmann & Le (2009), a fully three-dimensional setting and a geometrically exact description (finite strains) is considered. Furthermore, all slip systems important for the mechanical description of single crystal magnesium are taken into account. For the modeling of the phase transition associated with twinning, a novel approximation is discussed. Starting with a numerically very expensive rank-one convexification similar to those adopted in Ball & James (1987); Simha (1997); Mueller (1999); Idesman et al. (2000); James & Hane (2000); Mielke et al. (2002), the deformation induced by twinning is decomposed into a re-

orientation of the crystal lattice and pure shear. The latter is assumed to be governed by a standard Schmid-type plasticity law (pseudo-dislocation), while the reorientation of the crystal lattice is considered, when the respective plastic shear strain reaches a certain threshold value, cf. Staroselsky & Anand (2003). The underlying idea is in line with experimental observations where dislocation slip within the twinned domain is most frequently seen, if the twin laminate reaches a critical volume. It will be shown that the resulting model predicts a stress-strain response in good agreement with that of a rank-one convexification method, while showing the same numerical efficiency as a classical Taylor-type approximation. Consequently, it combines the advantages of both limiting cases. The model is calibrated for single crystal magnesium by means of the channel die test. Moreover, using a viscos approximation of the variational rate-independent crystal plasticity model within finite element framework, the deformation behavior and the texture evolution in a polycrystal is analyzed.

The versatility of the variational model allows to study the twinning microstructure further. In this line, the twinning microstructure is modeled based on the theory of sequential lamination. Since the physics of twinning deformation differs from dislocation slip, the traditional multiplicative decomposition of deformation does not seem to be the proper choice anymore. Accordingly, the kinematics of twinning will be described by an enhanced multiple multiplicative decomposition of the total deformation gradient. The combination of the variational model, relaxation theory and multiple multiplicative decomposition of deformation leads to a robust material model suitable for analyzing the twinning deformation, not only for magnesium alloys, but also for wider range of materials experiencing diffusion-less phase transitions. The evolution of the twinning microstructure is also investigated by considering the twinning interface energy and the energy associated with the configuration misfit of the twinning lamellas. In this regard, minimizing the stress power leads to the characterization of the energetically most favorable twinning laminate microstructure.

1.3 Structure of the thesis

In order to get insight into the physics of the problem, Chapter 2 is devoted to a brief introduction to lattice defects and deformation mechanisms responsible for irreversible deformation of metallic materials. The mathematical description of deformation is given in Chapter 3 including a concise review of thermodynamic laws which assemble the backbone of the proposed variational model. Based on these physical fundaments, constitutive theories are given in Chapter 4. The existence and uniqueness of the solution of the resulting variational

minimization problem are discussed separately in Chapter 5. It is shown that these conditions are directly related to convexity of the respective energy functional. It will be shown that one definition of convexity (rank-one convexity) is closely related to microstructures observed in ductile crystals such as those in copper and magnesium. Based on energy minimization this microstructure depending on the twinning interface energy will be analyzed in Chapter 6. It will be also shown in this chapter that a certain type of interface energy enforces an instantaneous phase transition. By combining a suitable interface energy with the concept of pseudo-dislocation, twinning transformation is modeled in an efficient manner. The numerical implementation of this model, together with its variational re-formulation, are also discussed in Chapter 6. Chapter 7 addresses the numerical procedure of the calibration of the respective material parameters based on experimentally obtained results of the channel die test of single crystal magnesium. Using the calibrated material parameters the deformation behavior and the texture evolution of a polycrystal is analyzed within a finite element framework in Chapter 8. The energy relaxation model described in Chapter 6 is further developed in Chapter 9 where it is shown that the twinning microstructure can be mathematically interpreted as sequential laminates. Based on this interpretation the evolution of microstructures associated with deformation-induced twinning can be analyzed in a more detailed way. Particularly, the thickness of twinning laminates can be predicted.

2 Fundamental mechanisms of micro-scale deformation

All substances are made of discrete units (atoms). Based on the electromagnetic properties of atoms, they pack together in different arrangements. At the macro-scale, the physical state of a material (gas, liquid, solid or meta-phase) and their properties depend on these arrangements. Molecular materials can constitute rather complex microstructures. However, at the macro-scale, all properties are averaged and they can be classified as those with individual atoms.

Metallic materials constitute a subgroup of solid state materials. With the advent of the x-ray technique, the visualization of atomic structures revealed the origin of symmetric properties of metallic materials. It turned out that the macro-scale structure of solid metals is an array of unit cells repeating periodically in three dimensions. The common unit cells in metallic materials are cubic and hexagonal, see Fig. 2.1.

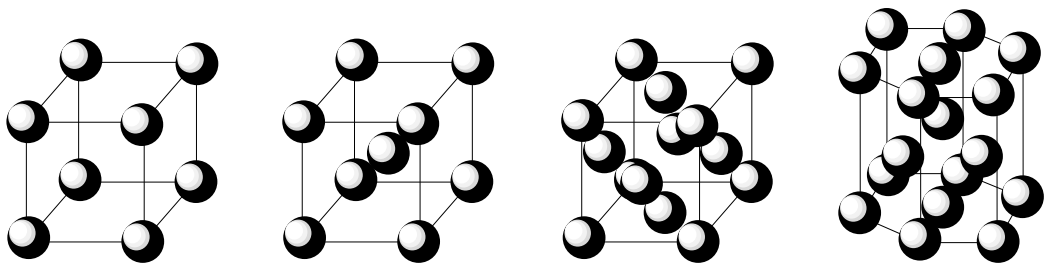

Figure 2.1: Commonly observed crystal unit cells of metallic materials. SC: simple cubic, BCC: body-centered cubic, FCC: face-centered cubic, HCP: hexagonal close-packed

2.1 Point defects

It has been observed that ordered crystalline materials, particularly metals, inherently possess imperfections, often referred to as crystalline defects. A

basic defect is an atomic vacancy wherein an atom is missing from one of the lattice sites. Vacancies occur naturally in all crystalline materials. At any given temperature up to the melting point, there is an equilibrium concentration of vacancy sites, see Siegel (1978); Ashby et al. (2009). Other types of point defect are known as interstitial atoms, substitutional atoms and Frenkel-pairs. The motion of a point defect is a diffusion process and depends on the temperature. Except at temperatures close to the melting point and very low strain rates, point defects merely contribute to large plastic deformations. However, a typical counterexample is creep at high temperature in which both conditions are likely drawn together.

2.2 Line defects: dislocations

The observation of formability of metallic materials, e.g. copper, at room temperature raises the fundamental question about the mechanisms of their irreversible deformations. Theoretical calculations for perfect crystals approximate the yield stress (σ_{yield}), i.e., the stress level at which non-reversible deformation starts, about one-sixth of the elastic shear modulus

$$\sigma_{\text{yield}} = \frac{\mu}{2\pi}, \tag{2.1}$$

where μ is the elastic shear modulus, see Dieter (1986); Perez (2004) and literature cited therein. However, experimental measurements show that the range of error obtained using Eq. (2.1) is from hundred to thousand percent, cf. Schmid (1924); Zupan & Hemker (2003); Yu & Spaepen (2004). This problem was open until the answer was given by a series of mathematical studies on bounded strains in isotropic continua which gives anticipation of topological defects at a larger scale than point defects, see Weingarten (1901); Timpe (1905); Volterra (1907); Ghosh (1926). The observation of traces of slip bands on the surface of deformed metals augments the idea of having planar distortions within the crystal lattice (dislocations). Fig. 2.2 (I) depicts the topology of an edge dislocation. Under the action of a shear stress the total energy of the lattice increases due to stretching. The dislocation moves in favor of the relaxation of the lattice energy, Fig. 2.2 (II). That means a series of jogging motions translates the extra plane to the right side of the crystal (Fig. 2.2 (III)). This leads to a step on the crystal's surface which is visible by high resolution atomic force microscopy (AFM). The length of the step is characterized by the so-called *Burgers vector* and depends on the lattice size parameters. After several planes reach the surface, they accumulate and form a bigger step (slip band) which is visible even by the naked eye.

Dislocations also appear in screw form. The atomistic configuration of the screw dislocation differs from an edge dislocation and it is even more complex

in the case of a mixed dislocation (dislocation loop). However, their definition can be unified at continuum-scale.

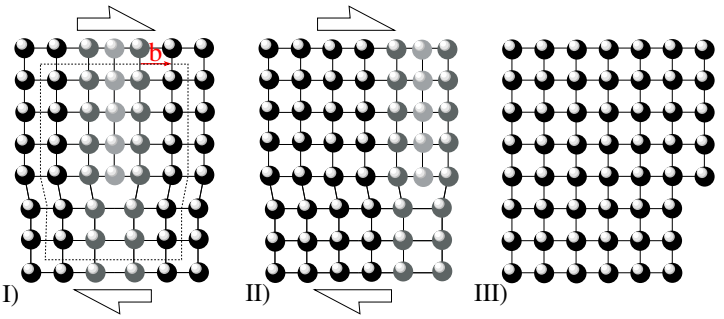

Figure 2.2: Schematic representation of an edge dislocation moving under the action of shear stress in SC

2.2.1 A continuum-scale approach to dislocation

The first continuum-scale approximation of the constitutive behavior of dislocations was developed by Schmid (1924); Taylor (1934); Orowan (1934); Polanyi (1934). In this approach, a dislocation is characterized by two orthogonal unit vectors, $\boldsymbol{s}$ and $\boldsymbol{m}$ (Fig. 2.3). Here, $\boldsymbol{s}$ denotes the Burgers vector and $\boldsymbol{m}$ is the normal vector of the glide plain. Based on the empirical Schmid's

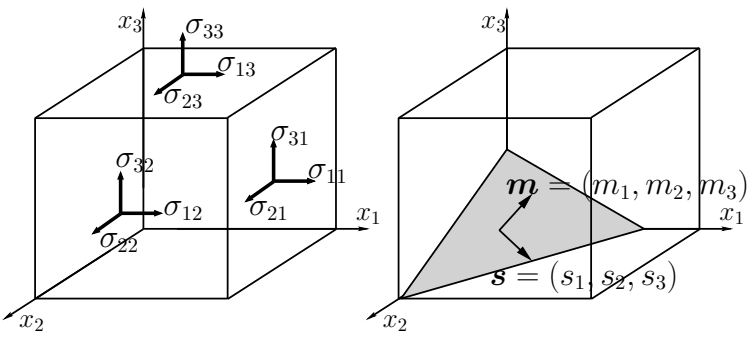

Figure 2.3: Geometrical relation between the characteristic dislocation vectors and the components of the Cauchy stress tensor in the deformed configuration

law, dislocation slip occurs if the resolved shear stress (σ_{RSS}) on a dislocation system reaches a critical value (σ_{CRSS}). According to Fig. 2.3, the general form of Schmid's law is written as

$$\sigma_{\mathrm{RSS}} = \boldsymbol{\sigma} : \boldsymbol{N} = \begin{pmatrix} \sigma_{11} & \sigma_{21} & \sigma_{31} \\ \sigma_{12} & \sigma_{22} & \sigma_{32} \\ \sigma_{13} & \sigma_{23} & \sigma_{33} \end{pmatrix} : \begin{pmatrix} s_1 m_1 & s_1 m_2 & s_1 m_3 \\ s_2 m_1 & s_2 m_2 & s_2 m_3 \\ s_3 m_1 & s_3 m_2 & s_3 m_3 \end{pmatrix}, \qquad (2.2)$$

where $\boldsymbol{\sigma}$ is the Cauchy stress tensor and (:) indicates the Frobenius inner product. $\boldsymbol{N} := (\boldsymbol{s} \otimes \boldsymbol{m})$ is also called *Schmid's tensor*.

Instead of dealing with an individual dislocation, it is assumed that a dislocation source continuously produces dislocations of the type $\{\boldsymbol{s}; \boldsymbol{m}\}$ with a constant rate of generation ($\dot{n}_{\mathrm{d}}$) at the continuum-scale. One such dislocation source is that proposed in Frank & Read (1950). It has been also observed that at room temperature, plastic shear is almost rate-independent, i.e.,

$$\frac{\mathrm{d}\dot{n}_{\mathrm{d}}}{\mathrm{d}\dot{\sigma}_{\mathrm{RSS}}} = 0. \tag{2.3}$$

More detailed information about the kinematics of dislocation slip will be given in Section 4.2.

2.2.2 Dislocation hardening

Though almost at any temperature a constant rate of dislocation generation has been observed, the critical resolved shear stress (σ_{CRSS}) depends on the number of dislocations or, more precisely, on the dislocation density. If dislocations are not inhibited, the rate of generation and motion remains constant (perfect plasticity). However, this is an ideal assumption and the material body is bounded in certain domains, e.g. grains enclosed by grain boundaries. Furthermore, this body comprises several types of dislocation barriers.

The presence of barriers such as dislocation locks, jogs, precipitated particles, twinning, grain boundaries etc., is one of the major sources for dislocation pile-ups. The direct consequence of dislocation pile-ups is a reduction of the generation rate ($\dot{n}_{\mathrm{d}}$) at the dislocation source. This occurs because the compression stress field of dislocation pile-ups reduces the effective applied force on the new-born dislocation at the source position. The result is an increase in slope of stress vs. strain digram in a strain-controlled experiment. This effect is traditionally referred to dislocation hardening. In fact the input energy is stored in the dislocation microstructure at the micro-scale.

In Sections 2.2.2.1 and 2.2.2.2 illustrative examples are given in order to highlight the concept of dislocation hardening and stored energy. Comprehensive studies including examples of precise analyses of the interaction among dislocation stress fields and barriers can be found in Peach & Köhler (1950); Hirth & Lothe (1982); Argon (2007).

2.2.2.1 1D illustrative example I: dislocation slip - ideal plasticity

Assume a strain-controlled shear test on a sample with unit volume including a Frank-Read source, Fig. 2.4 (A). The internal state of the sample can be

determined solely by the number of dislocations generated by Frank-Read source. In the elastic regime, Fig. 2.4 (A-B), the applied shear stress tends to bend the initial dislocation. Due to the dislocation's curvature, the response is naturally nonlinear. However, the stress-strain response is piece-wise linear. The applied stress raises until it reaches the critical threshold (σ_{CRSS}) at point (B) in Fig. 2.4. This threshold is considered to be the stress at which the source starts to generate dislocations continuously. It can be shown that the following relation holds:

$$\sigma_{CRSS} = \frac{2\mu b}{w}, \tag{2.4}$$

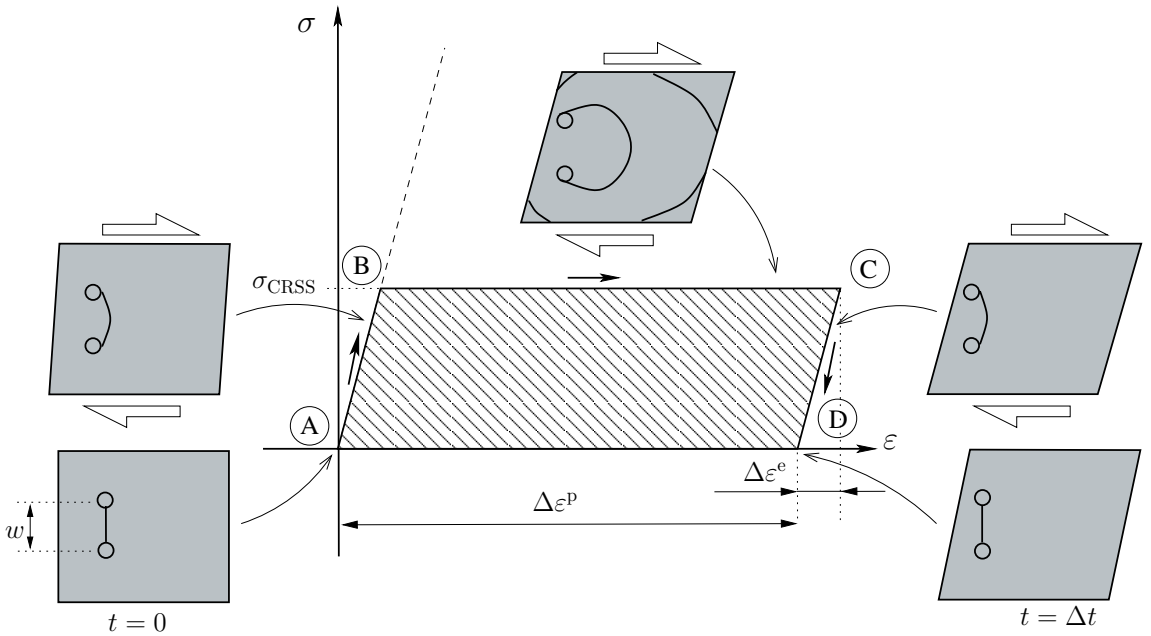

Figure 2.4: Schematic illustration of ideal plasticity resulting from a generation of dislocations by Frank-Read source and annihilation on the surface under the action of shear stress

where b and w are the norm of the Burgers vector and the width of Frank-Read source, respectively, see Peach & Köhler (1950); Hirth & Lothe (1982); Argon (2007). Dislocations pass throughout the sample and reach the surface. The free surface acts as a dislocation sink (annihilation processes), cf. Section 2.2. During the generation and annihilation of dislocations, the applied macro-scale shear stress does not increase beyond σ_{CRSS}. The reason is that the free surface annihilates mobile dislocations soon after their generation at the source position, Fig 2.4 (B-C). This results in the presence of dislocation steps on the surface and finally a macroscopic plastic shear. If the considered

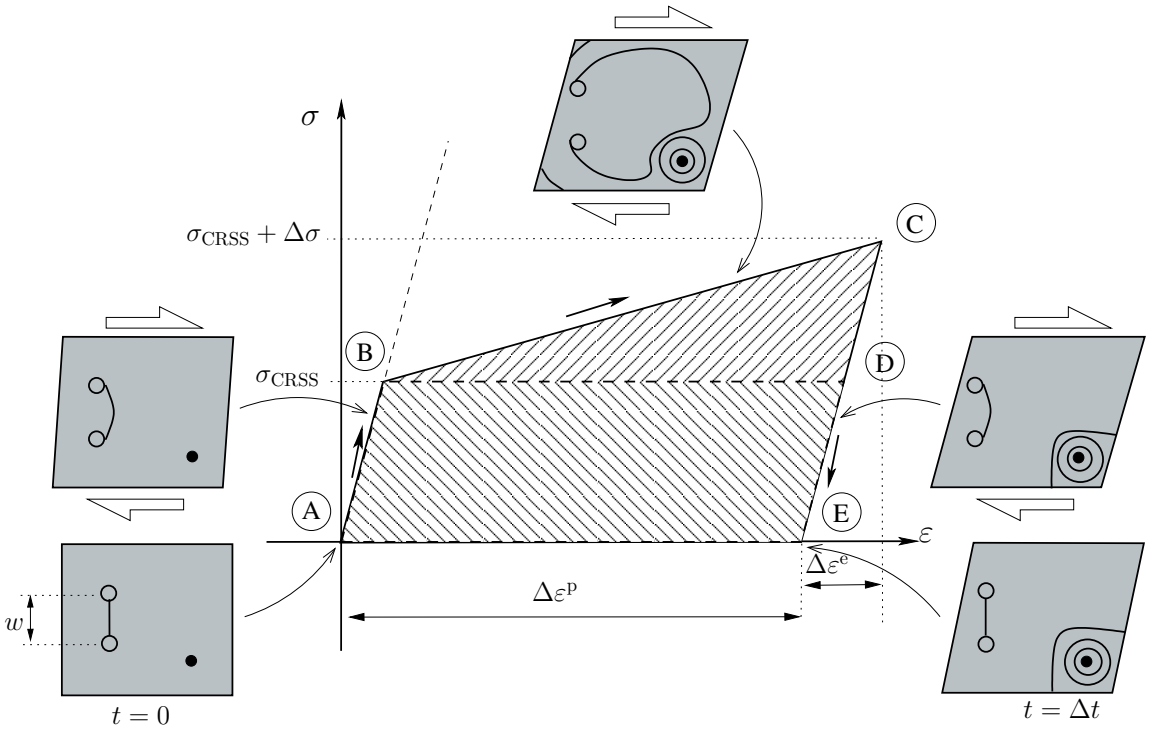

Figure 2.5: Schematic illustration of linear dislocation hardening and the stress resulting from a dislocation pile-up

sample is unloaded (Fig 2.4 (C-D)), the microstructure returns to its original configuration, Fig 2.4 (D).

The sole difference between the final configuration (Fig 2.4 (D)) and its initial counterpart at (Fig 2.4 (A)) is the external geometry. If this sample is reloaded at $t > \Delta t$, it follows the elastic path (Fig 2.4 (D-C)) until the stress reaches σ_{CRSS}. Thereafter, the generation and annihilation continue in the same way as before unloading, Fig 2.4 (B-C). Within the time interval $t = [0, \Delta t]$ the input energy is not fully stored in the sample but dissipated by exchange of the thermal energy on the material boundary (free surfaces).

2.2.2.2 1D illustrative example II: linear dislocation hardening

Consider a sample similar to the one explained in Section 2.2.2.1, but including a particle in a distance larger than w from the source. This particle acts as a dislocation barrier, see Fig. 2.5(A). It is assumed that the initial particle does not induce a long range stress field. Thus, the Frank-Read source becomes active, if the shear stress reaches σ_{CRSS}. It implies that the elastic deformation is similar to the previous example.

In contrast to the example given in Section 2.2.2.1, a portion of dislocation will be trapped around the barrier, see Peach & Köhler (1950); Hirth & Lothe (1982); Argon (2007). The trapped dislocations induce a repulsive interaction force on the dislocation at the source position and in opposite direction to the applied force. Consequently, to keep the Frank-Read source generating dislocations, the applied force (indirectly the resolved shear stress) increases, see Fig. 2.5(B-C). After unloading, the trapped dislocations are kept as a residual dislocation microstructure, (Fig. 2.5(D)). Upon reloading (Fig. 2.5(E-C)), the activation of the dislocation source requires a higher stress ($\sigma_{\mathrm{CRSS}} + \Delta\sigma$) at Fig. 2.5(C). Briefly, the history of deformation is kept in the form of trapped dislocations.

Remark 1 *The hardening mechanism explained in Section 2.2.2.2 is commonly referred to the self hardening mechanism. By way of contrast, dislocation slip on non-planar systems results in the so-called latent hardening.*

2.3 Twinning

If an adequate number of dislocations is not available in metallic materials with a low symmetric crystalline structure (BCC and HCP), mechanical twinning has been identified to be an important deformation mechanism, see Christian & Mahajan (1995) and literature cited therein. If the shear stress on a certain atomistic plane (the so called *twinning habit plane*) reaches a threshold, atoms at one side of the habit plane move to a new position. The motion is parallel to the habit plane and the displacement is proportional to the normal distance to the habit plane, Fig. 2.6. Since the atomistic displacement is nearly homo-

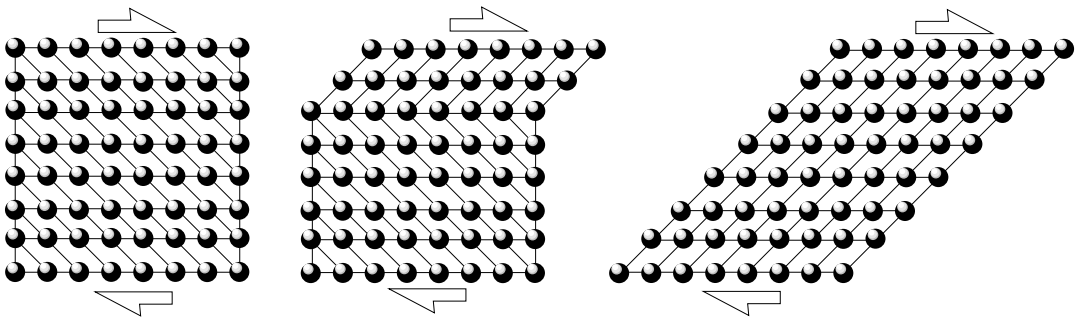

Figure 2.6: Classical illustration of the motion of a twinning interface under the action of shear stress

geneous, both sides of the twinning plane have the same crystal structure but bear different orientations.

2.3.1 Twinning invariants

Each twinning mode is identified by the invariant shear plane and shear direction. Consider the parallelepiped p_1 in Fig. 2.7, which is transformed by simple shear to p_2, see Fig. 2.6. Crystallographic elements of twinning are described as follows. In Fig. 2.7, κ_1 indicates the invariant plane of shear and the shear direction is represented by $\boldsymbol{\eta}_1$. During twinning, the atomistic plane κ_2 remains undistorted. The plane of shear (s) which contains the shear vector $\boldsymbol{\eta}_1$, is normal to both invariant and conjugate planes. The intersection between s and κ_2 identifies the conjugate shear direction, denoted as $\boldsymbol{\eta}_2$. Based on this notation, Tab. 2.1 summarizes the commonly observed twinning systems in HCP metals. Note that the Miller-Bravais indexing system is adopted. Moreover, Tab. 2.1 includes the amplitude of the twinning shear strain λ_{Twin}, which depends on the crystal axial ration $r = (c/a)$, see Christian & Mahajan (1995).

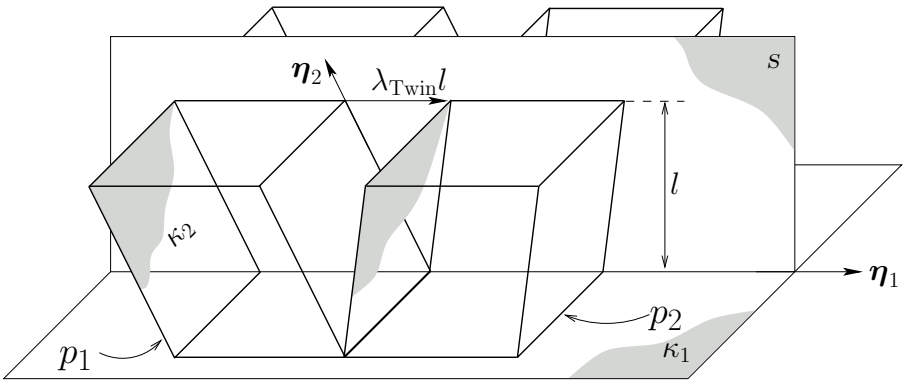

Figure 2.7: Crystallographic elements of twinning, cf. Christian & Mahajan (1995)

Table 2.1: Commonly observed twinning invariants in HCP metals, cf. Yoo (1981)

κ_1	κ_2	$\boldsymbol{\eta}_1$	$\boldsymbol{\eta}_2$	λ_{Twin}
$\{10\bar{1}2\}$	$\{10\bar{1}\bar{2}\}$	$\pm\langle 10\bar{1}\bar{1}\rangle$	$\pm\langle 10\bar{1}1\rangle$	$\frac{\lvert r^2-3\rvert}{r\sqrt{3}}$
$\{10\bar{1}1\}$	$\{10\bar{1}\bar{3}\}$	$\langle 10\bar{1}\bar{2}\rangle$	$\langle 30\bar{3}2\rangle$	$\frac{4r^2-9}{4r\sqrt{3}}$
$\{11\bar{2}2\}$	$\{11\bar{2}\bar{4}\}$	$\frac{1}{3}\langle 11\bar{2}\bar{3}\rangle$	$\frac{1}{3}\langle 22\bar{4}3\rangle$	$\frac{2(r^2-2)}{3r}$
$\{11\bar{2}1\}$	$\{0002\}$	$\frac{1}{3}\langle\bar{1}\bar{1}26\rangle$	$\frac{1}{3}\langle 112\rangle$	$\frac{1}{r}$

2.3.2 Mechanism of twinning

2.3.2.1 Initiation

There is controversial debate about the nucleation of twinning lamellas under the action of the applied stress in magnesium. Generally, two main types of nucleation mechanisms for HCP metals have been proposed in the literature, see Orowan (1954); Bell & Cahn (1957); Price (1960); Mendelson (1970); Hirth & Lothe (1982); Yoo et al. (2002). The first one is based on experimental measurements using dislocation-free Zn whiskers, which suggests a homogeneous twinning nucleation, see Orowan (1954); Price (1960). However, it has been also observed that in larger Zn specimens, the nucleation of twinning occurs after the formation of dislocation pile-ups. In these samples, the second mechanism (heterogeneous nucleation) has been observed at locations of stress concentration zones and stacking faults, see Bell & Cahn (1957); Mendelson (1970); Yoo (1981); Hirth & Lothe (1982).

In spite of the conflict about the aforementioned different mechanisms of twinning nucleation, the respective theories agree that the activation of a particular twinning system follows the critical resolved shear stress law (Schmid's law). By virtue of Eq. (2.2) and using the characteristic vectors of twinning invariants (the normal to (κ) and ($\boldsymbol{\eta}$)), the resolved shear stress can be calculated in the same fashion as for a dislocation system. However, the size and the preparation method as well as the deformation history of the respective sample affect the critical value significantly, see Yoo (1981); Hirth & Lothe (1982); Szczerba et al. (2004); Yu et al. (2009).

2.3.2.2 Propagation

At the atomistic-scale, there are two possible mechanisms by which a particular material volume element can be transformed from the initial configuration into the twinning configuration:

1. Translating all atoms of a complete layer from the initial phase to the

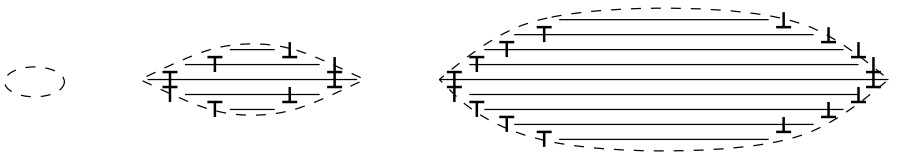

Figure 2.8: A model for the growth of a twinning lenticular, cf. Christian & Mahajan (1995)

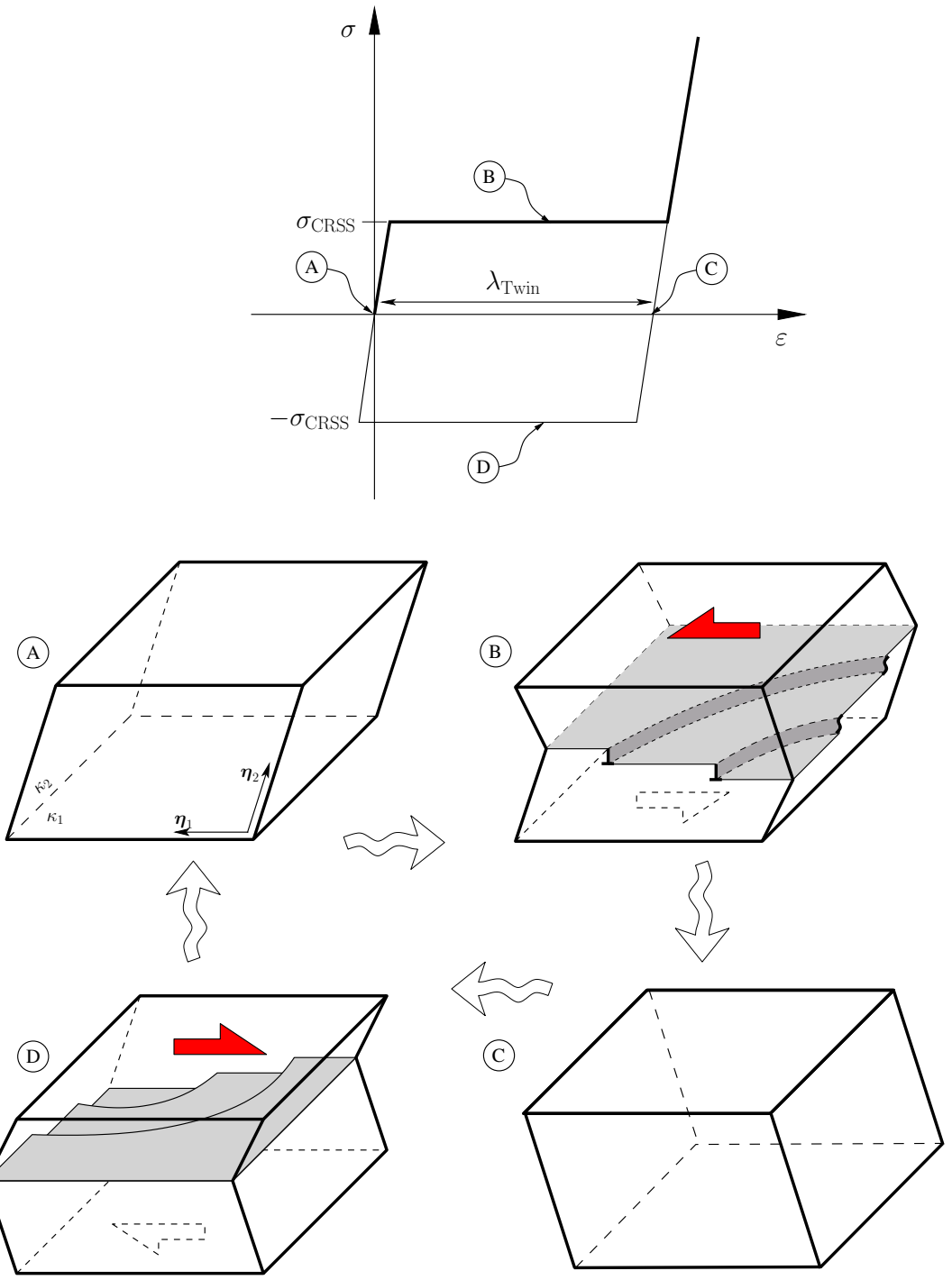

Figure 2.9: Schematic diagram representing the correlation between the stress vs. strain diagram and a twinning transformation, A) The parallelepiped represents the initial variant, B) moving zonal dislocations under the action of applied stresses, C) second unstressed crystal variant, D) moving zonal dislocations under reverse loading

twinning phase (Fig. 2.6),

2. Dislocation loops on the twinning boundary (the so-called *zonal dislocations*) transform the initial configuration into the twinning phase, see Hirth & Lothe (1982); Chen & Howitt (1998); Li & Ma (2009).

The magnitude of the shear stress required for the first type of transformation is of the order of the shear modulus (Eq. (2.4)). This is in contrast to experimental results indicating much smaller resolved shear stresses. However, the dislocation based mechanism explains the commonly observed lenticular shape of twinning lamellas (see Fig. 2.8) as well as the low activation stress of twinning, see Barrett (1949); Frank (1951); Thompson & Millard (1952); Yoo et al. (2002); Li & Ma (2009); Wang et al. (2009).

Fig. 2.9 illustrates schematically the transformation of a particular twinning invariant to its conjugate by the motion of zonal dislocations in the direction of applied shear stresses. Furthermore, a hysteresis loop appears in the related stress vs. strain diagram through a cyclic deformation. Starting from the original material element (Fig. 2.9(A)), the parallelepiped sample represents the material with the initial crystallographic orientation. At the outset of loading, the sample gives an elastic response before the applied stress reaches the critical value (σ_{CRSS}). Then, zonal dislocations are initiated at the right-hand side of the sample moving toward the direction of the applied shear stress, (Fig. 2.9(B)). The downward motion of the interface between two invariants is mediated by waves of zonal dislocations. During the motion of the interface, a stress plateau appears in the stress vs. strain diagram. Once the sample is completely transformed into the second crystallographic invariant, further strain is accommodated by elastic deformation. Releasing the load gives rise to the second stress free invariant, (Fig. 2.9(C)). Reverse loading stimulates the

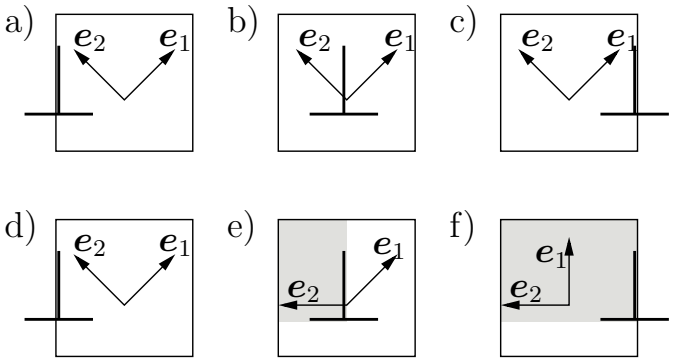

Figure 2.10: Schematic representation of the effect of a normal dislocation (a-c) and a zonal dislocation (d-f) on the crystallographic orientation of the parent crystal lattice

zonal dislocation to move in the opposite direction and results in the second stress plateau, (Fig. 2.9(D)). Finally, the material structure is transformed into the initial invariant after unloading, (Fig. 2.9(A)).

Remark 2 *At first glance, the kinematics of the zonal dislocation resembles the one presented in ideal dislocation plasticity (Section 2.2.2.1). However, the key difference is that once a zonal dislocation passes over a material element, it reorients the lattice base vectors.*

Remark 3 *If only one twinning variant is active, self and latent hardening do not occur since the Burgers vectors of zonal dislocations are parallel to each other (see Fig. 2.8 and Fig. 2.9b). For a comparison with ideal dislocation plasticity, refer to Section 2.2.2.1. However and in contrast to dislocation slip, the material element does not only experience plastic slip, but also a reorientation of the lattice. Consequently, the stress power is partly dissipated through dislocation slip and partly stored as crystal reorientation.*

2.4 Micro-mechanical deformation systems of magnesium

Since the objective of the current thesis is the modeling of plastic deformation of magnesium, a short review of its micro-mechanical deformation systems is given in this section. Attractive features of magnesium and its alloys, which were discussed in Chapter 1, make them the topic of a significant number of research studies. Accordingly, one can find a large number of comprehensive experimental and analytical studies regarding slip and twinning in magnesium (Schmid, 1924; Siebel, 1939; Hauser et al., 1955; Reed-Hill & Robertson, 1957a; Yoshinaga & Horiuchi, 1963; Tegart, 1964; Roberts & Partridge, 1966; Wonsiewicz & Backofen, 1967; Kelley & Hosford, 1968; Obara et al., 1973; Yoo, 1981; Ando & Tonda, 2000; Agnew et al., 2001, 2005; Beausir et al., 2008; Li & Ma, 2009; Byer et al., 2010; Lilleodden, 2010). According to these publications and works cites therein, the number of possible deformation systems in magnesium is relatively large. However, in this section, special focus is on the energetically most favorable deformation systems which contribute to plastic deformation in conventional forming processes.

The energetically most favorable slip systems in HCP metals are prismatic and basal moving on $\langle a \rangle$. They provide four independent deformation systems. However, the resultant shear strain component of pyramidal slip on $\langle a \rangle$ is equivalent to slip on basal and prismatic planes. Once a slip system becomes active with the Burgers vector of the type $\langle a \rangle + \langle c \rangle$, it satisfies the Taylor criterion for homogeneous plastic deformation, see Taylor (1938); Kratochvil & Sedlacek (2004). In general, the relative activity of dislocations with the

Burgers vector in basal plane $\langle a \rangle$ compared to those with a Burgers vector of the type $\langle a \rangle + \langle c \rangle$ is dictated by the crystal axial ratio c/a. Higher magnitudes of c/a result in a lower activity of $\langle a \rangle + \langle c \rangle$ systems. The possible slip modes (slip direction + glide plane) in HCP metals are listed in Tab. (2.2).

2.4.1 Dislocation systems

Fig. 2.11 illustrates the frequently reported crystallographic slip planes and directions in magnesium single crystal. Through experimental analyses it has been revealed that basal slip is the most dominant deformation mode in magnesium alloys in a wide range of testing temperatures, see Burke (1952); Hauser et al. (1955). In these studies, it is also revealed that the prismatic system is active, but only in regions with higher stress intensities. If the basal system is suppressed by geometrical constraints, e.g. a tensile test perpendicular to the basal plane, the prismatic system $\langle a \rangle$ and the pyramidal system $\langle a \rangle + \langle c \rangle$ govern plastic deformation, see Reed-Hill & Robertson (1957a); Yoshinaga & Horiuchi (1963).

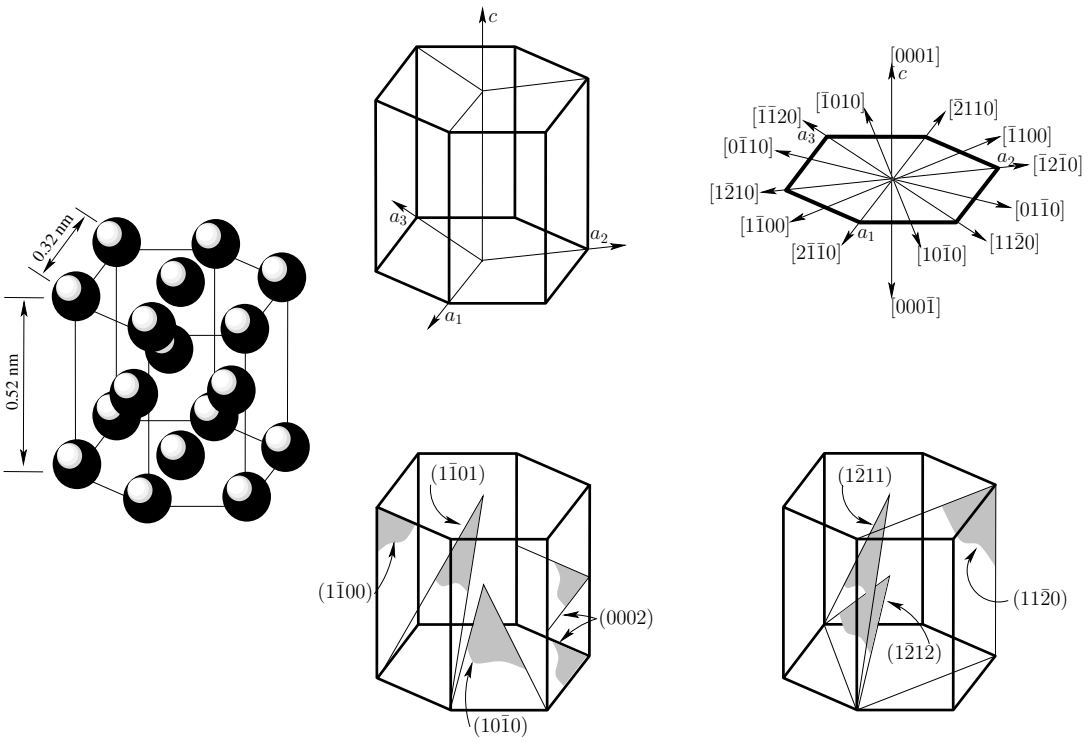

Figure 2.11: Geometrical illustration of frequently reported crystallographic slip planes and directions in a single crystal magnesium

Table 2.2: Independent dislocation systems in HCP metals, cf. Yoo (1981)

Direction	Plane	Notation	Number of independent modes
$\langle a \rangle$	Basal	$\{0002\}\langle 11\bar{2}0\rangle$	2
$\langle a \rangle$	Prismatic	$\{1\bar{1}00\}\langle 11\bar{2}0\rangle$	2
$\langle a \rangle$	Pyramidal	$\{1\bar{1}01\}\langle 1120\rangle$	4
$\langle a \rangle + \langle c \rangle$	Pyramidal	$\{10\bar{1}1\}\langle 11\bar{2}\bar{3}\rangle$	4
$\langle a \rangle + \langle c \rangle$	Pyramidal	$\{2\bar{1}\bar{1}1\}\langle 11\bar{2}\bar{3}\rangle$	4
$\langle a \rangle + \langle c \rangle$	Pyramidal	$\{11\bar{2}2\}\langle 11\bar{2}\bar{3}\rangle$	4

2.4.2 Twinning systems

2.4.2.1 Tensile twinning

It has been identified that elongating a single crystal magnesium toward the c-axis activates twinning at the plane $\kappa := \{10\bar{1}2\}$. Twinning occurs because it requires less activation energy than pyramidal slip $\langle a \rangle + \langle c \rangle$. The crystal structure of the twinning phase is the mirrored counterpart of the initial crystal with respect to $\kappa := \{10\bar{1}2\}$. This leads to 86.3 degrees rotations of the basal planes, see Wonsiewicz & Backofen (1967). Fig. 2.12(b) shows the relative configuration of the crystal orientation of the initial and twinning phase. A rotation of the crystal lattice changes the Schmid factor of the current active or non-active slip systems by the transformation of their characteristic vectors. Since the rotation angle is nearly 90 degrees, a new set of deformation systems may result in a totally different deformation response than the one of the initial crystal.

2.4.2.2 Contraction twinning

Pioneering works on single crystal magnesium at room temperature reveal the traces of contraction twinning at the plane $\kappa := \{10\bar{1}1\}$ (Wonsiewicz & Backofen, 1967; Reed-Hill & Robertson, 1957a; Reed-Hill, 1960; Couling et al., 1959). Fig. 2.12(c) shows the mechanism of contraction twinning proposed by Wonsiewicz & Backofen (1967). Under compression loading, twinning lenticulars are observed at the plane $\kappa := \{10\bar{1}1\}$. The close packed layers of twinning lenticulars have a 56 degrees angular difference with the basal planes of the initial crystal. The resolved shear stress on the tensile twinning system within the lenticular increases upon first contraction twinning. Thus, tensile twinning occurs immediately inside the initial twin resulting in a 37 degrees rotation angle with respect to basal planes in the initial crystal (Fig. 2.12(d)). This mechanism is called double twinning.

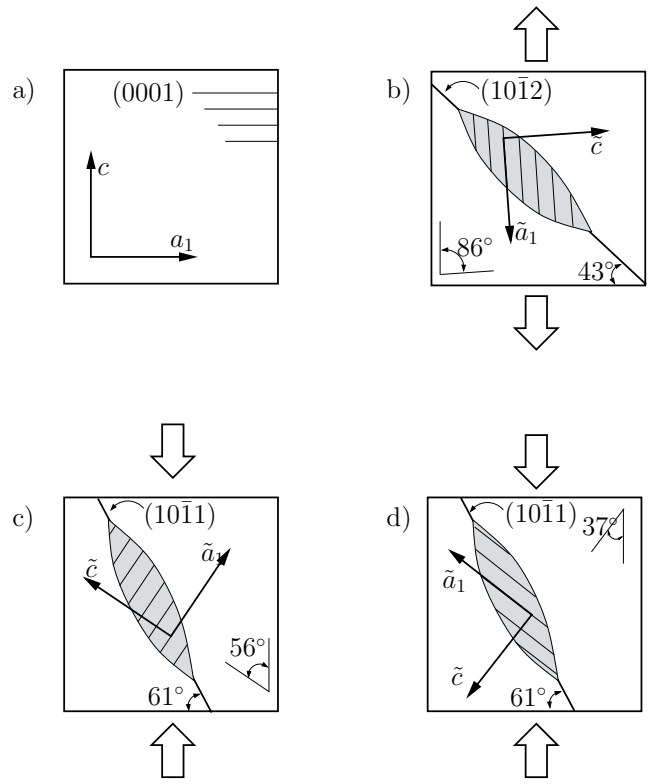

Figure 2.12: Rotation of basal planes due to twinning, a) the initial material element representing the initial crystallographic directions c and a_1, b) lenticular represents the tensile twinning, c) contraction twinning, d) double twinning

Remark 4 *While there is an agreement about tensile twinning, the existence of contraction twinning is still under debate. Although most of the pioneering works indicate that contraction twinning is the dominant deformation system, recent analyses using precisely prepared micro-samples, indicate that the pyramidal system governs the contraction deformation, see Byer et al. (2010); Lilleodden (2010). In the current thesis, the pyramidal deformation system is thus considered.*

2.4.3 Channel die test

Plastic deformations of single crystal magnesium have been investigated by Wonsiewicz & Backofen (1967) and Kelley & Hosford (1968) in the late sixties. The present author realized that their experimental results still provide the most comprehensive information about magnesium micro-mechanical deformation systems. The primary data published by Kelley & Hosford (1968) is used in the following chapters as reference characterizing the hardening be-

Table 2.3: Crystallographic orientations used in the channel die tests on magnesium single crystals by Kelley & Hosford (1968)

Test label	Loading direction	Constrained direction
A	[0001]	$[10\bar{1}0]$
C	$[10\bar{1}0]$	[0001]
E	$[10\bar{1}0]$	$[1\bar{2}10]$
G	[0001]at 45°	$[10\bar{1}0]$

havior of magnesium.

Kelley and Hosford (Kelley & Hosford (1968)) prepared seven hexahedron single crystal samples. The samples were cut out of a single crystal bar with a predetermined crystal orientation. The crystal orientation varied among the samples while having the same cuboid exterior geometry. The crystal orientation of each sample was chosen such that a specific slip system became active. The crystallographic orientations of four samples used by Kelley & Hosford (1968) are given in Tab. 2.3. The remaining three samples are omitted here because of their similar deformation behavior. Further detailed information regarding the sample preparation and compression procedure are omitted here. The results of the channel die tests in terms of true stress vs. true strain in the punching direction (z-axis) are shown in Fig. 2.13 where the directional dependency of the deformation of single crystal magnesium is clearly demonstrated. Comparisons of this data with numerically obtained results will be given in Chapter 7.

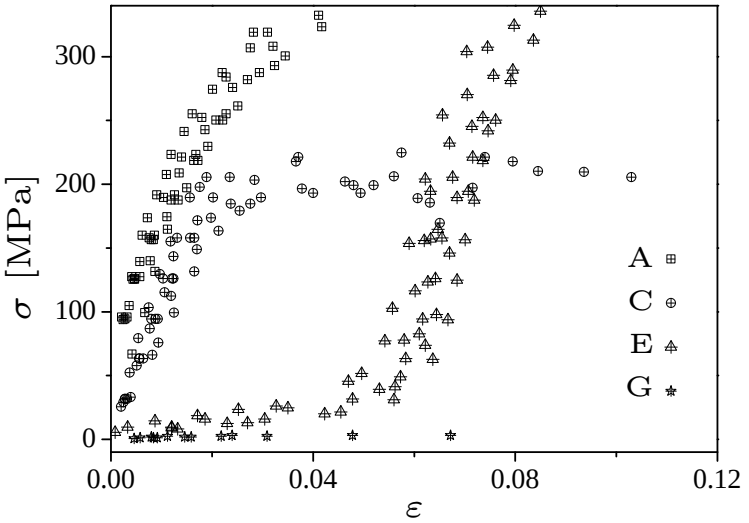

Figure 2.13: Experimental data of the channel die tests on magnesium single crystals in terms of true stress vs. true strain conducted by Kelley and Hosford (Kelley & Hosford (1968))

3 Fundamentals of continuum mechanics

In the previous chapter, micromechanical deformation systems have been introduced at the atomistic-scale. Instead of considering the material as a large collection of discrete atoms, a continuum mechanical standpoint is adopted here. Consequently, the description of the mechanical behavior of the bulk material is simplified by using an averaging method such that the material body is considered as a continuous medium. This chapter is devoted to present a short review of the kinematics as well as the governing laws describing the response of continuous media (continuum mechanics). Though, nowadays, these funduments are well established in literature, they are required for the models proposed in this work. For further details, the reader is referred to the works Truesdell & Noll (1965a); Holzapfel (2000); Haupt (2000); Mosler (2007). Special attention is given to the behavior of metallic materials.

3.1 Kinematics

In a three dimensional Euclidean space ($\mathbb{R}^3$) any material point P of a body $\mathcal{B}$ within the domain $\Omega_0 \subset \mathbb{R}^3$ is addressed by a position vector (see Fig. 3.1)

$$\boldsymbol{X}(P) = X_i \boldsymbol{e}_i, \tag{3.1}$$

where $\boldsymbol{e}_i$ are the base vectors of the Cartesian reference coordination system. Note that in Eq. (3.1) the Einstein summation convention is applied. The body deforms under the action of applied body forces, surface tractions and prescribed displacements. The resulting deformation is described by the mapping $\boldsymbol{\varphi} : \Omega_0 \rightarrow \mathbb{R}^3$ which is sufficiently smooth and injective. It maps the position $\boldsymbol{X} \in \Omega_0$ of material particles in the reference configuration (initial configuration) to their positions $\boldsymbol{x} \in \boldsymbol{\varphi}(\Omega_t)$ in the deformed configuration (cf. Ciarlet (1988)). The local deformation at a material point, with the position vector $\boldsymbol{X}$, is defined by the transformation of a line element

$$\mathrm{d}\boldsymbol{x} = \boldsymbol{F} \cdot \mathrm{d}\boldsymbol{X}, \tag{3.2}$$

and

$$\boldsymbol{F} = \mathrm{GRAD}\boldsymbol{\varphi} \quad \text{with} \quad \mathrm{GRAD} := \frac{(\bullet)}{\partial \boldsymbol{X}} \quad \text{and} \quad \mathrm{grad} := \frac{(\bullet)}{\partial \boldsymbol{x}}, \tag{3.3}$$

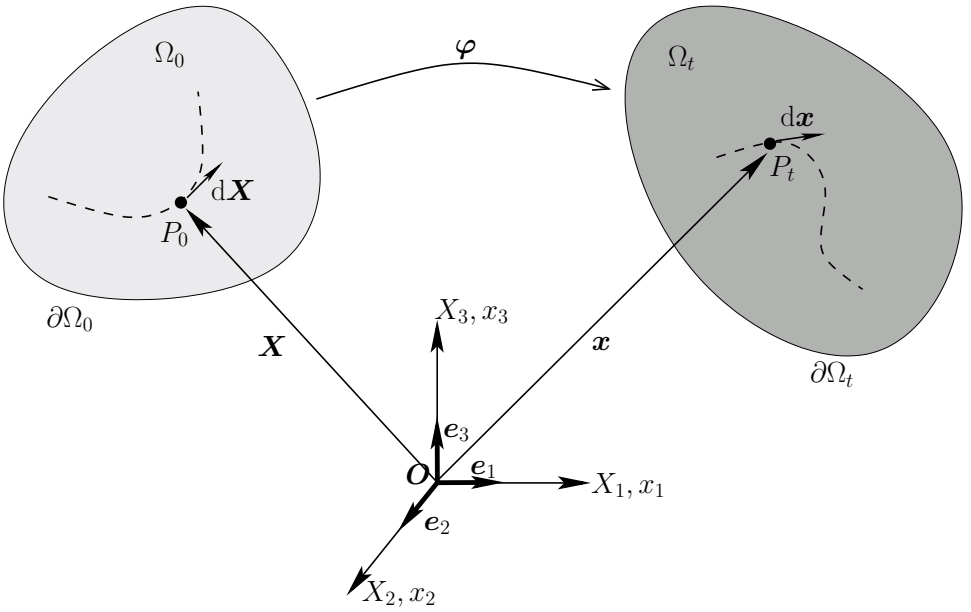

Figure 3.1: Reference and current configuration of a material body in the Cartesian reference coordinate system

where $\boldsymbol{F}$ is a second-order two-point tensor representing the material deformation gradient. Being continuously differentiable with respect to $\boldsymbol{X}$ and time t (smooth function), the deformation map ($\boldsymbol{\varphi}$) preserves continuity of the material. Since $\boldsymbol{\varphi}|_\Omega$ is injective, $\boldsymbol{\varphi}^{(-1)}|_\Omega$ exists and by the implicit function theorem $\det\boldsymbol{F} \neq 0 \; \forall \boldsymbol{X} \in \Omega$. Moreover, the local invertibility condition follows

$$\det\boldsymbol{F} > 0 \qquad \forall \boldsymbol{X} \in \Omega, \tag{3.4}$$

see Truesdell & Noll (1965a); Mosler (2007). Accordingly, $\boldsymbol{F} \in GL_+(3)$ with $GL_+(n)$ denoting the general linear group of dimension n showing a positive determinant. With this property, the following polar decompositions exist:

$$\begin{aligned} \forall \boldsymbol{F} \quad &\in \quad GL_+(3) \qquad \exists \boldsymbol{R}, \boldsymbol{U} \in GL_+(3) \quad : \quad \boldsymbol{F} = \boldsymbol{R} \cdot \boldsymbol{U} \\ \forall \boldsymbol{F} \quad &\in \quad GL_+(3) \qquad \exists \boldsymbol{R}, \boldsymbol{V} \in GL_+(3) \quad : \quad \boldsymbol{F} = \boldsymbol{V} \cdot \boldsymbol{R}. \end{aligned}$$

where $(\cdot)$ defines the simple tensor contraction, $\boldsymbol{R}$ is a proper orthogonal tensor $\boldsymbol{R} \in SO(3)$ ($\boldsymbol{R}^{-1} = \boldsymbol{R}^{\mathrm{T}}$, $\det\boldsymbol{R} = +1$) and $\boldsymbol{V}$ and $\boldsymbol{U}$ are symmetric and positive definite stretch tensors. Accordingly,

$$\boldsymbol{U} = \boldsymbol{R}^{-1} \cdot \boldsymbol{V} \cdot \boldsymbol{R} = \boldsymbol{R}^{\mathrm{T}} \cdot \boldsymbol{V} \cdot \boldsymbol{R}. \tag{3.5}$$

Eq. (3.5) implies that $\boldsymbol{U}$ and $\boldsymbol{V}$ have the same eigenvalues ($\lambda_i > 0$) however, they differ in their eigenvectors ($\boldsymbol{N}_i$ and $\boldsymbol{n}_i$). These principle directions are related by the rotation transformation

$$\boldsymbol{N}_i = \boldsymbol{R}^{\mathrm{T}} \cdot \boldsymbol{n}_i. \tag{3.6}$$

Consequently, the spectral decomposition theorem can be applied to $\boldsymbol{U}$ and $\boldsymbol{V}$ leading to

$$\boldsymbol{U} = \sum_{i=1}^{3} \lambda_i \boldsymbol{N}_i \otimes \boldsymbol{N}_i \quad \text{with} \quad \boldsymbol{N}_i \cdot \boldsymbol{N}_j = \delta_{ij} \tag{3.7}$$

$$\boldsymbol{V} = \sum_{i=1}^{3} \lambda_i \boldsymbol{n}_i \otimes \boldsymbol{n}_i \quad \text{with} \quad \boldsymbol{n}_i \cdot \boldsymbol{n}_j = \delta_{ij} \tag{3.8}$$

where δ_{ij} is the Kronecker delta. Based on the spectral decomposition, a family of strain measures can be introduced. According to Hill (1968, 1978); Mosler (2007), classical Hill strains are defined as

$$\boldsymbol{A}(\boldsymbol{U}) = \sum_{i=1}^{3} f(\lambda_i) \boldsymbol{N}_i \otimes \boldsymbol{N}_i \tag{3.9}$$

$$\boldsymbol{a}(\boldsymbol{V}) = \sum_{i=1}^{3} f(\lambda_i) \boldsymbol{n}_i \otimes \boldsymbol{n}_i \tag{3.10}$$

with f representing a scaling function which is monotonously increasing and smooth. It is also required to meet the normalizing conditions, i.e., $f(1) = \acute{f}(1) - 1 = 0$. Following the general formula for Lagrangian strain tensors

$$\boldsymbol{E}_{(m)} = \frac{1}{2m}(\boldsymbol{U}^{(2m)} - \boldsymbol{I}), \tag{3.11}$$

(see Hill (1968)), the frequently used strain tensors are defined as

- The Green-Lagrangian strain tensor

$$\boldsymbol{E}_{(1)} = \frac{1}{2}(\boldsymbol{U}^2 - \boldsymbol{I}) = \sum_{i=1}^{3} \frac{1}{2}(\lambda_i^2 - 1) \boldsymbol{N}_i \otimes \boldsymbol{N}_i \tag{3.12}$$

- The Biot strain tensor

$$\boldsymbol{E}_{(\frac{1}{2})} = (\boldsymbol{U} - \boldsymbol{I}) = \sum_{i=1}^{3} (\lambda_i - 1) \boldsymbol{N}_i \otimes \boldsymbol{N}_i \tag{3.13}$$

- The logarithmic or true strain tensor

$$\boldsymbol{E}_{(0)} = \ln(\boldsymbol{U}) = \sum_{i=1}^{3} \ln(\lambda_i) \boldsymbol{N}_i \otimes \boldsymbol{N}_i. \tag{3.14}$$

Remark 5 *Instead of using the aforementioned strain measures, the right Cauchy-Green deformation tensor defined as*

$$\begin{aligned} \boldsymbol{C} &= \boldsymbol{F}^{\mathrm{T}} \cdot \boldsymbol{F} = \boldsymbol{U}^{\mathrm{T}} \cdot \boldsymbol{R}^{\mathrm{T}} \cdot \boldsymbol{R} \cdot \boldsymbol{U} \\ &= \boldsymbol{U}^2 = \sum_{i=1}^{3} \lambda_i^2 \boldsymbol{N}_i \otimes \boldsymbol{N}_i \end{aligned} \tag{3.15}$$

is also frequently applied in constitutive material modeling. According to Eq. 3.12, $\boldsymbol{C}$ *and the strain tensor* $\boldsymbol{E}_{(1)}$ *are linearly related.*

3.2 Balance laws

3.2.1 Conservation of mass

The mass of a closed domain Ω_0 is an inherent property being the measure of its constitutional matter. Thus, the total mass of the body $\mathcal{B}_0$ in a closed domain Ω_0 is given by

$$m = \int_{\Omega_0} \rho_0 \, \mathrm{d}V = \int_{\boldsymbol{\varphi}(\Omega_0)} \rho \, \mathrm{d}v, \tag{3.16}$$

where ρ_0 and ρ are the volume densities with respect to the initial Ω_0 and deformed body $\boldsymbol{\varphi}(\Omega_0)$. The deformation $\boldsymbol{\varphi}$ maps the volume element $\mathrm{d}V$ to $\mathrm{d}v$ by the relation

$$\mathrm{d}v = J \mathrm{d}V \quad \text{with} \quad J = \mathrm{detGRAD}\boldsymbol{\varphi}. \tag{3.17}$$

After inserting Eq. (3.16) into Eq. (3.17), the local form of the principle of conservation of mass is obtained as

$$\rho_0 = J\rho. \tag{3.18}$$

Moreover, the mass of a closed system during a dynamic process is conserved. Accordingly, the rate form of Eq. (3.16) can be written as

$$\int_{\boldsymbol{\varphi}(\Omega_0)} (\dot{J}\rho + J\dot{\rho}) \, \mathrm{d}v = 0. \tag{3.19}$$

3.2.2 Conservation of momentum

The inertia residing in a moving body is called momentum. The amount of momentum depends directly on the mass and the velocity of the respective object. The velocity itself depends on the spatial positions of the moving object. It comprises a translational and a rotational part resulting in two forms of momentum.

3.2.2.1 Conservation of linear momentum

The Eulerian description of the linear momentum is given by

$$\mathcal{I} = \int\limits_{\boldsymbol{\varphi}(\Omega_0)} \rho \dot{\boldsymbol{\varphi}} \, \mathrm{d}v. \tag{3.20}$$

Based on the principle of conservation of linear momentum (Newton's second law), the rate of change in momentum is equivalent to the applied force on the respective body, i.e.,

$$\dot{\mathcal{I}} = \frac{\mathrm{d}}{\mathrm{d}t} \int\limits_{\boldsymbol{\varphi}(\Omega_0)} \rho \dot{\boldsymbol{\varphi}} \, \mathrm{d}v = \int\limits_{\boldsymbol{\varphi}(\Omega_0)} \rho \boldsymbol{b} \, \mathrm{d}v + \int\limits_{\boldsymbol{\varphi}(\partial\Omega_0)} \boldsymbol{t}^* \, \mathrm{d}a, \tag{3.21}$$

where the first term on the right-hand side is the body force acting on $\boldsymbol{\varphi}(\Omega_0)$ and $\boldsymbol{b}$ corresponds to the body force per unit mass. The traction vector $\boldsymbol{t}^*$ is defined as the force per unit surface of the boundary of the domain (Fig. 3.2). Eq. (3.21) gives the balance of linear momentum in a weak form. Following Cauchy's stress theorem, a second-order tensor $\boldsymbol{\sigma}$ can be postulated such that the traction vector $\boldsymbol{t}^*$ can be expressed as a linear function of $\boldsymbol{n}$ which is the normal vector of the unit element $\mathrm{d}a$, i.e.,

$$\boldsymbol{t}^* = \boldsymbol{\sigma} \cdot \boldsymbol{n}. \tag{3.22}$$

Applying the Gauss' theorem

$$\int\limits_{\boldsymbol{\varphi}(\partial\Omega_0)} \boldsymbol{\sigma} \cdot \boldsymbol{n} \, \mathrm{d}a = \int\limits_{\boldsymbol{\varphi}(\Omega_0)} \mathrm{div}\boldsymbol{\sigma} \, \mathrm{d}v \tag{3.23}$$

the local form of conversation of linear momentum for a system with a conserved mass is given by

$$\mathrm{div}\boldsymbol{\sigma} = \rho(\ddot{\boldsymbol{\varphi}} - \boldsymbol{b}). \tag{3.24}$$

3.2.2.2 Conservation of angular momentum

The angular momentum with respect to the origin of the coordinate system is defined by

$$\int\limits_{\boldsymbol{\varphi}(\Omega_0)} \rho(\boldsymbol{\varphi} \times \dot{\boldsymbol{\varphi}}) \, \mathrm{d}v, \tag{3.25}$$

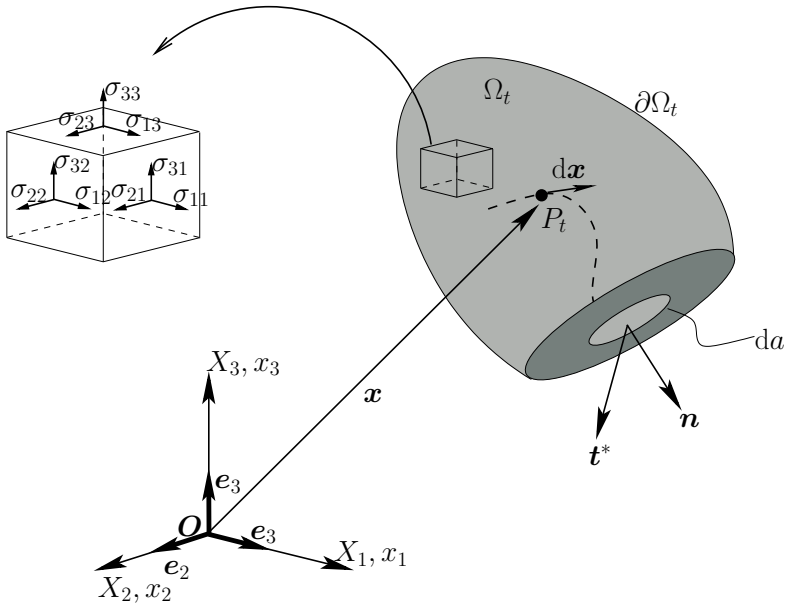

Figure 3.2: Cauchy stress tensor and traction vector in the deformed configuration

where $\times$ denotes the cross product. The body force and the surface traction apply a torque on a material point addressed by $\boldsymbol{\varphi}(\boldsymbol{X})$. Obviously, the applied torque and Eq. (3.25) are strictly dependent on the choice of the reference point (origin). Euler's law of motion states that the rate of change of the angular momentum is equivalent to the applied torque, i.e.,

$$\frac{\mathrm{d}}{\mathrm{d}t}\int\limits_{\boldsymbol{\varphi}(\Omega_0)} \rho(\boldsymbol{\varphi}\times\dot{\boldsymbol{\varphi}})\,\mathrm{d}v = \int\limits_{\boldsymbol{\varphi}(\Omega_0)} \rho(\boldsymbol{\varphi}\times\boldsymbol{b})\,\mathrm{d}v + \int\limits_{\boldsymbol{\varphi}(\partial\Omega_0)} \rho(\boldsymbol{\varphi}\times\boldsymbol{t}^*)\,\mathrm{d}a. \tag{3.26}$$

Expanding the left-hand side of Eq. (3.26) results in

$$\begin{aligned}\int\limits_{\Omega_0} (\dot{\overline{\rho J}})(\boldsymbol{\varphi}\times\dot{\boldsymbol{\varphi}})\,\mathrm{d}V + \int\limits_{\Omega_0} \rho(\dot{\boldsymbol{\varphi}}\times\dot{\boldsymbol{\varphi}})\,J\mathrm{d}V + \int\limits_{\boldsymbol{\varphi}(\Omega_0)} \rho(\boldsymbol{\varphi}\times\ddot{\boldsymbol{\varphi}})\,\mathrm{d}v \\ = \int\limits_{\boldsymbol{\varphi}(\Omega_0)} \rho(\boldsymbol{\varphi}\times\boldsymbol{b})\,\mathrm{d}v + \int\limits_{\boldsymbol{\varphi}(\partial\Omega_0)} \rho(\boldsymbol{\varphi}\times(\boldsymbol{\sigma}\cdot\boldsymbol{n}))\,\mathrm{d}a.\end{aligned} \tag{3.27}$$

By virtue of Eq. (3.19) and ($\dot{\boldsymbol{\varphi}}\times\dot{\boldsymbol{\varphi}} = \boldsymbol{0}$), the application of the divergence theorem to the right-hand side of Eq. (3.27) gives

$$\int\limits_{\boldsymbol{\varphi}(\Omega_0)} \boldsymbol{\varphi}\times(\mathrm{div}\boldsymbol{\sigma} + \rho\boldsymbol{b} - \rho\ddot{\boldsymbol{\varphi}})\mathrm{d}v + \int\limits_{\boldsymbol{\varphi}(\Omega_0)} \mathrm{grad}\boldsymbol{\varphi}\times\boldsymbol{\sigma}\,\mathrm{d}v = \boldsymbol{0}. \tag{3.28}$$

Inserting Eq. (3.24) into Eq. (3.28) leads to

$$\int_{\boldsymbol{\varphi}(\Omega_0)} \operatorname{grad}\boldsymbol{\varphi} \times \boldsymbol{\sigma}\, \mathrm{d}v = \mathbf{0}, \tag{3.29}$$

and following a straightforward tensor algebra, the local form of the conservation of the angular momentum is written as

$$\boldsymbol{I} \times \boldsymbol{\sigma} = \mathbf{0}. \tag{3.30}$$

Eq. (3.30) implies $\boldsymbol{\sigma} = \boldsymbol{\sigma}^{\mathrm{T}}$ which is know as Cauchy's second law of motion. Note that in Eqs. (3.28-3.30), the cross product of two second-order tensor ($\boldsymbol{A}_1$, $\boldsymbol{A}_2$) is defined as

$$\boldsymbol{A}_1 \times \boldsymbol{A}_2 = \mathbb{I} : (\boldsymbol{A}_1 \cdot \boldsymbol{A}_2^{\mathrm{T}}), \tag{3.31}$$

where $\mathbb{I}$ denotes the third-order isotropic tensor.

3.2.3 Conservation of energy

One of the principal laws of thermodynamics is the conservation of energy. It is empirically understood that the total energy of a closed system is conserved over time. Despite the total energy, different forms of energy are not conserved. The energy of a thermo-mechanical system consists of thermal Q, kinetic K and internal energy E_{int}. Though the total amount of the energy is conserved, dealing with the rate form of the energy balance is more practical in mechanical problems. For a quasi-static condition where $\dot{K} = 0$, the law of energy conservation reads

$$\overset{\circ}{E}_{\mathrm{int}} = P_{\mathrm{ext}} + \overset{\circ}{Q}, \tag{3.32}$$

where P_{ext} is the power expended by forces applied to the body $\boldsymbol{\varphi}(\Omega)$, which can be computed as

$$P_{\mathrm{ext}} = \int_{\boldsymbol{\varphi}(\Omega_0)} \rho \boldsymbol{b} \cdot \dot{\boldsymbol{\varphi}}\, \mathrm{d}v + \int_{\boldsymbol{\varphi}(\partial\Omega_0)} \boldsymbol{t}^* \cdot \dot{\boldsymbol{\varphi}}\, \mathrm{d}a. \tag{3.33}$$

The rate of change of the thermal energy is given as

$$\overset{\circ}{Q} = \int_{\boldsymbol{\varphi}(\Omega_0)} \rho g\, \mathrm{d}v - \int_{\boldsymbol{\varphi}(\partial\Omega_0)} \boldsymbol{q} \cdot \boldsymbol{n}\, \mathrm{d}a \tag{3.34}$$

Here, g denotes the material heat-source density and $\boldsymbol{q} \cdot \boldsymbol{n}$ depending on the normal vector $\boldsymbol{n}$ of the hyperplane $\boldsymbol{\varphi}(\partial\Omega)$ is the outward material heat flux.

It should be emphasized that the variable $\overset{\circ}{Q}$ has to be understood as defined by Eq. (3.34) and it is not necessarily the time derivative of a function Q, cf. Stein & Barthold (1995). The remaining term of Eq. (3.32) is the rate of the internal energy E. According to experimental evidence, the integral of $\overset{\circ}{E}$ over a time period is path-independent. Thus, the existence of a material internal energy density potential u per unit mass can be justified and hence, the total internal energy is written as

$$E_{\text{int}}(\boldsymbol{\varphi}(\Omega_0)) = \int\limits_{\boldsymbol{\varphi}(\Omega_0)} \rho u \, \mathrm{d}v. \tag{3.35}$$

Therefore, the rate of internal energy is simplified to the time derivative of Eq. (3.35), i.e., $\overset{\circ}{E} = \dot{E}$. Finally, using the divergence theorem, conservation of linear momentum and assuming sufficiently smooth solutions, the balance law of energy is given by

$$\rho \dot{u} = \boldsymbol{\sigma} : \boldsymbol{l} + \rho g - \operatorname{div} \boldsymbol{q}, \tag{3.36}$$

where

$$\boldsymbol{l} = \dot{\boldsymbol{F}} \cdot \boldsymbol{F}^{-1}, \tag{3.37}$$

is the velocity gradient.

3.2.4 Balance of entropy

In statistical mechanics entropy is the measure of disorder of a system. Based on the second law of thermodynamics the entropy of a closed system increases during an irreversible process and remains conserved for a reversible process. In other words, the balance of entropy defines the direction of a thermodynamical process. Following Coleman & Gurtin (1967); Truesdell & Noll (1965a), at absolute temperature θ, the second law of the thermodynamics states that the rate of entropy in a system is never smaller than the rate of entropy due to heat. This can be written as

$$\frac{\mathrm{d}}{\mathrm{d}t} \int\limits_{\boldsymbol{\varphi}(\Omega_0)} \rho \hat{s} \, \mathrm{d}v \geq \int\limits_{\boldsymbol{\varphi}(\Omega_0)} \frac{\rho g}{\theta} \, \mathrm{d}v - \int\limits_{\boldsymbol{\varphi}(\partial\Omega_0)} \frac{\boldsymbol{q} \cdot \boldsymbol{n}}{\theta} \, \mathrm{d}a, \tag{3.38}$$

where $\hat{s}$ is the entropy density function of a unit mass of the material body in the current configuration. Using the divergence theorem and assuming a sufficiently smooth solution, the local form of Eq. (3.38) is written as

$$\rho \dot{\hat{s}} - \frac{\rho g}{\theta} + \operatorname{div} \frac{\boldsymbol{q}}{\theta} \geq 0. \tag{3.39}$$

Another way of expressing the second law of thermodynamics which is more popular in constitutive modeling of materials is the Clausius-Duhem inequality. Unlike Eq. (3.38), the Clausius-Duhem inequality is expressed in terms of the Helmholtz energy. More precisely, by defining the Helmholtz energy ψ through a Legendre-Fenchel transformation of the type

$$\psi(\bullet,\theta) = \inf_{\hat{s}} \left\{ u(\bullet,\hat{s}) - \left(\frac{\partial u}{\partial \hat{s}} \right) \hat{s} \right\}, \tag{3.40}$$

the Clausius-Duhem inequality reads

$$\boldsymbol{\sigma} : \boldsymbol{l} - \rho \left(\dot{\theta}\hat{s} + \dot{\psi} \right) - \frac{1}{\theta} \boldsymbol{q} \cdot \mathrm{grad}\theta \geq 0. \tag{3.41}$$

If a Fourier-type heat transfer model is assumed or if $\mathrm{grad}\theta = 0$, a sufficient condition of Eq. (3.41) is provided by the well know Clausius-Planck inequality, i.e.,

$$\boldsymbol{\sigma} : \boldsymbol{l} - \rho \left(\dot{\theta}\hat{s} + \dot{\psi} \right) \geq 0. \tag{3.42}$$

By introducing the stress tensor in the initial configuration (the first Piola-Kirchhoff stress tensor)

$$\boldsymbol{P} = \det\boldsymbol{F}\ \boldsymbol{\sigma} \cdot \boldsymbol{F}^{-\mathrm{T}}, \tag{3.43}$$

as well as the entropy density function of unit mass of the material body in the initial configuration $\hat{S}$, the Lagrangian description of the Clausius-Planck inequality can be given as

$$\boldsymbol{P} : \dot{\boldsymbol{F}} - \rho_0 \left(\dot{\theta}\hat{S} + \dot{\psi}_0 \right) \geq 0, \tag{3.44}$$

see Truesdell & Noll (1965b); Simo (1998); Mosler (2007).

4 Constitutive modeling

Based on the kinematic relations and the balance laws reviewed in the previous chapter, the fundamentals of material modeling are presented here. Initially, reversible (elastic) deformation is analyzed. However, since the focus of this thesis is on the deformation of metallic materials (particularly magnesium), irreversible (plastic) deformations cannot be neglected. They are described by introducing a set of internal state variables, see Section 4.2.

4.1 Hyperelasticity

If the work of deformation,

$$\mathcal{W} = \int_t^{t+\Delta t} \mathcal{P}\ \mathrm{d}t = \int_t^{t+\Delta t} \boldsymbol{P} : \dot{\boldsymbol{F}} \mathrm{d}t = \int_{\boldsymbol{F}_t}^{\boldsymbol{F}_{t+\Delta t}} \boldsymbol{P} : \mathrm{d}\boldsymbol{F} \tag{4.1}$$

is path-independent, the corresponding material is called *hyperelastic*. Consequently, a potential Ψ exists such that

$$\boldsymbol{P} = \frac{\partial \Psi(\boldsymbol{F})}{\partial \boldsymbol{F}} \quad \text{and} \quad \dot{\Psi} = \boldsymbol{P} : \dot{\boldsymbol{F}}. \tag{4.2}$$

By inserting Eq. (4.2) into Clausius-Planck inequality (Eq. 3.44), the identity

$$\Psi(\boldsymbol{F}) = \rho_0 \psi_0(\boldsymbol{F}) \tag{4.3}$$

is obtained. It implies that hyperelasticity can be uniquely defined by the Helmholtz free energy (a scalar-valued potential). It is possible to define the Helmholtz energy as function of the right Green-Cauchy strain tensor,

$$\Psi(\boldsymbol{C}) = \Psi(\boldsymbol{F}^{\mathrm{T}} \cdot \boldsymbol{F}), \tag{4.4}$$

thereby Eq. (4.4) satisfies the objectivity principle. For a detailed discussion about the implication induced by the principle of objectivity, see, for instance, Ciarlet (1988). According to Eq. (4.2), the first Piola-Kirchhoff stress tensor can be computed as

$$\boldsymbol{P} = \frac{\partial \Psi(\boldsymbol{C})}{\partial \boldsymbol{F}} = \frac{\partial \Psi(\boldsymbol{C})}{\partial \boldsymbol{C}} : \frac{\partial \boldsymbol{C}}{\partial \boldsymbol{F}} = 2\boldsymbol{F} \cdot \frac{\partial \Psi(\boldsymbol{C})}{\partial \boldsymbol{C}}. \tag{4.5}$$

Due to the fact that $\boldsymbol{C}$ is a symmetric tensor, the partial derivative of the scalar-valued function $\Psi(\boldsymbol{C})$ with respect to $\boldsymbol{C}$ can be represented by a symmetric tensor. By virtue of Eq. (3.43), it can be shown that

$$\boldsymbol{P} \cdot \boldsymbol{F}^{\mathrm{T}} = 2\boldsymbol{F} \cdot \frac{\partial \Psi(\boldsymbol{C})}{\partial \boldsymbol{C}} \cdot \boldsymbol{F}^{\mathrm{T}} = \boldsymbol{F} \cdot \boldsymbol{P}^{\mathrm{T}}, \tag{4.6}$$

which implies that the balance of angular momentum and consequently Eq. (3.26) and Eq. (3.30) are automatically fulfilled. Note that in Eq. (4.6), the standard permutation of tensors in a scalar product is applied, i.e., $(\boldsymbol{A}_1 \cdot \boldsymbol{A}_2 : \boldsymbol{A}_3 \cdot \boldsymbol{A}_4 = \boldsymbol{A}_2 \cdot \boldsymbol{A}_4^{\mathrm{T}} : \boldsymbol{A}_1^{\mathrm{T}} \cdot \boldsymbol{A}_3)$, cf. Levitas (1998).

4.1.1 Examples

In this work, two different hyperelastic material models are considered. In both cases, isotropy of material is assumed.

4.1.1.1 St. Venant-Kirchhoff model

The St. Venant-Kirchhoff model is one of the simplest hyperelastic material models. In this model the elastic stored energy is defined by

$$\Psi(\boldsymbol{E}) = \frac{1}{2}\boldsymbol{E} : \mathbb{K} : \boldsymbol{E}. \tag{4.7}$$

Here, $\boldsymbol{E}(\boldsymbol{C})$ is the Green-Lagrangian strain tensor (Eq. (3.12)) and $\mathbb{K}$ is the fourth-order stiffness tensor. In the case of isotropic materials, Eq. (4.7) can be written as

$$\Psi(\boldsymbol{E}) = \frac{\lambda_{\mathrm{E}}}{2} (\boldsymbol{I} : \boldsymbol{E})^2 + \mu \boldsymbol{I} : \boldsymbol{E}^2. \tag{4.8}$$

In Eq. (4.8), $\{\lambda_{\mathrm{E}}, \mu\}$ are the Lamè parameters.

Remark 6 *It is evident that the material model given by Eq. (4.8) does not satisfy the physical constrains regarding extreme loading condition such as infinite stress for infinite compression, see Ciarlet (1988); Kintzel (2007); Mosler (2008).*

4.1.1.2 neo-Hooke model

The neo-Hookean hyperelastic material models were developed to cover large non-linear elastic deformations, see Simo & Pister (1984); Ciarlet (1988). One

frequently used material model falling into this range of such constitutive laws is given by the Helmholtz energy

$$\Psi(\boldsymbol{C}) = \frac{\lambda_{\mathrm{E}}}{2}(\ln(J))^2 - \mu \ln(J) + \frac{\mu}{2}(\mathrm{tr}(\boldsymbol{C}) - 3). \tag{4.9}$$

Note that the existence of solutions depends on convexity of the strain energy function. This will be explained in more detail is Chapter 5.

Remark 7 *Given Eq. (4.9) depends only on the stretch tensor* ($\boldsymbol{C} = \boldsymbol{U}^2$)*, it satisfies the principle of objectivity. Moreover, in the case of infinite compression* ($J \to 0^+$)*, or infinite stretching* ($\{||\boldsymbol{F}|| + ||\mathrm{Cof}\boldsymbol{F}|| + \det \boldsymbol{F}\} \to \infty^+$)*, the elastic strain energy tends to infinity – as required by physics.*

4.2 Crystal plasticity theory

Elasticity theory exclusively deals with fully reversible deformation processes. Ideal elasticity in engineering materials, in the sense of non-dissipative processes, has been only observed in whiskers wires, see Yoshida et al. (1968). Due to the fact that microstructures of materials are not perfectly ordered and comprise defects, the total deformation recovers only partly after being fully unloaded. The non-reversible part is related to the change in the state of internal defects (Chapter 2). For instance, motion of dislocation and annihilation on the surface (or trapped inside the lattice) result in a class of non-reversible deformation. Another classical example is failure of materials due to initiation and growth of micro-cracks. In Section 4.2.1, a brief review of continuum models describing the plastic behavior of metallic materials (crystal plasticity) is given. Detailed information can be found in the pioneering work by Rice (1971) and Asaro & Rice (1977); Asaro (1983); Asaro & Needleman (1985); Cuitiño & Ortiz (1992); Ortiz & Repetto (1999); Miehe et al. (2002). A variational reformulation of the crystal plasticity model in Section 4.3 is also discussed. Although such a framework is not frequently applied, it is already relatively well developed. Further details concerning the variational structure of plasticity theory can be found, e.g., in Ortiz & Stainier (1999); Mosler & Bruhns (2009b).

4.2.1 Fundamentals of crystal plasticity theory

For the modeling of inelastic processes such as those related to dislocation slip, a nowadays standard multiplicative decomposition of the deformation gradient is adopted. More precisely, with

$$\boldsymbol{F} = \boldsymbol{F}^{\mathrm{e}} \cdot \boldsymbol{F}^{\mathrm{p}} \;\text{ with }\; \det(\boldsymbol{F}^{\mathrm{e}}) > 0 \text{ and } \det(\boldsymbol{F}^{\mathrm{p}}) > 0, \tag{4.10}$$

the deformation gradient $\boldsymbol{F} = \mathrm{GRAD}\boldsymbol{\varphi}(\boldsymbol{X})$ is decomposed into a plastic part $\boldsymbol{F}^{\mathrm{p}}$, which transforms the reference body to an intermediate, incompatible, stress-free configuration, and an elastic part $\boldsymbol{F}^{\mathrm{e}}$ corresponding to the elastic distortion Lee (1969). Hardening effects are taken into account by means of a finite set of strain-like internal variables $\boldsymbol{\lambda} \subset \mathbb{R}^n$. Obviously, those variables are related to the accumulated shear strain caused by dislocation slip, cf. Lubliner (1972); Ortiz & Repetto (1999). With the aforementioned definitions and by assuming isothermal conditions, a Helmholtz energy of the type

$$\Psi = \Psi(\boldsymbol{F}, \boldsymbol{\lambda}) \tag{4.11}$$

is postulated, cf. Lubliner (1972, 1997); Simo & Hughes (1998). Since the elastic stored energy depends only on the elastic distortion (the elastic response of a solid is not affected by plastic deformations), the Helmholtz energy can be additively decomposed into an elastic part Ψ^{e} and a plastic part Ψ^{p} corresponding to plastic work. Combining this with the principle of material frame indifference, the stored energy can, thus, be written as

$$\Psi = \Psi^{\mathrm{e}}(\boldsymbol{C}^{\mathrm{e}}) + \Psi^{\mathrm{p}}(\boldsymbol{\lambda}). \tag{4.12}$$

Here and henceforth, $\boldsymbol{C}^{\mathrm{e}} := \boldsymbol{F}^{\mathrm{e}T} \cdot \boldsymbol{F}^{\mathrm{e}}$ is the elastic right Cauchy-Green tensor. In what follows, Ψ^{p} is further decomposed into a part $\Psi^{\mathrm{p}}_{\mathrm{self}}$ related to self hardening and $\Psi^{\mathrm{p}}_{\mathrm{lat}}$ associated with latent hardening, i.e.,

$$\Psi^{\mathrm{p}} = \Psi^{\mathrm{p}}_{\mathrm{self}} + \Psi^{\mathrm{p}}_{\mathrm{lat}}. \tag{4.13}$$

While the elastic response of a single crystal is completely defined by assuming a physically sound energy Ψ^{e}, plastic deformations require, in addition to the energy Ψ^{p}, suitable evolution equations fulfilling the second law of thermodynamics. For deriving those evolution equations, the Clausius-Planck dissipation inequality

$$\mathcal{D} = \boldsymbol{P} : \dot{\boldsymbol{F}} - \dot{\Psi} = \boldsymbol{S} : \frac{1}{2}\dot{\boldsymbol{C}} - \dot{\Psi} \geq 0 \tag{4.14}$$

is considered, cf. Coleman (1964). In Eq. (4.14), $\boldsymbol{P}$ and $\boldsymbol{S}$ are the first and second Piola-Kirchhoff stress tensors and the superimposed dot denotes the material time derivative. Applying the Coleman & Noll procedure to elastic unloading (Coleman, 1964), yields the elastic response

$$\boldsymbol{S} = 2\frac{\partial \Psi}{\partial \boldsymbol{C}} = 2(\boldsymbol{F}^{\mathrm{p}})^{-1} \cdot \frac{\partial \Psi}{\partial \boldsymbol{C}^{\mathrm{e}}} \cdot (\boldsymbol{F}^{\mathrm{p}})^{-\mathrm{T}} \tag{4.15}$$

and finally, by inserting Eq. (4.15) into the Clausius-Planck inequality (4.14), the reduced dissipation inequality

$$\mathcal{D} = \boldsymbol{\Sigma} : \boldsymbol{l}^{\mathrm{p}} + \boldsymbol{Q} \cdot \dot{\boldsymbol{\lambda}} \geq 0 \tag{4.16}$$

with $\boldsymbol{\Sigma} := 2\boldsymbol{C}^{\mathrm{e}} \cdot \partial_{\boldsymbol{C}^{\mathrm{e}}} \Psi^{\mathrm{e}}$ being the Mandel stresses (Mandel, 1972), $\boldsymbol{l}^{\mathrm{p}} := \dot{\boldsymbol{F}}^{\mathrm{p}} \cdot (\boldsymbol{F}^{\mathrm{p}})^{-1}$ denoting the plastic velocity gradient (with respect to the intermediate configuration) and $\boldsymbol{Q}$ being a set of stress-like internal variables conjugate to the strain-like internal variable $\boldsymbol{\lambda}$, i.e.,

$$\boldsymbol{Q} = -\frac{\partial \Psi}{\partial \boldsymbol{\lambda}}. \tag{4.17}$$

For the modeling of isotropic hardening in single crystals, the vector $\boldsymbol{Q}$ contains n stress-like internal variables corresponding to the admissible slip systems, i.e., $\boldsymbol{Q} = [Q^{(1)}, \dots Q^{(n)}]$. Each of those is defined according to

$$Q^{(a)} = -\partial_{\lambda^{(a)}} \Psi^{\mathrm{p}} = -\frac{\Psi^{\mathrm{p}}_{\mathrm{self}}}{\partial \lambda^{(a)}} - \frac{\Psi^{\mathrm{p}}_{\mathrm{lat}}}{\partial \lambda^{(a)}} = Q^{(a)}_{\mathrm{self}} + Q^{(a)}_{\mathrm{lat}} \tag{4.18}$$

where $\lambda^{(a)}$ is the strain-like internal variable conjugate to $Q^{(a)}$. For providing certain loading conditions, i.e., deciding whether elastic unloading or plastic loading occurs, an admissible stress space $\mathbb{E}_{\boldsymbol{\sigma}}$

$$\mathbb{E}_{\boldsymbol{\sigma}} = \left\{ (\boldsymbol{\Sigma}, \boldsymbol{Q}) \in \mathbb{R}^{9+n} \;\middle|\; \phi^{(a)}(\boldsymbol{\Sigma}, Q^{(a)}) \leq 0,\ a = 1, ..., n \right\} \tag{4.19}$$

is introduced. It is defined by n convex yield functions $\phi^{(a)}$. Each of those is associated with a certain slip system within the respective single crystal and assumed to be governed by Schmid's law. More explicitly,

$$\phi^{(a)}(\boldsymbol{\Sigma}, \boldsymbol{\lambda}) = |\boldsymbol{\Sigma} : \boldsymbol{N}^{(a)}| - (\Sigma_0^{(a)} - Q^{(a)}(\boldsymbol{\lambda})). \tag{4.20}$$

Accordingly, the applied resolved shear stress at slip system a (the slip activation force) computed by projecting the Mandel stresses $\boldsymbol{\Sigma}$ onto the slip plane using the Schmid tensor $\boldsymbol{N}^{(a)} := (\boldsymbol{s}^{(a)} \otimes \boldsymbol{m}^{(a)})$ is compared to the material's current strength which, is decomposed into an initial yield stress $\Sigma_0^{(a)}$ and an additional hardening term $Q^{(a)}$. The time invariant orthogonal unit vectors $\boldsymbol{m}^{(a)}$ and $\boldsymbol{s}^{(a)}$ correspond to the normal of the slip plane and the direction of the plastic shear strain, respectively.

By combining dissipation inequality (4.16) with the space of admissible stresses (4.19), physically sound evolution equations can be derived. For that purpose, the postulate of maximum dissipation is considered here, cf. Hill (1972). A straightforward computation yields in this case

$$\begin{aligned} \boldsymbol{l}^{\mathrm{p}} &= \sum_{a=1}^{n} \varsigma^{(a)} \ \frac{\partial \phi^{(a)}}{\partial \boldsymbol{\Sigma}} \\ &= \sum_{a=1}^{n} \varsigma^{(a)} \ \mathrm{sign}[\boldsymbol{\Sigma} : \boldsymbol{N}^{(a)}] \ \boldsymbol{N}^{(a)} \quad \text{and} \quad \dot{\lambda}^{a} = \varsigma^{(a)} \ \frac{\partial \phi^{(a)}}{\partial Q^{(a)}} = \varsigma^{(a)}, \end{aligned} \tag{4.21}$$

together with the Karush-Kuhn-Tucker optimality conditions

$$\varsigma^{(a)} \geq 0 \ , \ \varsigma^{(a)} \ \phi^{(a)} = 0, \tag{4.22}$$

cf. Rice (1971); Luenberger (1984). In Eqs. (4.21)–(4.22), $\varsigma^{(a)}$ is the plastic multiplier associated with slip system a. It can be computed from the consistency conditions $\dot{\phi}^{(a)} = 0$. By inserting Eq. (4.21) into the dissipation inequality (4.16), the dissipation is obtained as

$$\begin{aligned} \mathcal{D} &= \sum_{a=1}^{n} \varsigma^{(a)} \ \Big[\text{sign}[\boldsymbol{\Sigma} : \boldsymbol{N}^{(a)}] \ (\boldsymbol{\Sigma} : \boldsymbol{N}^{(a)}) + Q^{(a)} \Big] \\ &\overset{\phi^a = 0}{=} \sum_{a=1}^{n} \varsigma^{(a)} \ \Sigma_0^{(a)} \geq 0. \end{aligned} \tag{4.23}$$

Since $\Sigma_0^{(a)} > 0$ and $\varsigma^{(a)} \geq 0$, the second law of thermodynamics is indeed fulfilled. The closed form expression for the dissipation is a direct consequence of the positive homogeneity of the equivalent stresses $|\boldsymbol{\Sigma} : (\boldsymbol{s}^{(a)} \otimes \boldsymbol{m}^{(a)})|$.

4.3 A variational reformulation of crystal plasticity theory

A variational reformulation of crystal plasticity theory discussed before is addressed here. For this theory and following Ortiz & Stainier (1999); Mosler & Bruhns (2009b), the stress power is given by

$$\tilde{\mathcal{E}}(\dot{\boldsymbol{\varphi}}, \dot{\boldsymbol{F}}^{\text{p}}, \dot{\boldsymbol{\lambda}}, \boldsymbol{\Sigma}, \boldsymbol{Q}) = \dot{\Psi}(\dot{\boldsymbol{\varphi}}, \dot{\boldsymbol{F}}^{\text{p}}, \dot{\boldsymbol{\lambda}}) + \mathcal{D}(\dot{\boldsymbol{\lambda}}) + J(\boldsymbol{\Sigma}, \boldsymbol{Q}) \tag{4.24}$$

Here, the characteristic function of the admissible stress space

$$J := \begin{cases} 0 & \forall (\boldsymbol{\Sigma}, \boldsymbol{Q}) \in \mathbb{E}_\sigma \\ \infty & \text{otherwise} \end{cases} \tag{4.25}$$

has been introduced. Accordingly, J penalizes the functional (4.24) for inadmissible stress states. It can be shown that the stationarity conditions of functional (4.24) are equivalent to the crystal plasticity model discussed in the previous section, cf. Carstensen et al. (2002), i.e.,

$$\begin{aligned} \partial_{\boldsymbol{\Sigma}} \tilde{\mathcal{E}} = 0 &\Rightarrow \boldsymbol{l}^{\text{p}} = \sum_{a=1}^{n} \varsigma^{(a)} \ \frac{\partial \phi^{(a)}}{\partial \boldsymbol{\Sigma}} \\ \partial_{\boldsymbol{Q}} \tilde{\mathcal{E}} = 0 &\Rightarrow \dot{\lambda}^a = \varsigma^{(a)} \ \frac{\partial \phi^{(a)}}{\partial Q^{(a)}} \\ \partial_{\dot{\lambda}^{(a)}} \tilde{\mathcal{E}} = 0 &\Rightarrow Q^{(a)} = -\partial_{\lambda^{(a)}} \Psi^{\text{p}} \\ \partial_{\dot{\boldsymbol{F}}^{\text{p}}} \tilde{\mathcal{E}} = 0 &\Rightarrow \boldsymbol{\Sigma} = 2 \, \boldsymbol{C}^{\text{e}} \cdot \partial_{\boldsymbol{C}^{\text{e}}} \Psi^{\text{e}}. \end{aligned} \tag{4.26}$$

Hence, this stationarity problem represents a variational reformulation of crystal plasticity theory. By enforcing the postulate of maximum dissipation (maximization with respect to the stress-like variables) the reduced stress power, now a function in terms of strain-like variables only, reads

$$\mathcal{E}(\dot{\boldsymbol{\varphi}}, \dot{\boldsymbol{F}}^{\mathrm{p}}, \dot{\boldsymbol{\lambda}}) = \dot{\Psi}(\dot{\boldsymbol{\varphi}}, \dot{\boldsymbol{F}}^{\mathrm{p}}, \dot{\boldsymbol{\lambda}}) + J^*(\dot{\boldsymbol{F}}^{\mathrm{p}}, \dot{\boldsymbol{\lambda}}). \tag{4.27}$$

Here, J^* is the Legendre transformation of the characteristic function J. Physically speaking and considering associative evolution equations, it is the dissipation.

Interestingly and in contrast to the stationarity problem stat$\tilde{\mathcal{E}}$, the crystal plasticity model described in the previous subsection can now be formulated as a minimization problem of the type $\inf \mathcal{E}$. More precisely, the evolution equations (4.21) are equivalent to

$$(\dot{\boldsymbol{F}}^{\mathrm{p}}, \dot{\boldsymbol{\lambda}}) = \arg \inf_{\dot{\boldsymbol{F}}^{\mathrm{p}}, \dot{\boldsymbol{\lambda}}} \mathcal{E}(\dot{\boldsymbol{\varphi}}, \dot{\boldsymbol{F}}^{\mathrm{p}}, \dot{\boldsymbol{\lambda}}). \tag{4.28}$$

Minimization principle (4.28) gives rise to the introduction of the reduced functional

$$\hat{\mathcal{E}}(\dot{\boldsymbol{\varphi}}) := \inf \mathcal{E} = \boldsymbol{P} : \dot{\boldsymbol{F}}. \tag{4.29}$$

Accordingly and in line with hyperelastic materials, this pseudo potential defines the stress response, i.e,

$$\boldsymbol{P} = \partial_{\dot{\boldsymbol{F}}} \hat{\mathcal{E}}. \tag{4.30}$$

Remark 8 *In case of rate-independent plasticity theory, the dissipation is a positively homogeneous function of degree one, cf. Ortiz & Stainier (1999); Hackl & Fischer (2008) (see also Eq. (4.23)). In the present chapter, it followed from a Legendre-Fenchel transformation applied to the characteristic function of the space of admissible stresses, see Mosler & Bruhns (2009a); Homayonifar & Mosler (2011). Thus, it depends on the underlying yield function representing the primary assumption. By way of contrast, the dissipation and the flow rule represent the primary variables in Ortiz & Stainier (1999); Ortiz & Repetto (1999) and the yield function is derived from them. Both methods are connected through a Legendre-Fenchel transformation. Therefore, they are essentially equivalent for rate-independent processes. However, depending on the application, one of these methods can be advantageous. For instance, the approach advocated in Ortiz & Stainier (1999); Ortiz & Repetto (1999) will be chosen for elaborating the model suitable for the analysis of deformation-induced twinning.*

4.3.1 Numerical implementation - Variational constitutive updates

Based on minimization principle (4.28), effective numerical implementations can be developed, Ortiz & Repetto (1999); Carstensen et al. (2002); Miehe (2002); Mosler & Cirak (2009). For that purpose, a time discretization of the continuously defined functional (4.27) of the type

$$I_{\text{inc}} = \int_{t_n}^{t_{n+1}} \tilde{\mathcal{E}} \, \mathrm{d}t = \Psi_{n+1} - \Psi_n + \sum_{a=1}^{n} \Delta\varsigma^{(a)} \, \Sigma_0^{(a)}, \quad \Delta\varsigma^{(a)} := \int_{t_n}^{t_{n+1}} \varsigma^{(a)} \, \mathrm{d}t \tag{4.31}$$

is considered. Here, t_n and t_{n+1} are two pseudo times. For computing the Helmholtz energy Ψ at time t_{n+1}, the plastic part of the deformation gradient is approximated by means of an exponential integration scheme, while a classical backward Euler discretization is applied to the strain-like internal variables, i.e.,

$$\boldsymbol{F}_{n+1}^{\text{p}} = \exp(\Delta t \; \boldsymbol{l}^{\text{p}}) \cdot \boldsymbol{F}_n^{\text{p}} \; , \; \lambda_{n+1}^a = \lambda_n^a + \Delta\varsigma^{(a)}. \tag{4.32}$$

Inserting these approximations into Eq. (4.31), together with the flow rule (4.21), the incrementally defined functional I_{inc} depends on the unknown slip rates (discrete increments) as well as on the current deformation gradient (the old state is known in numerical schemes such as the finite element method). As a consequence,

$$I_{\text{inc}} = I_{\text{inc}}(\boldsymbol{F}_{n+1}, \Delta\varsigma^{(1)}, \ldots, \Delta\varsigma^{(n)}). \tag{4.33}$$

Based on this functional, the slip rates can be computed according to

$$(\Delta\varsigma^{(1)}, \ldots, \Delta\varsigma^{(n)}) = \arg \inf_{\Delta\varsigma^{(1)}, \ldots, \Delta\varsigma^{(n)}} I_{\text{inc}}|_{\boldsymbol{F}_{n+1}} \tag{4.34}$$

and finally, the stresses are defined by

$$\boldsymbol{P} = \partial_{\boldsymbol{F}_{n+1}} \inf_{\Delta\varsigma^{(1)}, \ldots, \Delta\varsigma^{(n)}} I_{\text{inc}}. \tag{4.35}$$

In addition to its physical and mathematical elegance, the variational constitutive update presented here shows further advantages. For instance, the determination of the set of the active slip systems is naturally included within the optimization problem and thus, sophisticated regularization techniques such as those in Schmidt-Baldassari (2003); McGinty & McDowell (2006); Zamiri et al. (2007) are not required. Even more importantly, energy principles provide a physically sound basis for coupling different models, cf. Mosler & Cirak (2009), i.e., the energetically most favorable combination between the respective models is considered. Such a canonical coupling is also proposed in the present thesis for combining plastic slip and deformation-induced twinning.

5 Convex analysis

In the previous chapter, a variational framework for crystal plasticity theory based on energy minimization was discussed. The existence of the solution of such a variational problem is strongly related to the convexity of the internal energy (Ψ). Interestingly, convexity conditions are connected to microstructures in materials. For instance, in the late twentieth century, the evolution of the material microstructure has been explained based on a certain class of convex energy functions, see Ericksen (1979); Ball & James (1987); Ortiz & Repetto (1999). Accordingly, the current chapter is devoted to give a brief review of the general concept of convexity suitable for the constitutive modeling of materials. For more detailed studies, the reader is referred to Morrey (1952); Rockafellar (1970); Ball (1977); Ciarlet (1988); Dacorogna (2008); Schröder & Neff (2010).

5.1 Convexity

A function $\Psi(\boldsymbol{F})$ is convex if for any $\lambda \in [0,1]$ and $\forall\ \boldsymbol{F} \in \mathcal{R}^{n\times n}$

$$\Psi\left((1-\lambda)\boldsymbol{F}^{+} + (\lambda)\boldsymbol{F}^{-}\right) \leq (1-\lambda)\Psi(\boldsymbol{F}^{+}) + (\lambda)\Psi(\boldsymbol{F}^{-}). \tag{5.1}$$

A graphical interpretation of Eq. (5.1) is given in Fig. 5.1. Note that Fig. (5.1) is only a schematic illustration since the tensorial deformation field can not be shown. Although a convex energy potential is desired, convexity violates the physical principle of objectivity, see Ciarlet (1988). Thus, the convexity condition of the stored energy function (Ψ) must be ruled out. This condition can be replaced by a more suitable weaker requirement.

5.2 Poly-convexity

A weaker requirement of convexity was proposed in Ball (1977) and Ciarlet (1988). According to these references, a function Ψ is poly-convex, if there exists a function $\hat{\Psi}$ which is convex on the set

$$\mathbb{S} := \{(\boldsymbol{F}, \operatorname{Cof}\boldsymbol{F}, \det \boldsymbol{F})\}, \tag{5.2}$$

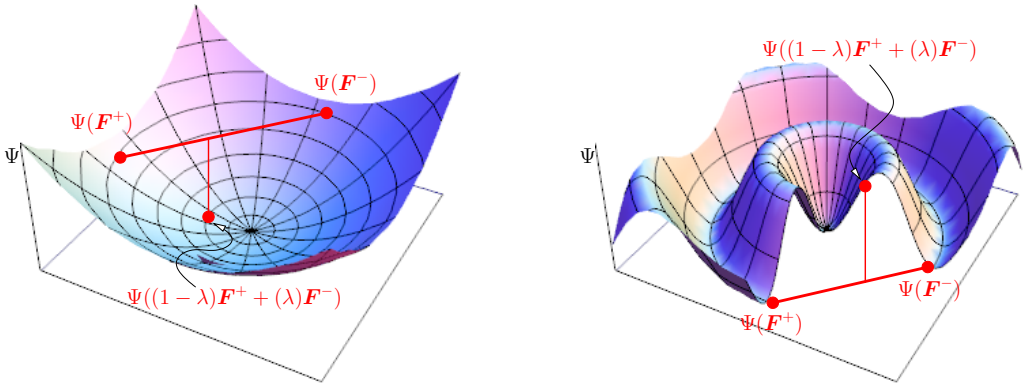

(a) Convex (b) Non-convex

Figure 5.1: A schematic illustration of convexity. The connecting straight line between $\Psi(\boldsymbol{F}^+)$ and $\Psi(\boldsymbol{F}^-)$ is always located above the surface of a convex function, while this does not hold in the case of a non-convex function.

and

$$\Psi(\boldsymbol{F}) = \hat{\Psi}(\boldsymbol{F}, \operatorname{Cof}\boldsymbol{F}, \det \boldsymbol{F}), \tag{5.3}$$

where $\operatorname{Cof}\boldsymbol{F}$ denotes the cofactor of $\boldsymbol{F}$. Note that the geometrical elements in the material configuration (infinitesimal line element $\mathrm{d}\boldsymbol{X}$, area element $\mathrm{d}\boldsymbol{A} = \boldsymbol{N}\mathrm{d}A$ and volume element $\mathrm{d}V$) are transformed to the current configuration using the set $\mathbb{S}$ and the standard transformations:

$$\mathrm{d}\boldsymbol{x} = \boldsymbol{F}\mathrm{d}\boldsymbol{X} \quad , \quad \mathrm{d}\boldsymbol{a} = \boldsymbol{n}\mathrm{d}a = \operatorname{Cof}\boldsymbol{F} \cdot \boldsymbol{N}\mathrm{d}A \quad , \quad \mathrm{d}v = \det \boldsymbol{F}\mathrm{d}V. \tag{5.4}$$

Analogous to Eq. (5.1), Ψ is poly-convex if for any $\lambda \in [0,1]$ and $\forall\ \boldsymbol{F} \in \mathcal{R}^{n\times n}$

$$\begin{aligned} &\Psi\big((1-\lambda)(\boldsymbol{F}, \operatorname{Cof}\boldsymbol{F}, \det \boldsymbol{F})^+ + (\lambda)(\boldsymbol{F}, \operatorname{Cof}\boldsymbol{F}, \det \boldsymbol{F})^-\big) \leq \\ &\quad (1-\lambda)\Psi\big((\boldsymbol{F}, \operatorname{Cof}\boldsymbol{F}, \det \boldsymbol{F})^+\big) + (\lambda)\Psi\big((\boldsymbol{F}, \operatorname{Cof}\boldsymbol{F}, \det \boldsymbol{F})^-\big). \end{aligned} \tag{5.5}$$

According to Dacorogna (2008), although convexity implicates poly-convexity, the converse does not hold, i.e.,

$$\text{poly-convexity} \quad \not\Rightarrow \quad \text{convexity}. \tag{5.6}$$

For instance, $\Psi(\boldsymbol{F}) : \mathcal{R}^{2\times 2} \rightarrow \mathcal{R}$ defined as

$$\Psi(\boldsymbol{F}) := \det \boldsymbol{F} \tag{5.7}$$

is poly-convex, while it is not a convex function. Convexity was also examined earlier by another weaker form of convexity which is quasi-convexity, see Morrey (1952).

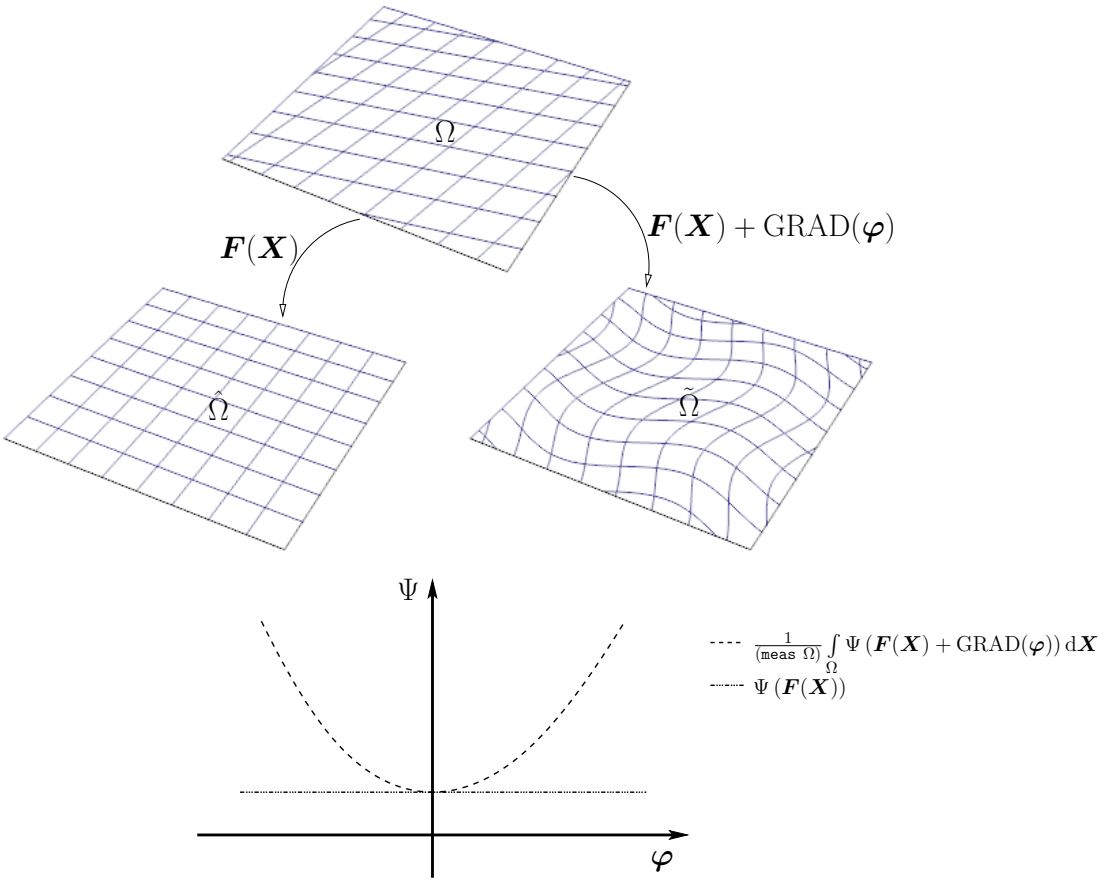

Figure 5.2: A graphical illustration of the concept of quasi-convexity.

5.3 Quasi-convexity

For heterogeneous deformation fields, a convexity condition related to the integrated energy

$$\mathcal{I} := \int_{\Omega} \Psi\left(\boldsymbol{F}(\boldsymbol{X})\right) \mathrm{d}\boldsymbol{X}. \tag{5.8}$$

is more suitable. According to Morrey (1952); Ball (1977, 1986); Dacorogna (2008), sufficient conditions for the existence of minimizers are sequential-weak-lower- semicontinuity and coercivity of Ψ. Morrey (1952) has shown that these conditions are equivalent to the quasi-convexity condition. Let $W^{1,p}(\Omega : \mathcal{R}^m)$ denotes all mappings $\boldsymbol{\varphi} : \Omega \to \mathcal{R}^n$ such that

$$||\boldsymbol{\varphi}||_p + ||\mathrm{GRAD}(\boldsymbol{\varphi})||_p < \infty \tag{5.9}$$

where $||\bullet||_p$ designates the p-norm of $(\bullet)$. And the subset of $W^{1,p}(\Omega : \mathcal{R}^n)$ consisting of those $\boldsymbol{\varphi}$ vanishing on the boundary $\partial\Omega$ is defined by $W_0^{1,p}(\Omega : \mathcal{R}^n)$. Accordingly, a function Ψ is $W^{1,p}$-quasi-convex at $\boldsymbol{F}$, if

$$\Psi(\boldsymbol{F}(\boldsymbol{X})) \leq \frac{1}{(\texttt{meas}\ \Omega)} \int_{\Omega} \Psi\left(\boldsymbol{F}(\boldsymbol{X}) + \mathrm{GRAD}(\boldsymbol{\varphi})\right) \mathrm{d}\boldsymbol{X} \tag{5.10}$$

with

$$\boldsymbol{\varphi} \in W_0^{1,p}(\Omega : \mathcal{R}^n) \tag{5.11}$$

where $(\texttt{meas}\ \Omega)$ indicates the Lebesgue measure of Ω. In the case of $p = \infty$ the abbreviation quasi-convex is used instead of $W^{1,p}$-quasi-convex. The graphical interpretation is given in Fig. 5.2 where it is shown that any perturbation in the form of $\mathrm{GRAD}(\boldsymbol{\varphi})$ increases the internal energy. From Eq. (5.11) it can be realized that the quasi-convexity is not a local condition and hence, proving this condition is not straightforward. Although quasi-convexity is a nonlocal condition, it is bounded between two local upper and lower limits, i.e.,

$$\text{poly-convexity} \quad \Rightarrow \quad \text{quasi-convexity} \quad \Rightarrow \quad \text{rank-one-convexity}, \tag{5.12}$$

see Dacorogna (2008); Raoult (2010). The remaining limit being that defined by rank-one-convexity is discussed next.

5.4 Rank-one-convexity

The development of the concept of rank-one-convexity can be motivated by some experimental measurements in which the deformation of materials is governed by sequential laminates. Microscopic observations revealed that the deformation in a certain class of materials is localized within distinct regions such as dislocation laminates in ductile crystals and martensites in shape memory alloys, see Saimoto (1963); Rasmussen & Pedersen (1980); Jin & Winter (1984); Ball & James (1987). This laminate microstructure can be mathematically explained by a piece-wise continuous deformation field. For instance, under a macroscopic deformation $\boldsymbol{F}$, the material body Ω is transformed to a collection of sequential sub-domains $(\Omega_1^+ \cup \Omega_1^- \cup \Omega_2^+ \cup \Omega_2^- \cup \dots)$ with microscopic deformation fields $(\boldsymbol{F}^+/\boldsymbol{F}^-/\boldsymbol{F}^+/\boldsymbol{F}^-/\dots)$, which fulfill the compatibility conditions

$$\boldsymbol{F} = \lambda^+ \boldsymbol{F}^+ + \lambda^- \boldsymbol{F}^- \quad \text{and} \quad \boldsymbol{F}^- - \boldsymbol{F}^+ = (\boldsymbol{a} \otimes \boldsymbol{n}) \quad \text{where} \quad \{\boldsymbol{a}; \boldsymbol{n}\} \in \mathcal{R}^3 \tag{5.13}$$

and $\lambda^{\pm}$ indicate the volume fraction of each laminate. The Legendre-Hadamard condition implies that the aforementioned laminate configuration is stable

(with respect to the energy Ψ), if it fulfills the strong ellipticity condition. That is, if $\Psi \in C^2$,

$$(\boldsymbol{a} \otimes \boldsymbol{n}) : \frac{\partial^2 \Psi(\boldsymbol{F})}{\partial \boldsymbol{F} \partial \boldsymbol{F}} : (\boldsymbol{a} \otimes \boldsymbol{n}) = \frac{\partial^2 \Psi(\boldsymbol{F})}{\partial F_{ik} \partial F_{jl}} a_i n_k a_j n_l > 0, \tag{5.14}$$

see Ball (2010). Alternatively, if the wavefront ($\partial\Omega := \Omega^+ \cap \Omega^-$) is characterized by $\boldsymbol{n}$, the acoustic tensor

$$\mathbb{A} = \boldsymbol{n} \cdot \frac{\partial^2 \Psi(\boldsymbol{F})}{\partial \boldsymbol{F} \partial \boldsymbol{F}} \cdot \boldsymbol{n} \tag{5.15}$$

must be positive definite, see Hadamard (1903). Ball (1977) showed that the Legendre-Hadamard condition is equivalent to rank-one-convexity condition. This condition states that a function $\Psi(\boldsymbol{F})$ is rank-one-convex for all $\text{rank}(\boldsymbol{F}^- - \boldsymbol{F}^+) \leq 1$ if it satisfies Eq. (5.1).

5.5 Convex hulls

The governing laws of many physical problems are realized by non-convex functions and thus, the existence of solutions can not be expected in the classical sense, cf. Ortiz & Repetto (1999); Carstensen et al. (2002); Miehe & Lambrecht (2003). However, a solution can often nevertheless be accommodated by convex envelops (Dacorogna (2008)) as

- Convex hull

$$\mathrm{C}\Psi = \sup \left\{ \tilde{\Psi} : \tilde{\Psi} \leq \Psi \quad \text{and} \quad \tilde{\Psi} \quad \text{convex} \right\} \tag{5.16}$$

- Poly-convex hull

$$\mathrm{P}\Psi = \sup \left\{ \tilde{\Psi} : \tilde{\Psi} \leq \Psi \quad \text{and} \quad \tilde{\Psi} \quad \text{poly-convex} \right\} \tag{5.17}$$

- Quasi-convex hull

$$\mathrm{Q}\Psi = \sup \left\{ \tilde{\Psi} : \tilde{\Psi} \leq \Psi \quad \text{and} \quad \tilde{\Psi} \quad \text{quasi-convex} \right\} \tag{5.18}$$

- Rank-one-convex hull

$$\mathrm{R}\Psi = \sup \left\{ \tilde{\Psi} : \tilde{\Psi} \leq \Psi \quad \text{and} \quad \tilde{\Psi} \quad \text{rank-one-convex} \right\}. \tag{5.19}$$

One can define the aforementioned hulls alternatively as

- Convex hull

$$\begin{aligned} \mathrm{C}\Psi(\boldsymbol{F}) = \inf \Bigg\{ \sum_{i=1}^{n} \lambda^{\{i\}} \Psi(\boldsymbol{F}^{\{i\}}) \Bigg| \lambda^{\{i\}}, \boldsymbol{F}^{\{i\}}; \lambda^{\{i\}} \in [0,1] \\ \sum_{i=1}^{n} \lambda^{\{i\}} = 1, \sum_{i=1}^{n} \lambda^{\{i\}} \boldsymbol{F}^{\{i\}} = \boldsymbol{F} \Bigg\} \end{aligned} \tag{5.20}$$

- Poly-convex hull

$$\begin{aligned} \mathrm{P}\Psi(\boldsymbol{F}) = \inf \Bigg\{ \sum_{i=1}^{n} \lambda^{\{i\}} \Psi(\boldsymbol{F}^{\{i\}}) \Bigg| \lambda^{\{i\}}, \boldsymbol{F}^{\{i\}}; \lambda^{\{i\}} \in [0,1] \\ \sum_{i=1}^{n} \lambda^{\{i\}} = 1, \sum_{i=1}^{n} \lambda^{\{i\}} \boldsymbol{F}^{\{i\}} = \boldsymbol{F}, \\ \sum_{i=1}^{n} \lambda^{\{i\}} \mathrm{Cof} \boldsymbol{F}^{\{i\}} = \mathrm{Cof} \boldsymbol{F}, \sum_{i=1}^{n} \lambda^{\{i\}} \det \boldsymbol{F}^{\{i\}} = \det \boldsymbol{F} \Bigg\} \end{aligned} \tag{5.21}$$

- Quasi-convex hull

$$\begin{aligned} \mathrm{Q}\Psi(\boldsymbol{F}) = \inf \Bigg\{ \frac{1}{(\mathtt{meas}\ \Omega)} \int_{\Omega} \Psi\left(\boldsymbol{F} + \mathrm{GRAD}(\boldsymbol{\varphi})\right) \mathrm{d}\boldsymbol{X} \Bigg| \boldsymbol{\varphi}; \\ \boldsymbol{\varphi} \in W_0^{1,\infty}(\Omega : \mathcal{R}^n) \Bigg\} \end{aligned} \tag{5.22}$$

- Rank-one-convex hull

$$\begin{aligned} \tilde{\mathrm{R}}\Psi(\boldsymbol{F}) = \inf \Bigg\{ (1-\lambda)\Psi(\boldsymbol{F}^{+}) + (\lambda)\Psi(\boldsymbol{F}^{-}) \Bigg| \lambda, \{\boldsymbol{F}^{+}; \boldsymbol{F}^{-}\}; \\ \lambda \in [0,1], (1-\lambda)\boldsymbol{F}^{+} + (\lambda)\boldsymbol{F}^{-} = \boldsymbol{F}, \\ \mathrm{rank}(\boldsymbol{F}^{-} - \boldsymbol{F}^{+}) \leq 1 \Bigg\}. \end{aligned} \tag{5.23}$$

It is worth mentioning that the rank-one-convex hull ($\tilde{\mathrm{R}}\Psi$) has been widely used to study the formation of microstructures. For instance, phase transitions such as the formation of a martensite, twinning (Ericksen, 1979; James, 1981; Ball & James, 1987; Bhattacharya et al., 1997; Mueller, 1999; Mielke, 2004; Kochmann & Le, 2009) and dislocation microstructures in ductile crystals (Ortiz & Repetto, 1999; Carstensen et al., 2002; Miehe & Lambrecht, 2003) have been explained by using a rank-one-convex energy potential. In these

works, λ and $\{\boldsymbol{F}^{-};\boldsymbol{F}^{+}\}$ are interpreted as being the volume fraction and the deformation gradients of two neighboring phases satisfying the Hadamard compatibility condition at the interface (Eq. (5.13)).

6 Modeling of twinning: solid-solid phase transition

In the previous section, constitutive models suitable for the analysis of dislocation slip were briefly discussed and reformulated within a variationally consistent framework. In the present section, focus is on the solid-solid phase transitions associated with deformation-induced twinning. In line with the previous subsection and for the sake of consistency, the aforementioned phase transition is assumed to be governed by energy minimization, i.e., a twin forms, if this is energetically favorable. While twinning is considered as a certain rank-one convexification in Subsection 6.1, a computationally more efficient approach is elaborated in Subsection 6.2. It is based on decomposing the deformation induced by twinning into a shear strain and the reorientation of the crystal lattice.

6.1 Modeling twinning by rank-one convexification

Twinning is characterized by a laminate structure, cf. James (1981). A powerful mathematical tool for analyzing such problems is provided by the concept of rank-one convexification, cf. Carstensen et al. (2002). Within this concept, the energy of a solid is further minimized by allowing for certain phase-decompositions (microstructures). Continuity of the sub-deformations is guaranteed by enforcing a Hadamard-type (Ball & James, 1987) compatibility condition between the deformation gradients within the different phases.

6.1.1 Kinematics

A twin $\partial\Omega^-$ partitions the initial domain $\Omega \subset \mathbb{R}^3$ into the sub-bodies Ω^+ and Ω^-, i.e., $\Omega = \Omega^+ \cup \Omega^- \cup \partial\Omega^-$. While the crystal lattice in Ω^+ is equivalent to that in Ω, the simple shear parallel to the twin plane $\partial\Omega^-$ changes the crystal lattice in Ω^-. Such a transformation can be described by a proper orthogonal tensor $\boldsymbol{R}$. More precisely, denoting the lattice vectors of the initial phase as $\boldsymbol{e} := \{\boldsymbol{e}_1, \boldsymbol{e}_2, \boldsymbol{e}_3\}$ and those corresponding to the twinned configuration as $\tilde{\boldsymbol{e}}$, the transformation

$$\tilde{\boldsymbol{e}} = \boldsymbol{R} \cdot \boldsymbol{e} \tag{6.1}$$

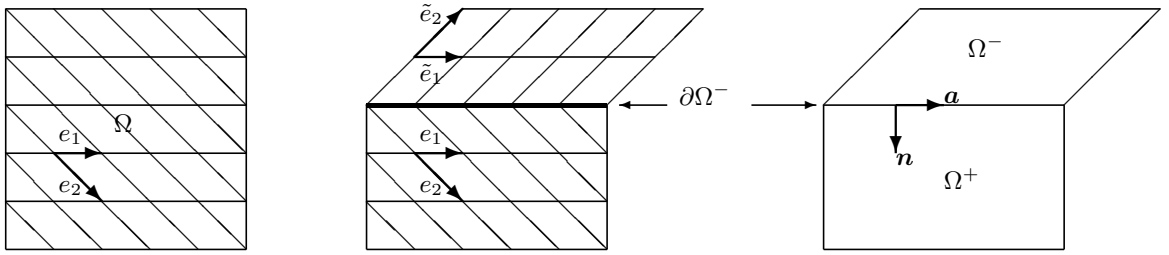

Figure 6.1: Lattice rotation associated with deformation-induced twinning

holds, see Fig. 6.1. With $\boldsymbol{n}$ being the normal vector of the twin interface, $\boldsymbol{R}$ is defined by

$$\boldsymbol{R} = -\boldsymbol{I} + 2(\boldsymbol{n} \otimes \boldsymbol{n}) \text{ with } \det \boldsymbol{R} = 1, \tag{6.2}$$

see Pitteri (1985). Commonly observed microstructures suggest that twinning occurs with laminate topology. Here, a first-order approximation is considered. More precisely and following James (1981); Ortiz & Repetto (1999); Carstensen et al. (2002), the deformation gradient $\boldsymbol{F}^+$ associated with the initial phase Ω^+ and $\boldsymbol{F}^-$ belonging to Ω^- are decomposed according to

$$\boldsymbol{F}^- = \boldsymbol{F}^+ - \lambda_{\mathrm{Twin}}(\boldsymbol{a} \otimes \boldsymbol{n}). \tag{6.3}$$

For guaranteeing a resulting physically reasonable macroscopic strain, the additional compatibility conditions

$$\boldsymbol{F} = \xi^+ \boldsymbol{F}^+ + \xi^- \boldsymbol{F}^- \tag{6.4}$$

and

$$\xi^+ + \xi^- = 1 \tag{6.5}$$

are enforced, see Silhavy (1997). Henceforth, the subscript $(^-)$ is omitted from ξ^-, i.e., ξ denotes the volume fraction of the twinning phase. As evident from Eq. (6.3), the rank-one deformation tensor $\lambda_{\mathrm{Twin}}(\boldsymbol{a} \otimes \boldsymbol{n})$ defines the deformation jump across the twinning interface. In this connection, the normal vector $\boldsymbol{n}$ corresponds to the twinning plane (interface), while $\boldsymbol{a}$ and λ_{Twin} define the jump direction and the amplitude of the shear deformation. In contrast to conventional rank-one convexification (Carstensen et al., 2002), the direction and the amplitude of the twinning shear are a priori prescribed by the respective lattice structure. For instance, in case of magnesium tensile twinning ($\boldsymbol{a} := \langle 10\bar{1}1\rangle, \boldsymbol{n} := \{\bar{1}012\}$), it is obtained as $\lambda_{\mathrm{Twin}} = f(c/a)$, see Christian & Mahajan (1995).

Remark 9 *In general, deformation-induced twinning can occur successively by several twinning variants. In this case, the aforementioned phase decomposition has to be considered several times. However, within the present chapter,*

only first-order laminates will be modeled. Since the resulting approach predicts the mechanical response of magnesium single crystal very well, computationally more expensive higher-order approximations will not be analyzed here.

6.1.2 Energy

According to the previous section, the presence of twin laminates induces deformation fluctuations in the initial phase. More precisely, the deformation gradient decomposes as stated in Eq. (6.3). Consequently, the Helmholtz energy of the whole solid can be described by a volume averaging of the energies associated with each phase, i.e.,

$$\begin{aligned}\Psi_{\mathrm{C}}(\boldsymbol{C}, \boldsymbol{F}^{+\mathrm{p}}, \boldsymbol{\lambda}^{+}, \boldsymbol{F}^{-\mathrm{p}}, \boldsymbol{\lambda}^{-}, \xi) = (1-\xi)\Psi^{+}(\boldsymbol{C}^{+\mathrm{e}}, \boldsymbol{\lambda}^{+}) \\ + \xi\ \Psi^{-}(\boldsymbol{C}^{-\mathrm{e}}, \boldsymbol{\lambda}^{-}) + \Psi^{\mathrm{mix}}(\xi).\end{aligned} \tag{6.6}$$

In Eq. (6.6), an additional mixture energy Ψ^{mix} has been introduced. It primarily depends on the coherency of the neighboring phases in the vicinity of the interface. It vanishes in case of unconstrained twinning, e.g., Fig. 6.1. The purpose of this mixture energy is two-fold. First, as mentioned before, it allows to include interface effects, i.e., it leads to a physically more sound model. Second, by choosing different energies, different approximations of phase transition can be analyzed within a unique framework. For instance, by choosing

$$\Psi^{\mathrm{mix}} = \begin{cases} 0 & \forall \xi \in \{0;1\} \\ \infty & \forall \xi \in (0,1) \end{cases} \tag{6.7}$$

a classical Taylor-type approximation is obtained, i.e., either phase Ω^{+} or Ω^{-} will be active. A mixture state cannot occur, if energy minimization is the overriding principle. Clearly, by neglecting the mixture energy, the rank-one convexification method is obtained. It represents a lower bound of the energy, i.e.,

$$\inf_{\xi} \Psi_{\mathrm{C}} \leq \Psi. \tag{6.8}$$

Remark 10 *In the present subsection, the concept of rank-one convexification has been briefly discussed. Although only the Helmholtz energy has been considered, the same concept can also be applied to the dissipation or to the incrementally defined potential associated with variational constitutive updates, cf. Subsection 4.3. For the sake of understandability, dissipative effects have been excluded here. However, the final model combining deformation-induced twinning and dislocation slip will show such features.*

6.1.3 Effect of mixture energy on phase transition

The mixture energy Ψ^{mix} in Eq. (6.6) governs implicitly the phase transition induced by deformation-induced twinning. By using a simple prototype model, this effect is analyzed here. For the sake of simplicity, it is assumed that the initial and the twinning phase are dislocation-free and further dissipative processes are also excluded (fully reversible model). The more general case, including dissipation of energy will be discussed later. With these assumptions and adopting a St. Venant material model, the Helmholtz energy of the initial phase is given by

$$\Psi^{+}(\boldsymbol{E}^{+}) = \frac{1}{2}\boldsymbol{E}^{+} : \mathbb{K}^{+} : \boldsymbol{E}^{+} \tag{6.9}$$

where $\boldsymbol{E}^{+} = \frac{1}{2}(\boldsymbol{F}^{+\mathrm{T}} \cdot \boldsymbol{F}^{+} - \boldsymbol{I})$ is the Green-Lagrange strain tensor and $\mathbb{K}^{+}$ denotes the fourth-order elastic stiffness tensor. It is supposed that the material shows twinning at the system determined by $\{\boldsymbol{a} := \{01\bar{1}1\}, \boldsymbol{n} := \{0\bar{1}12\}\}$. Accordingly, the twinning shear strain $\boldsymbol{E}_{\mathrm{Twin}}$ which defines the stress free state of the twinning phase is obtained by

$$\boldsymbol{E}_{\mathrm{Twin}} = \frac{1}{2}(\boldsymbol{F}_{\mathrm{Twin}}^{\mathrm{T}} \cdot \boldsymbol{F}_{\mathrm{Twin}} - \boldsymbol{I}) \tag{6.10}$$

with

$$\boldsymbol{F}_{\mathrm{Twin}} = \boldsymbol{I} + \lambda_{\mathrm{Twin}}(\boldsymbol{a} \otimes \boldsymbol{n}). \tag{6.11}$$

Since the material properties of both phases are similar, the elastic strain energy of the twinning phase can be derived from that of the initial phase simply by translating the stress-free state. More explicitly, the energy of the new phase reads

$$\Psi^{-}(\boldsymbol{E}^{-}) = \frac{1}{2}(\boldsymbol{E}^{-} - \boldsymbol{E}_{\mathrm{Twin}}) : \mathbb{K}^{-} : (\boldsymbol{E}^{-} - \boldsymbol{E}_{\mathrm{Twin}}) + \alpha. \tag{6.12}$$

Here, the scalar-valued parameter α corresponds to the thermal activation energy of twinning which is taken as a constant. Following the previous subsection, the total energy obtained by volume averaging is thus given by

$$\Psi = (1 - \xi)\Psi^{+}(\boldsymbol{E}^{+}) + \xi\, \Psi^{-}(\boldsymbol{E}^{-}) + \Psi^{\mathrm{mix}}(\xi). \tag{6.13}$$

Consequently, by considering the Hadamard-type compatibility condition Eq. (6.3) and taking into account that the vectors $\boldsymbol{a}$, $\boldsymbol{n}$ as well as the shear strain λ_{Twin} are a priori known from crystallographic information, the energy Ψ depends only on the macroscopic deformation gradient as well as on the unknown volume fraction ξ, i.e.,

$$\Psi = \Psi(\boldsymbol{F}, \xi). \tag{6.14}$$

Function label	a	b	c	f
Boxcar	0.99	0.01	1000	1
Gauss_A	0.70	0.30	15	1
Gauss_B	0.60	0.40	10	1
Coh	0.45	0.55	1000	1

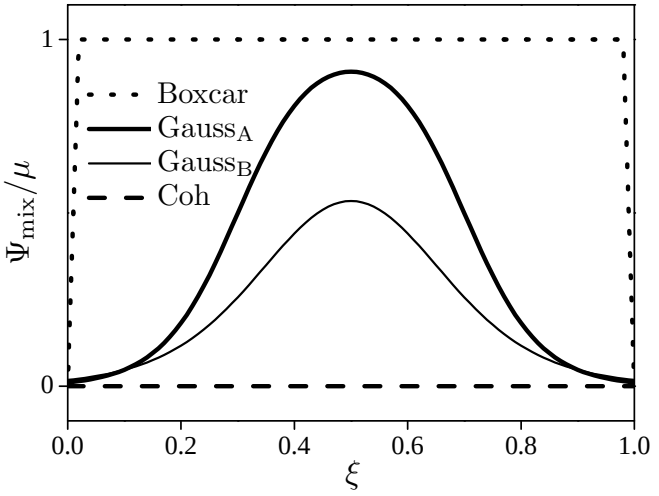

Figure 6.2: Mixture energies (6.15) as a function of the twinning volume fraction ξ

Despite the fact that several parameters such as the laminate morphology, chemical composition, temperature and dislocation structures have deterministic effects on the mixture energy Ψ^{mix}, a simplified model of the type

$$\Psi^{\text{mix}}(\xi) = \frac{f\mu}{(1+\exp[c(\xi-a)])(1+\exp[-c(\xi-b)])}, \tag{6.15}$$

solely depending on the current twinning volume fraction ξ is adopted. In Eq. (6.15), μ is the elastic shear modulus and $\{a, b, c, f\}$ is a set of adjustable scalar shape function parameters defining the mixture energy Ψ^{mix}, see Fig. 6.2. In case of a fully coherent interface not showing any residual stresses, the mixture energy "Coh" is set to zero. The other limiting case is the Boxcar-type function. It describes a highly incoherent interface. Depending on the shear modulus, this function is a good approximation of the classical Taylor-type homogenization. More precisely, if energy minimization is the overriding principle and μ is large enough, phase mixture cannot occur.

The prototype model discussed before is subjected to a shear strain

$$\boldsymbol{F} = \boldsymbol{I} + \varepsilon(\boldsymbol{a} \otimes \boldsymbol{n}) \tag{6.16}$$

parallel to the twinning plane. Here, ε denotes the loading amplitude. Subsequently, the stable state of the system is obtained by minimizing the total

energy, i.e.,

$$\inf_{\xi} \Psi(\varepsilon, \xi). \tag{6.17}$$

The resulting energies are summarized in Fig. 6.3 (top). There, the thin lines correspond to the energies of the single phases. The evolution of the computed volume ratio ξ is shown in Fig. 6.3 (bottom). As expected, the interface energy strongly governs the phase transition. In the case of a coherent interface, the total energy is identical to the rank-one convex hull which results in a linear evolution of the twinning volume fraction. By way of contrast, the Boxcar mixture energy leads to a Taylor-type phase transition. The Gaussian mixture energies range between the aforementioned limiting cases.

Certainly, although the energy governs phase transition within the presented model, this physical quantity cannot be measured in experiments. For this reason, the stress response is analyzed as well. Fig. 6.4 summarizes the respective diagrams. Since the considered deformations are comparably small, the stress-strain diagrams are piecewise linear.

In case of coherent phases (Fig. 6.4(f)), a classical stress plateau can be seen, i.e., the stress increases linearly except for within the transition range $\xi \in (0, 1)$. By way of contrast, for the other limiting case, being the Boxcar-type mixture energy, a Taylor transition is observed. More precisely, the stress-strain diagram is discontinuous and shows a jump at the transition point. Experimental evidence of such a behavior can be found, e.g., in Salje et al. (2009); Harrison et al. (2004). However, considering sufficiently large samples of single crystal magnesium, a continuous stress-strain response is expected. Hence, the Taylor-type model, although computationally very efficient cannot be utilized. The opposite is true for the coherent case being identical to a rank-one convexification: It leads to physically sound results, but it is numerically very expensive. For this reason, an approximation combining the advantages of these limiting cases will be elaborated in the next subsection.

6.2 Approximation of the solid-solid phase transition induced by twinning

Although the modeling of a solid-solid phase transition by means of the concept of rank-one convexification is physically sound, its application to complex systems showing dislocation slip and deformation-induced twinning is numerically very expensive (in case of magnesium, the interplay between twelve dislocation systems and six different twinning modes has to be considered). More precisely, the respective computational costs corresponding to the numerical analysis of a polycrystal would be prohibitive. Therefore, an approximation of

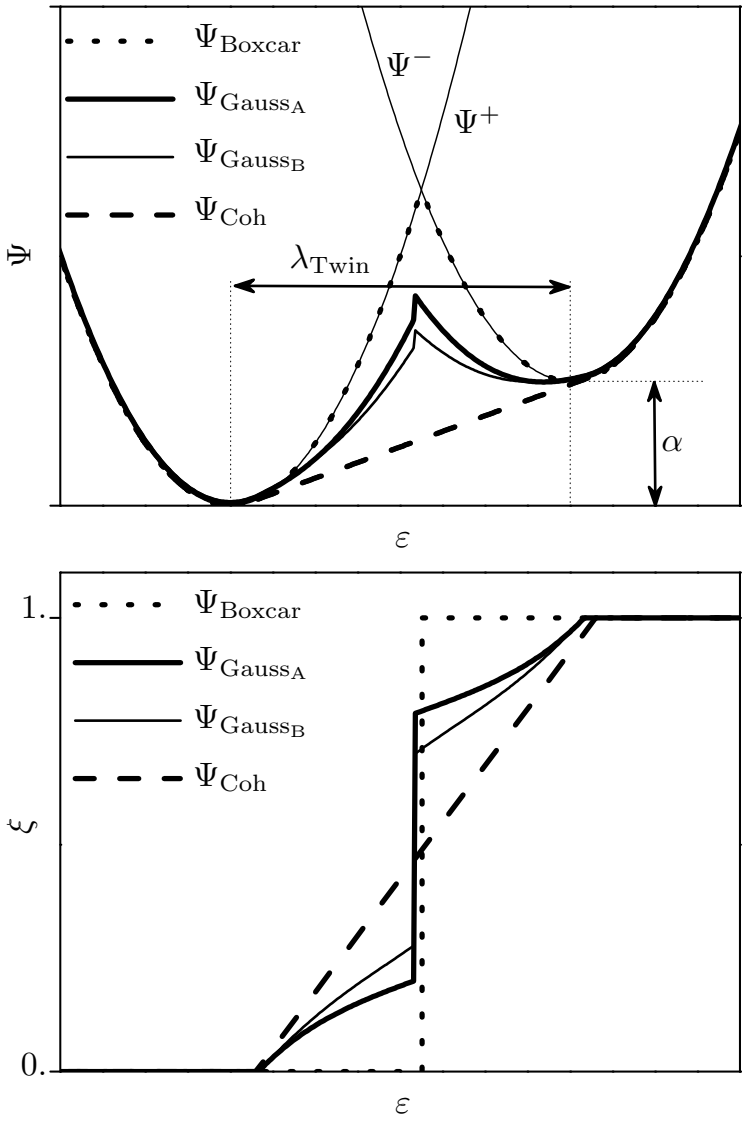

Figure 6.3: Top: elastic strain energy of the initial and twinning phase and the resulting homogenized energy using the mixture energies illustrated in Fig.(6.2); Bottom: evolution of the twinning volume fraction ξ depending on the considered mixture energy

the rank-one convexification method which is significantly more efficient will be elaborated here.

6.2.1 Fundamentals

The underlying idea of the proposed model suitable for the analysis of solid-solid phase transition originates from experimental observations (Barber & Wenk, 1979; Terlinde & Luetjering, 1982; Chia et al., 2005; Li & Ma, 2009). According to the cited works, experiments show that the width of a twin laminate has to be large enough to allow for dislocation slip inside this laminate. Consequently, observable plastic deformations within the twin require a sufficient twin volume. This phenomenon is strongly pronounced, particularly, in the case of magnesium with a very low twinning activation energy.

The aforementioned experimental observations suggest to decompose twinning into two stages. Within the first of those, the twin laminate is comparably small and hence, plastic deformations within the reoriented phase can be neglected. If the twin volume reaches a critical threshold, the slip systems corresponding to the reoriented crystal lattice may become active. For modeling the first stage, the concept of *pseudo-dislocation* is utilized, cf. Chin (1975). Hence, instead of computing the twin volume explicitly, the shear strain caused by twinning is considered. If this shear strain equals the twinning strain (unconstrained twinning), the crystal lattice is reoriented. For the sake of computationally efficiency, the reorientation is applied to the whole underlying representative volume. Consequently, the deformation systems associated with the original crystal lattice may be active in the first stage, while only the systems related to the reoriented crystal are considered in the second stage.

Accounting for standard dislocation slip ($\varsigma^{(a)}$) as well as for the aforementioned pseudo-dislocation-related slip ($\varsigma_{\mathrm{pd}}^{(j)}$) caused by twinning within the first transformation stage, yields a plastic velocity gradient of the type

$$\boldsymbol{l}^{\mathrm{p}} = \sum_{a=1}^{n} \varsigma^{(a)} \operatorname{sign}[\boldsymbol{\Sigma} : \boldsymbol{N}^{(a)}] \, \boldsymbol{N}^{(a)} + \sum_{j=1}^{m} \varsigma_{\mathrm{pd}}^{(j)} \operatorname{sign}[\boldsymbol{\Sigma} : \boldsymbol{N}_{\mathrm{pd}}^{(j)}] \, \boldsymbol{N}_{\mathrm{pd}}^{(j)} \tag{6.18}$$

with

$$\boldsymbol{N}_{\mathrm{pd}}^{(j)} = \boldsymbol{a}^{(j)} \otimes \boldsymbol{n}^{(j)}. \tag{6.19}$$

Accordingly, the slip caused by pseudo-dislocations is assumed to be governed by a standard Schmid-type law. Further extending this analogy, the Helmholtz energy describing the initial (not twinned) phase is chosen as

$$\Psi^{+}(\boldsymbol{C}^{\mathrm{e}}, \boldsymbol{\lambda}, \boldsymbol{\lambda}_{\mathrm{pd}}) = \Psi^{\mathrm{e}}(\boldsymbol{C}^{\mathrm{e}}) + \Psi^{\mathrm{p}}(\boldsymbol{\lambda}) + \Psi_{\mathrm{pd}}^{\mathrm{p}}(\boldsymbol{\lambda}_{\mathrm{pd}}). \tag{6.20}$$

Here, $\lambda_{\mathrm{pd}}^{(i)}$ are internal variables associated with the pseudo-dislocation ($\dot{\lambda}_{\mathrm{pd}}^{(i)} = \varsigma_{\mathrm{pd}}^{(i)}$). Once the critical twinning strain is reached, the energy of the reoriented phase is active. Since the original and the twinned domain show the same mechanical properties (except for the orientation of the crystal lattice), the Helmholtz energy of the reoriented phase reads

$$\Psi^{-}(\boldsymbol{C}^{\mathrm{e}}, \boldsymbol{\lambda}) = \Psi^{\mathrm{e}}(\boldsymbol{C}^{\mathrm{e}}) + \Psi^{\mathrm{p}}(\boldsymbol{\lambda}). \tag{6.21}$$

Having defined the Helmholtz energies of the different phases, the total energy can be computed in a standard manner. In line with the previous subsections, it is given by

$$\begin{aligned} \Psi(\boldsymbol{C}^{\mathrm{e}}, \boldsymbol{\lambda}, \boldsymbol{\lambda}_{\mathrm{pd}}, \boldsymbol{\lambda}^{-}, \xi) = (1-\xi)\Psi^{+}(\boldsymbol{C}^{\mathrm{e}}, \boldsymbol{\lambda}, \boldsymbol{\lambda}_{\mathrm{pd}}) \\ + \xi\ \Psi^{-}(\boldsymbol{C}^{-\mathrm{e}}, \boldsymbol{\lambda}^{-}) + \Psi^{\mathrm{mix}}(\xi),\ \forall \xi \in \{0;1\}. \end{aligned} \tag{6.22}$$

Although Eq. (6.22) looks formally identical to Eq. (6.6), both models are significantly different. While a continuous evolution for ξ is considered within the framework provided by the rank-one convexification, the novel approximation is based on a discontinuous transition, i.e., $\xi \in \{0;1\}$. Clearly, the mixture energy can thus be neglected and consequently, a minimization of Eq. (6.22) w.r.t. ξ simplifies to

$$\inf_{\xi \in \{0;1\}} \Psi(\boldsymbol{C}^{\mathrm{e}}, \boldsymbol{\lambda}, \boldsymbol{\lambda}_{\mathrm{pd}}, \boldsymbol{\lambda}^{-}, \xi) = \min[\ \Psi^{+}(\boldsymbol{C}^{\mathrm{e}}, \boldsymbol{\lambda}, \boldsymbol{\lambda}_{\mathrm{pd}}),\ \Psi^{-}(\boldsymbol{C}^{-\mathrm{e}}, \boldsymbol{\lambda}^{-})]. \tag{6.23}$$

Remark 11 *During the first stage in which twinning is described by the concept of pseudo-dislocation, the elastic energy of the reoriented phase has been neglected. Such an approximation is admissible, since the elastic deformations are comparably small in magnesium. However, the more general case is also included in the framework as discussed here.*

Remark 12 *As mentioned before, it is completely unknown for complex loading conditions, whether the twinned domain inherits the dislocations corresponding to the initial phase, or if only a certain part of them is transferred. Therefore and focusing on the model presented here, it is not clear which initial conditions are to be chosen for $\boldsymbol{\lambda}^{-}$. Within the present thesis, the final values of $\boldsymbol{\lambda}$ serve as initializers of $\boldsymbol{\lambda}^{-}$. Hence, it is assumed that the whole dislocation history is kept.*

Remark 13 *Within the presented model, phase transition occurs, if the slip caused by pseudo-dislocations reaches a certain threshold. In this respect, the transformation is strain-based. However, by choosing $\Psi_{\mathrm{pd}}^{\mathrm{p}}(\boldsymbol{\lambda}_{\mathrm{pd}})$ properly, an equivalent energy depending criterion can be derived. Such a criterion will be elaborated for the final model.*

Remark 14 *Although only the Helmholtz energy has been considered within the present subsection, the discussed ideas can also be applied to the dissipation and the stress power. Accordingly, the final model will capture dissipative effects as well.*

6.2.2 Illustrative examples

In this subsection, the characteristics of the novel phase transition model as discussed in the previous subsection are illustrated. It will be shown that this model combines the advantages of a classical Taylor-type approximation and the computationally more expensive concept of rank-one convexification. More precisely, the continuous stress-strain response as predicted by the model is in line with that of the rank-one convexification, while it is as efficient as the Taylor-type model. First, a fully reversible prototype is considered. Subsequently, dissipative effects are considered as well.

6.2.2.1 Prototype model

The mechanical prototype model analyzed here is in line with that previously discussed in Subsection 6.1.3. The sole difference is that pseudo-dislocation slip caused by twinning is already considered within the initial phase. Accordingly, the plastic deformations in the initial phase are described by

$$\boldsymbol{F}^{+\mathrm{p}} = \boldsymbol{I} + \lambda_{\mathrm{pd}}(\boldsymbol{a} \otimes \boldsymbol{n}) \tag{6.24}$$

with λ_{pd} being the magnitude of the PD's plastic shear. With Eq. (6.24) and assuming the St. Venant model, the stored energy of the initial phase is given by

$$\Psi^{+}(\boldsymbol{E}^{+}, \lambda_{\mathrm{pd}}) = \frac{1}{2}(\boldsymbol{E}^{+} - \boldsymbol{E}^{+\mathrm{p}}) : \mathbb{K}^{+} : (\boldsymbol{E}^{+} - \boldsymbol{E}^{+\mathrm{p}}) + \Psi^{\mathrm{p}}_{\mathrm{pd}}(\lambda_{\mathrm{pd}}) \tag{6.25}$$

with $\boldsymbol{E}^{+} = 1/2(\boldsymbol{F}^{+T} \cdot \boldsymbol{F}^{+} - \boldsymbol{1})$ and $\boldsymbol{E}^{+\mathrm{p}} = 1/2(\boldsymbol{F}^{+\mathrm{p}T} \cdot \boldsymbol{F}^{+\mathrm{p}} - \boldsymbol{1})$ being the total Green-Lagrange strain tensor and its plastic part. The model is completed by assuming a suitable energy $\Psi^{\mathrm{p}}_{\mathrm{pd}}(\lambda_{\mathrm{pd}})$. Here, the choice

$$\Psi^{\mathrm{p}}_{\mathrm{pd}}(\lambda_{\mathrm{pd}}) = \beta\, \lambda_{\mathrm{pd}} + \Pi(\lambda_{\mathrm{pd}}) \tag{6.26}$$

is made. In Eq. (6.26), $\Pi(\lambda_{\mathrm{pd}})$ can be understood as a penalty function guaranteeing that the plastic shear of PD-twinning is properly bounded, i.e., $\lambda_{\mathrm{pd}} \in [0, \lambda_{\mathrm{Twin}}]$. This can be realized by defining

$$\Pi(\lambda_{\mathrm{pd}}) := \begin{cases} 0 & \text{if } \lambda_{\mathrm{pd}} \in [0, \lambda_{\mathrm{Twin}}) \\ \infty & \text{if } \lambda_{\mathrm{pd}} \geq \lambda_{\mathrm{Twin}} \end{cases} \tag{6.27}$$

Consequently, if energy minimization is the overriding principle, the second phase is energetically more favorable, if the PD-twinning strain λ_{pd} approaches the threshold λ_{Twin}. In this respect, $\Pi(\lambda_{\mathrm{pd}})$ defines an energy-based transformation condition.

Having discussed the second term in Eq. (6.26), the linear summand $\beta\ \lambda_{\mathrm{pd}}$ remains to be explained. Although the Helmholtz energy is addressed here, this terms looks formally identical to the dissipation (product of plastic multiplier and the yield strength). According to Eq. (6.27), $\Psi^{\mathrm{P}}_{\mathrm{pd}}(\lambda_{\mathrm{pd}}) = \beta\ \lambda_{\mathrm{pd}}$ for $\lambda_{\mathrm{pd}} \in [0, \lambda_{\mathrm{Twin}})$. Consequently, no additional hardening is active within the first stage. As a result, the Helmholtz energy can be decomposed in this case into a standard elastic part and a dissipation-like term. Hence, the predicted mechanical response is expected to be similar to that of perfect plasticity, i.e., the model will show a stress plateau within the interval $\lambda_{\mathrm{pd}} \in [0, \lambda_{\mathrm{Twin}})$.

6.2.2.2 Non-dissipative process

In this section, a fully reversible process is analyzed. More precisely, the model introduced within the previous section is utilized. The only difference compared to the model employed in Subsection 6.1.3 is that the PD-twinning system is included within the initial phase and a Boxcar mixture energy is considered for enforcing a Taylor-type approximation, see Fig. 6.2. Hence, and in line with Eq. (6.17), the minimization problem to be solved reads

$$\inf_{\lambda_{\mathrm{pd}},\xi} \Psi(\varepsilon, \lambda_{\mathrm{pd}}, \xi). \tag{6.28}$$

As evident, the slip caused by PD-twinning represents an additional unknown variable within optimization problem (6.28). Fig. 6.4(j) shows the minimizer of the total energy in terms of the prescribed strain amplitude. Accordingly, although the transition of the volume fraction ξ is approximated in a discontinuous fashion (see Fig. 6.4(k)), the resulting energy evolution is continuous. Consequently, PD-twinning leads to a smoothing of the energy and thus, to a continuous stress-strain diagram (see Fig. 6.4(l)). More precisely, the stress-strain diagram is piecewise linear (comparably small deformations) and shows a plateau. This is a direct consequence of the term $\beta\ \lambda_{\mathrm{pd}}$ included within Ψ^{P}.

A more careful comparison reveals that the energy response as well as that of the stresses predicted by the advocated model are in excellent agreement with those corresponding to the computationally more expensive rank-one convexification method (cf. Fig. 6.4(d) and Fig. 6.4(f)). However, the evolution of the volume fraction ξ is discontinuous as seen for the Taylor-type approximation (see Fig. 6.4(h)). As a result, the presented model combines indeed the advantages of the aforementioned limiting cases.

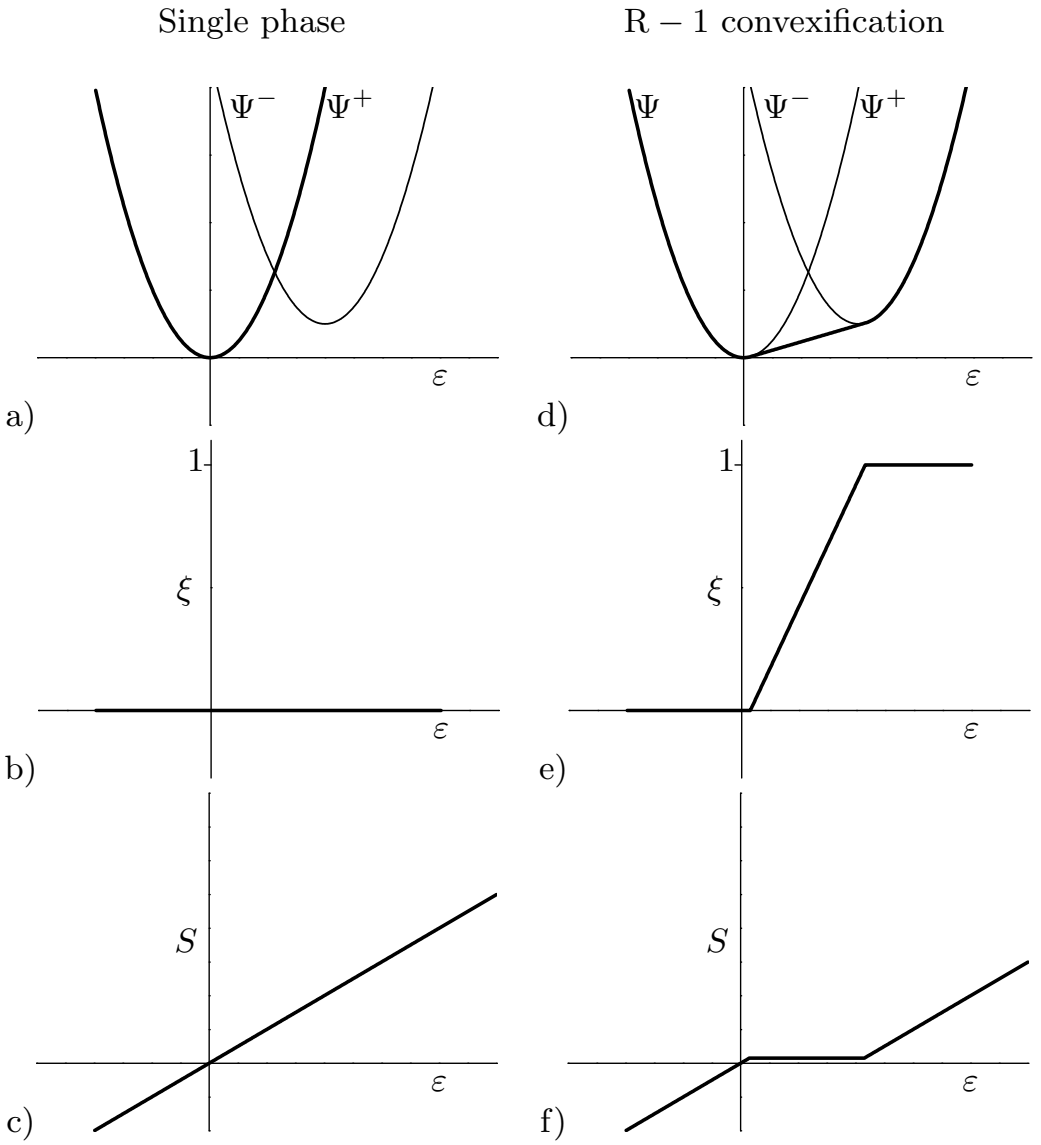

Figure 6.4: Fully reversible prototype model: Illustration of different phase transition models: energy evolution (top row); evolution of the twinning volume fraction (middle row); resulting stress-strain response (bottom row). Thick lines show the resulting minimum energy, while thin lines are associated with the single phases.

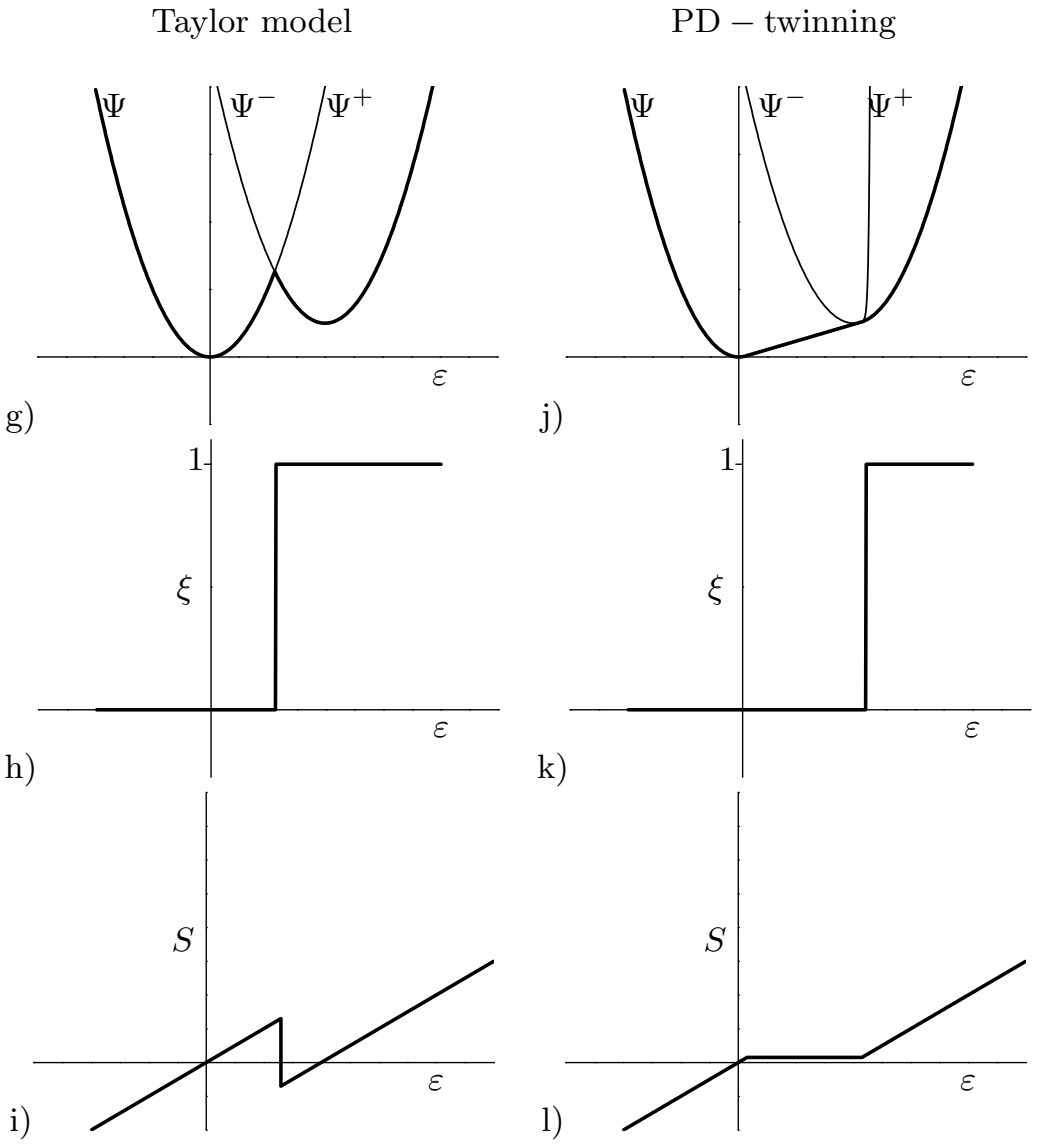

Figure 6.4: Continue

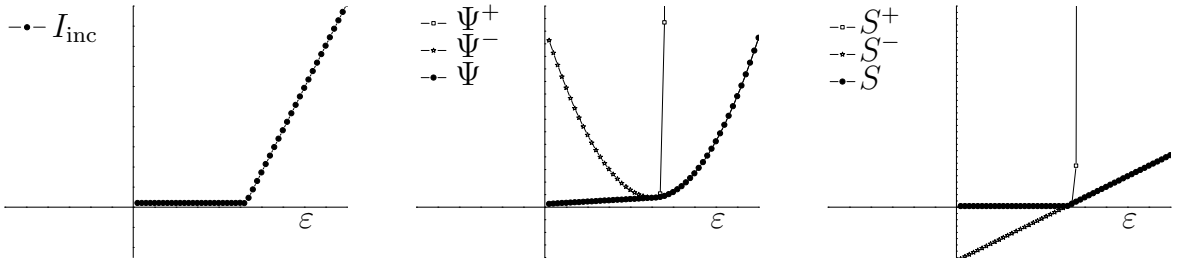

a) b) c)

Figure 6.5: Prototype model including dissipation: a) incremental minimizers of I_{inc} (see Eq. (6.30)), b) stored energy corresponding to each phase, c) stress-strain diagram

6.2.2.3 Dissipative process

Although the example discussed in the previous subsection illustrated the characteristics of the proposed phase transition model, deformation-induced twinning cannot be considered as fully reversible. Hence, dissipative mechanisms are additionally considered. Consequently, the Helmholtz energy in Eq. (6.28) is replaced by the incrementally defined integrated stress power, see Section 4.3.1. More explicitly, the integrated stress power of the initial phase and that of the twinned phase are given by

$$\begin{array}{lcll} I^+(\varepsilon, \Delta\lambda_{\text{pd}}) & = & \Psi^+|_{n+1}(\varepsilon, \Delta\lambda_{\text{pd}}) - \Psi^+|_n + A\ \Delta\lambda_{\text{pd}} \\ I^-(\varepsilon) & = & \Psi^-|_{n+1}(\varepsilon) & -\Psi^-|_n. \end{array} \tag{6.29}$$

Here, $A\ \Delta\lambda_{\text{pd}} = \Delta\mathcal{D}$ is the dissipation integrated over the time interval $[t_n; t_{n+1}]$ and A is an additional material parameter governing the dissipation amplitude. With Eqs. (6.29), the resulting energy is computed from the (discrete) minimization problem

$$I_{\text{inc}}(\varepsilon) = \min\{\inf_{\Delta\lambda_{\text{pd}}} I^+; I^-\}. \tag{6.30}$$

Fig. 6.5a shows the evolution of I_{inc} as a function of the applied strain ε. During the first stage, PD-twinning is active resulting in a vanishing energy I_{inc}. When the threshold value λ_{Twin} is reached, the phase showing the new orientation becomes energetically more favorable yielding an increasing energy. The same holds for the Helmholtz energy. The computed stress-strain response is depicted in Fig. 6.5c. Accordingly, the stress diagram shows a plateau until the threshold value λ_{Twin} is reached and the crystal is reoriented. Subsequently, the stresses increase linearly (small deformations). In summary, the mechanical response predicted by the novel model is again in excellent agreement with that of the computationally more expensive rank-one convexification method.

6.3 Numerical implementation - variational constitutive update

In this section, the numerical implementation of the proposed model suitable for the analysis of deformation-induced twinning coupled to plastic slip is summarized. Its calibration, together with the choice of admissible hardening evolution laws, will be described in Chapter 7. First, the Helmholtz energies $\Psi = \Psi^{\mathrm{e}} + \Psi^{\mathrm{p}}$ describing the initial phase and the reoriented phase are explained. Subsequently, the dissipation functionals are introduced. This section is completed by the numerical implementation.

The elastic response of magnesium within the initial and the reoriented phase is approximated by means of a neo-Hookean model (Eq. (4.9)). Since the macroscopic anisotropy is not pronounced, an isotropic model such as that defined by Eq. (4.9) represents a suitable choice. Furthermore, the elastic deformations in magnesium are comparatively small and consequently, the elastic material model does not influence the results significantly.

The opposite is true for the plastic deformations. Taking 12 slip systems and 6 PD-twinning systems into account, the part of the Helmholtz energy associated with plastic work is assumed as

$$\Psi^{\mathrm{p}} = \Psi^{\mathrm{p}}_{\mathrm{self}} + \Psi^{\mathrm{p}}_{\mathrm{lat}} + \Psi^{\mathrm{p}}_{\mathrm{pd}}. \tag{6.31}$$

Here, $\Psi^{\mathrm{p}}_{\mathrm{self}}$ and $\Psi^{\mathrm{p}}_{\mathrm{lat}}$ describe latent and self hardening of the slip systems, while $\Psi^{\mathrm{p}}_{\mathrm{pd}}$ is related to PD-twinning. This decomposition, together with the classical Schmid-type yield functions (4.20), results in the dissipation term

$$\mathcal{D} = \sum_{i=1}^{12} \Sigma_0^{(a)}\, \varsigma^{(a)} + \sum_{i=1}^{6} \Sigma^{(a)}_{\mathrm{pd}\,0}\, \varsigma^{(a)}_{\mathrm{pd}} \geq 0. \tag{6.32}$$

Again, the first part governs the standard slip systems, while the second part is associated with PD-twinning. Integration of the stress power ($\mathcal{P} = \dot{\Psi} + \mathcal{D}$) yields finally the incrementally defined functional

$$I^{(\alpha)}_{\mathrm{inc}} = \Psi|_{n+1} - \Psi|_n + \sum_{i=1}^{12} \Sigma_0^{(a)}\, \Delta\varsigma^{(a)} + \sum_{i=1}^{6} \Sigma^{(a)}_{\mathrm{pd}\,0}\, \Delta\varsigma^{(a)}_{\mathrm{pd}}. \tag{6.33}$$

Here, $\alpha \in \{\mathrm{ini}; \mathrm{Tw}\}$. Hence, the same incremental energy is used for the initial as well as for the reoriented phase. However, the crystal lattice orientation of both phases and the internal variables are, of course, not necessarily identical. For computing energy (7.5), the underlying evolution equations are again integrated by the implicit scheme (4.32). Finally, the stress power of the crystal can be determined from the discrete minimization

$$I_{\mathrm{inc}} = \min\{\inf I^{\mathrm{ini}}_{\mathrm{inc}}; \inf {I_{\mathrm{inc}}}^{-}\}. \tag{6.34}$$

In this connection, the optimization problems $\inf I_{\mathrm{inc}}^{(\alpha)}$ depending on $\Delta\varsigma^{(a)}$ and $\Delta\varsigma_{\mathrm{pd}}^{(a)}$ have to be solved for a given strain. Based on Eq. (6.34), the first Piola-Kirchhoff stress tensor $\boldsymbol{P}$ can be computed in a standard manner, i.e., $\boldsymbol{P} = \partial_{\boldsymbol{F}} I_{\mathrm{inc}}$.

7 Calibration of the variational model

The application of numerical models requires the calibration of the corresponding material parameters. In principle, they can be determined by a standard optimization procedure in which the error between the experimentally observed response and the prediction by the model is minimized. However, since the number of material parameters is large (12 slip systems, 6 PD-twinning systems, latent hardening, etc.), it is more promising to separate the different deformation modes. One possible experimental setup for achieving this is provided by the channel die test, cf. Kelley & Hosford (1968).

7.1 Experimental measurements

Tab. 7.1 summarizes the reported experimentally measured values of critical resolved shear stresses. It can be inferred from Tab. 7.1 and also from the yield points in Fig. 2.12 that the active deformation systems (basal and tensile twinning) are not coplanar. This implies that during an ideally arranged channel die test, punching the sample does not stimulate two highly active deformation systems simultaneously. Moreover, tensile twinning has a polar characteristic and is active only at tensile loading along the c-axis. Since the resolved shear stresses on basal and prismatic deformation systems are zero for sample A (Fig. 2.13), the only active deformation system is pyramidal. However, Kelley and Hosford (Kelley & Hosford (1968)) observed traces of the basal dislocation system and related it to an imperfection of the sample which is generated during preparation. By the same analogy, deformation in sample C reduces to prismatic slip, E to the tensile twinning (as well as post twinning pyramidal) and G to the basal slip system.

7.2 Identification of the material parameters

In this section, the channel die test is formulated as an initial boundary value problem based on which the material parameters of the proposed variational model are identified by a standard least squares method.

Table 7.1: Reported critical resolved shear stresses for the deformation systems of magnesium single crystal at room temperature.

	Basal [MPa]	Prismatic [MPa]	Pyramidal [MPa]	Twinning [MPa]
Burke (1952)	0.45			
Kelley & Hosford (1968)	0.48			
Reed-Hill & Robertson (1957a)				2
Obara et al. (1973)			30-50	
Reed-Hill & Robertson (1957b)		39.3		

7.2.1 Boundary condition

In order to simulate the channel die test, an approximated deformation of the type

$$\boldsymbol{F} = \boldsymbol{I} - \varepsilon(\boldsymbol{e}_3 \otimes \boldsymbol{e}_3) + \tilde{\varepsilon}(\boldsymbol{e}_1 \otimes \boldsymbol{e}_1), \tag{7.1}$$

is considered where ε and $\tilde{\varepsilon}$ characterize the compression and extension strain in the punching direction ($\boldsymbol{e}_3$) and the channel direction ($\boldsymbol{e}_1$).

7.2.2 Elasticity model

The elastic response of magnesium within the initial and the reoriented phase is approximated by means of a neo-Hooke model of the type

$$\Psi^{\mathrm{e}}(\boldsymbol{C}^{\mathrm{e}}) = \frac{\lambda_{\mathrm{E}}}{2}(\ln(J^{\mathrm{e}}))^2 - \mu \ln(J^{\mathrm{e}}) + \frac{\mu}{2}(\mathrm{tr}(\boldsymbol{C}^{\mathbf{e}}) - 3), \tag{7.2}$$

where J^{e} is the determinant of the elastic deformation gradient and $\{\lambda_{\mathrm{E}}, \mu\}$ are the Lamé constants. Since the macroscopic anisotropy is not pronounced, an isotropic model such as that defined by Eq. (7.2) represents a suitable choice. Furthermore, the elastic deformation in magnesium is comparatively small and hence, elastic material model does not influence the results significantly.

7.2.3 Plasticity model

The variational crystal plasticity model (Section 4.3) is taken into account. The part of the Helmholtz energy associated with plastic work is assumed as

$$\Psi^{\mathrm{p}} = \Psi^{\mathrm{p}}_{\mathrm{self}} + \Psi^{\mathrm{p}}_{\mathrm{lat}} + \Psi^{\mathrm{p}}_{\mathrm{pd}}. \tag{7.3}$$

Here, $\Psi^{\mathrm{p}}_{\mathrm{self}}$ and $\Psi^{\mathrm{p}}_{\mathrm{lat}}$ describe latent and self hardening of the slip systems, while $\Psi^{\mathrm{p}}_{\mathrm{pd}}$ is related to PD-twinning. This decomposition, together with the classical Schmid-type yield functions (4.20), results in the dissipation

$$\mathcal{D} = \sum_{i=1}^{12} \Sigma_0^{(a)}\, \varsigma^{(a)} + \sum_{i=1}^{6} \Sigma^{(a)}_{\mathrm{pd}\,0}\, \varsigma^{(a)}_{\mathrm{pd}} \geq 0. \tag{7.4}$$

Here, the first part governs the standard slip systems, while the second part is associated with PD-twinning. Integration of the stress power ($\mathcal{P} = \dot{\Psi} + \mathcal{D}$) yields finally the incrementally defined functional

$$I_{\mathrm{inc}} = \Psi|_{n+1} - \Psi|_n + \sum_{i=1}^{12} \Sigma_0^{(a)}\, \Delta\varsigma^{(a)} + \sum_{i=1}^{6} \Sigma^{(a)}_{\mathrm{pd}\,0}\, \Delta\varsigma^{(a)}_{\mathrm{pd}}. \tag{7.5}$$

Hence, the same incremental energy is used for the initial as well as for the reoriented phase. However, the crystal lattice orientation of both phases and the internal variables are, of course, not necessarily identical. For computing energy (7.5), the underlying evolution equations are again integrated by the implicit scheme (4.32). Finally, the stress power of the crystal can be determined from the discrete minimization

$$I_{\mathrm{inc}} = \min\{\inf I^{+}_{\mathrm{inc}}; \inf I^{-}_{\mathrm{inc}}\}. \tag{7.6}$$

In this connection, the optimization problems $\inf I^{(\alpha)}_{\mathrm{inc}}$ depending on $\Delta\varsigma^{(a)}$ and $\Delta\varsigma^{(a)}_{\mathrm{pd}}$ have to be solved for a given strain. Based on Eq. (7.6), the first Piola-Kirchhoff stress tensor $\boldsymbol{P}$ can be computed in standard manner, i.e., $\boldsymbol{P} = \partial_{\boldsymbol{F}} I_{\mathrm{inc}}$.

7.2.3.1 Sets of deformation systems

The crystal symmetry and the constrained loading conditions reduce the number of potentially active slip systems in each sample. More precisely, the following deformation modes are assumed to be active:

- Sample A: pyramidal slip systems $\{[2\bar{1}\bar{1}\bar{3}](2\bar{1}\bar{1}2)\ ,\ [2\bar{1}\bar{1}3](\bar{2}112)\}$
- Sample C: prismatic slip systems $\{[1\bar{2}10](10\bar{1}0)\ ,\ [11\bar{2}0](1\bar{1}00)\}$
- Sample E:
  - Initial phase: PD-twinning $\{[01\bar{1}1](0\bar{1}12)\ ,\ [0\bar{1}11](01\bar{1}2)\}$
  - Twinning phase: pyramidal slip systems $\{[11\bar{2}\bar{3}](11\bar{2}2)\ ,\ [\bar{1}\bar{2}\bar{1}\bar{3}](\bar{1}\bar{2}\bar{1}2)\ ,\ [\bar{1}\bar{1}2\bar{3}](\bar{1}\bar{1}22)\ ,\ [1\bar{2}1\bar{3}](1\bar{2}12)\}$
- Sample G: basal slip systems $[01\bar{1}0](0001)$

Pairs of energetically equivalent slip systems result in a pure stretching plastic deformation for samples A, C and E. By way of contrast, only one deformation system is potentially active in sample G resulting in a lattice rotation. Fig. 7.1 gives an illustration of the geometrical relation between the channel die test and the micromechanical deformation systems of each sample.

7.2.3.2 Hardening models

The results of the channel die experiments (see Kelley & Hosford (1968)) suggest that the mechanical response of prismatic and pyramidal slip systems can be approximated by an exponential hardening law, while only slight hardening effects have been observed for the basal and the PD-twinning systems. Hence, their hardening response is assumed as linear with comparably small moduli. To guarantee a physically sound phase transition, the hardening law corresponding to PD-twinning is superposed by an additional function converging to infinity, if the critical transformation strain λ_{Twin} is reached. In summary, self-hardening is approximated by

$$Q^{(a)}_{\mathrm{self}} = \frac{\partial \Psi^{\mathrm{p}}_{\mathrm{self}}}{\partial \lambda^{(a)}} = \begin{cases} h_0\ \lambda^{(a)} & \text{Basal} \\ \Sigma_\infty(1-\exp(-h_0\lambda^{(a)}/\Sigma_\infty)) & \text{Prismatic and Pyramidal} \\ h_0(\lambda^{(a)} + (\frac{\lambda^{(a)}}{\lambda_{\mathrm{Twin}}})^m) & \mathrm{PD-twinning} \end{cases} \tag{7.7}$$

where h_0, m, Σ_0 and Σ_∞ are material parameters, while $m >> 1$ is a numerical parameter smoothing the discrete phase transition. The resulting hardening functions are depicted in Fig. 7.2. The hardening response is completed by assuming a linear latent hardening model of the type

$$\Psi^{\mathrm{p}}_{\mathrm{lat}} = \frac{1}{2}\ \boldsymbol{\lambda} \cdot \boldsymbol{l} \cdot \boldsymbol{\lambda}. \tag{7.8}$$

Its resulting moduli are constant and given by

$$l^{ab} := \frac{\partial^2 \Psi^{\mathrm{p}}_{\mathrm{lat}}}{\partial \lambda^{(a)} \partial \lambda^{(b)}}. \tag{7.9}$$

By comparing the experimentally observed mechanical response to the respective predictions by the model, the set of material parameters as summarized in Tab. 7.2 was found.

7.2.4 Comparison between experimental observations and predictions by the model

The results as computed by applying the variationally consistent method described in Subsection 6.3, together with the respective experimental observa-

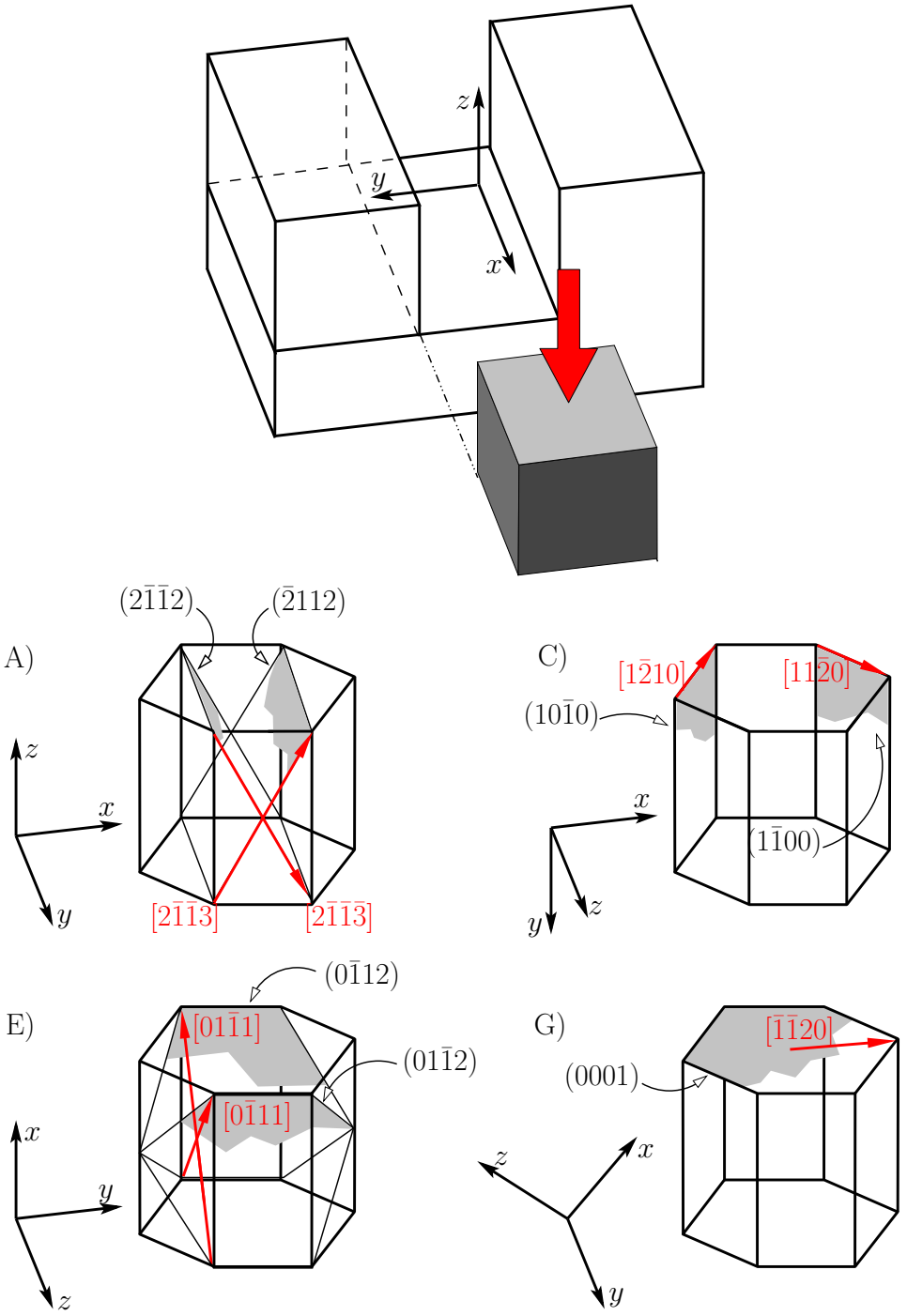

Figure 7.1: Crystallographic representation of active deformation systems in an ideally performed channel die test. Orientations A-G are analogous to those tested by Kelley and Hosford (Kelley & Hosford (1968)). Glide planes of active dislocations in each sample are illustrated by gray color and the directions are shown by red arrows

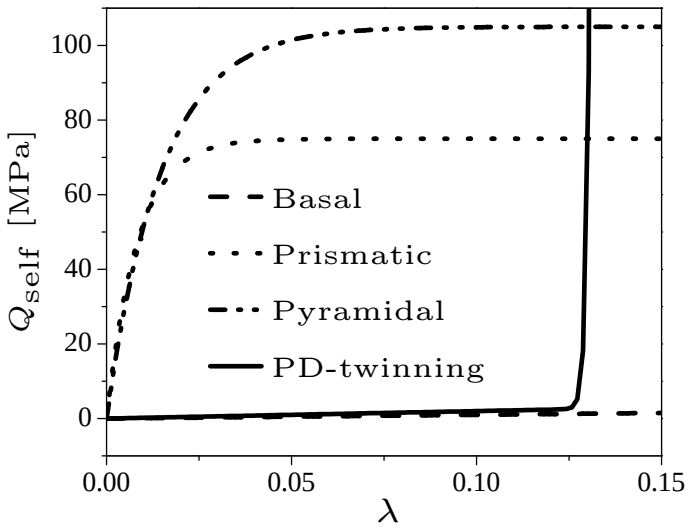

Figure 7.2: Self hardening of the different deformation systems in magnesium

Table 7.2: Material parameters used in the numerical analysis

Elastic Properties	$\lambda = 34$(GPa)			μ =17 (GPa)		
Hardening parameters						
	Σ_0 (MPa)	h_0 (MPa)	Σ_∞ (MPa)	m	λ_{Twin}	l^{ab}
Basal	0.48	10	-	-	-	0
Prismatic	20	9000	75	-	-	20
Pyramidal	25	7100	105	-	-	25
Pseudo-dislocation twinning	1	20	-	150	0.17	10

tions, are shown in Fig. 7.3.

For improving the numerical efficiency of the model, the symmetry conditions associated with the different crystal orientations were also taken into account. According to Fig. 7.3, the computed stress vs. strain response is in good agreement with the experimentally observed results. For the PD-twinning system, two energy wells are plotted: one for the initial phase and one for the reoriented phase. From this figure it can be seen that the energy of the reoriented system becomes energetically more favorable, when the critical twinning transformation strain is reached. The effect of this transition on the stresses is evident in the respective stress vs. strain diagram. While hardening is comparably small during the first loading stage, new slip systems are active within the reoriented phase resulting in more pronounced hardening.

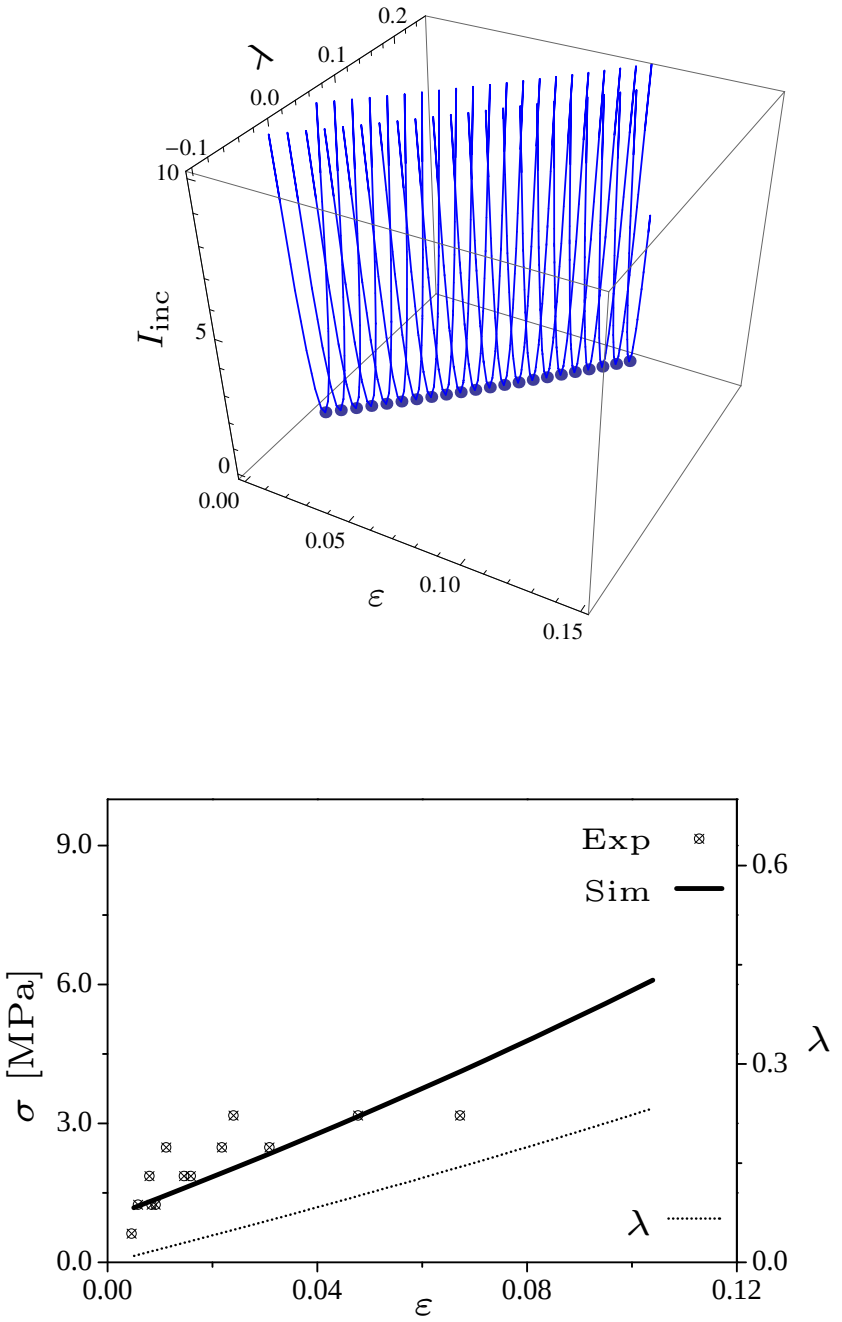

Figure 7.3: Channel die test: Comparison between the experimentally measured results by Kelley & Hosford (1968) (sample G), denoted by "Exp", and the model predictions, denoted by "Sim": evolution of the incrementally defined energy (top); true stresses vs. true strains (bottom).

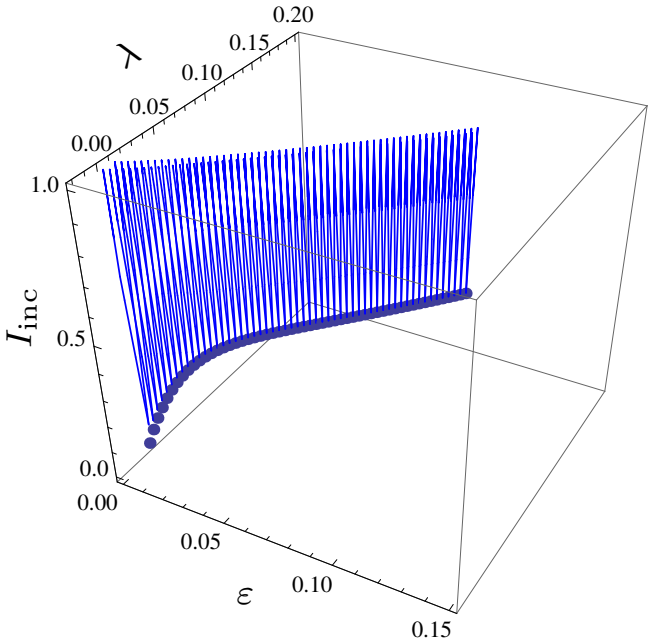

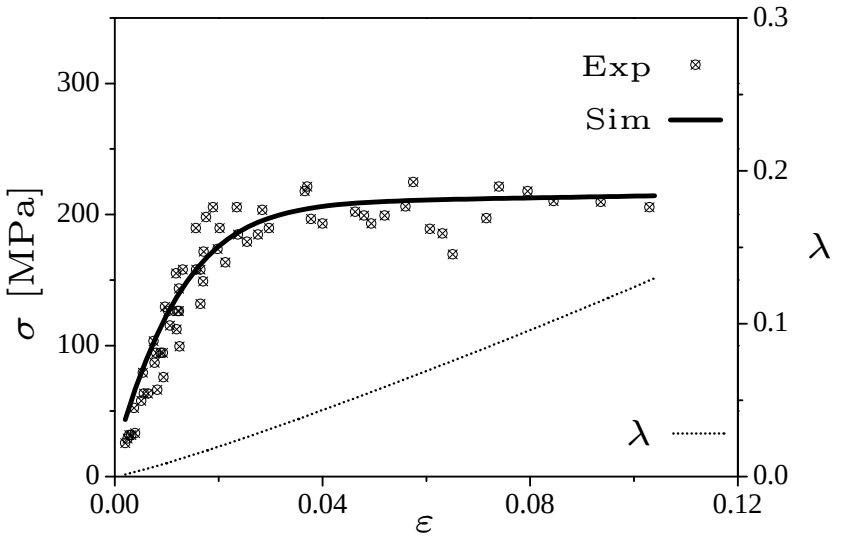

Figure 7.3: (*continued*) sample C

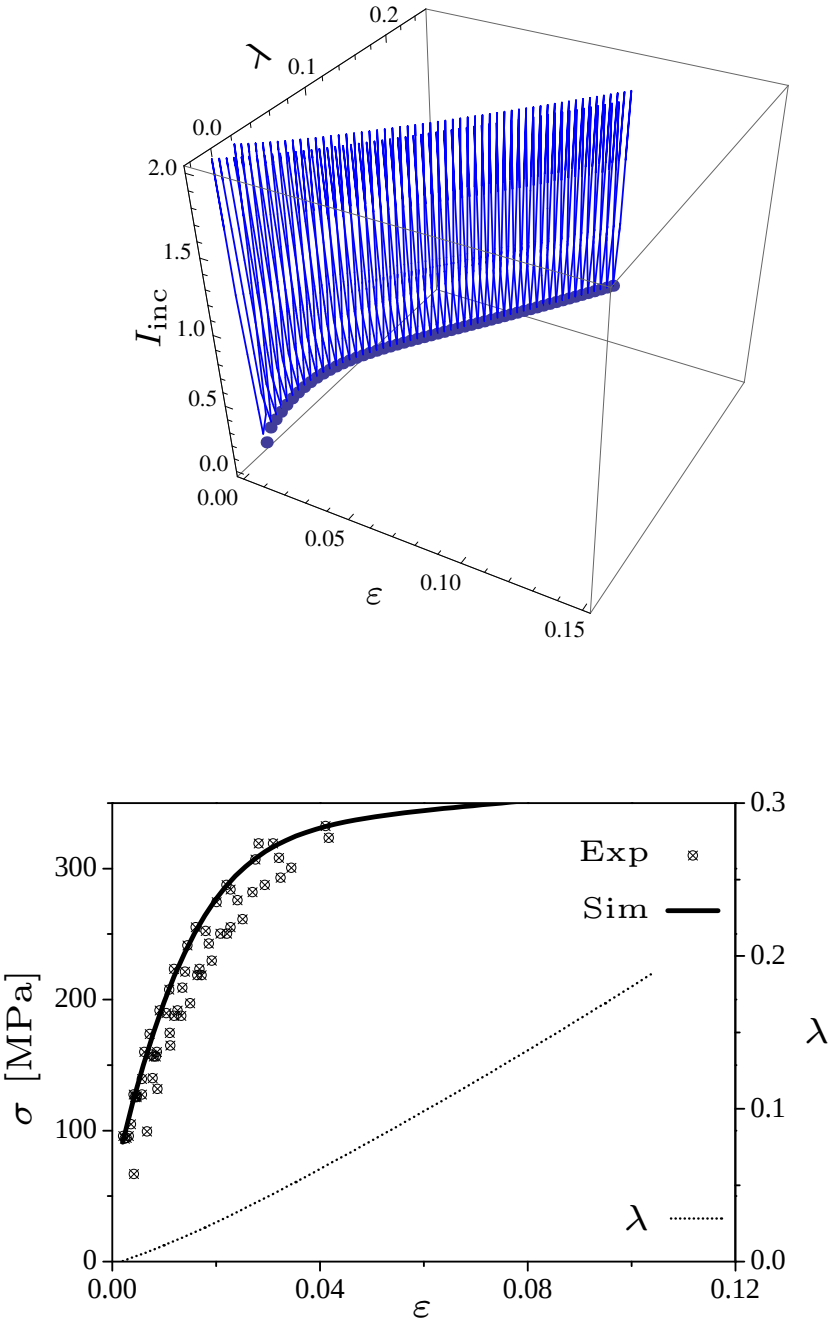

Figure 7.3: (*continued*) sample A

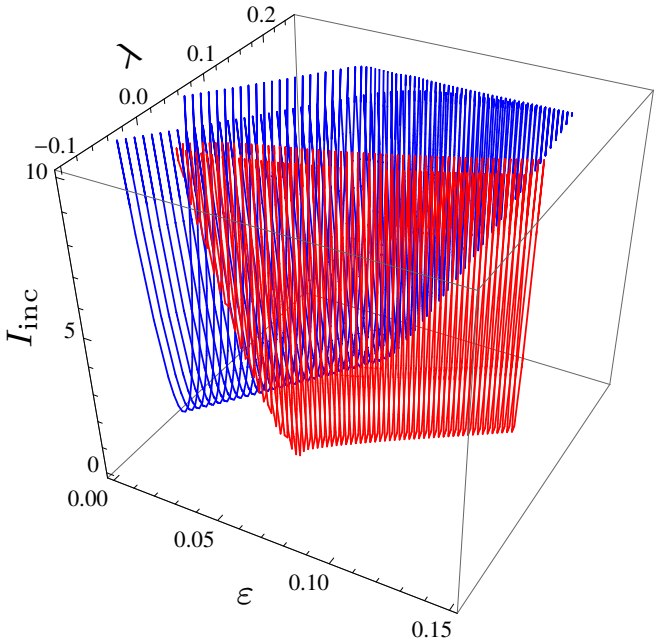

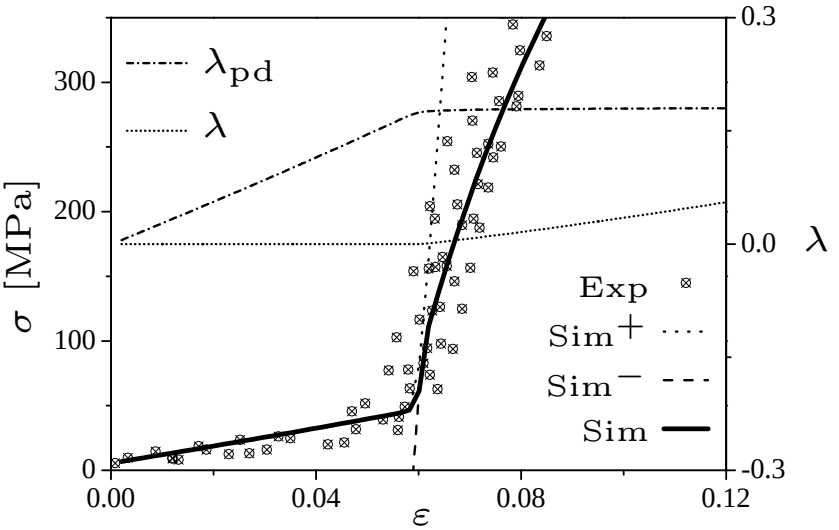

Figure 7.3: (*continued*) sample E

8 Modeling of texture evolution in a polycrystal

In the previous chapter, the concept of pseudo-dislocation twinning was developed at the micro-scale (at the scale of a single crystal). This chapter is devoted to analyze the behavior of a polycrystal using the proposed twinning model. Special focus is on the texture evolution during rolling process.

8.1 Viscous approximation

The algorithm summarized in the previous chapter describes twinning and crystal slip by means of a fully variational method. Although it is physically sound and numerically efficient, so-called *variational constitutive updates* can nowadays still not be considered as standard. By ways of contrast, implementations for standard crystal plasticity theory are available for a broad range of different finite element programs. For this reason, an approximation of the novel variational model is discussed here which allows to use standard viscoplastic crystal plasticity models. A similar strategy has already been reported earlier, e.g., in Staroselsky & Anand (2003); Forest & Parisot (2000). It bears emphasis that the additional viscosity is not related to the material, but it is introduced for relaxing the ill-posed problem of rate-independent crystal plasticity theory, cf. Schmidt-Baldassari (2003).

Instead of computing the plastic multipliers $\zeta^{(a)}$ from the consistency condition $\dot{\phi}^{(a)} = 0$, the viscous-type over-stress model

$$\dot{\zeta}^{(a)} = \zeta_0^{(a)} \langle \frac{\phi^{(a)}(\boldsymbol{\Sigma}, \boldsymbol{Q})}{\Upsilon} \rangle^n \tag{8.1}$$

is introduced. Here, Υ and $\zeta_0^{(a)}$ are material parameters, $\langle \bullet \rangle$ are the Macaulay brackets and n determines the rate sensitivity, see Rice (1971); Peirce et al. (1982). Since this viscous law is utilized here only for regularizing the rate-independent limiting case, the admissible choice $\Upsilon = 1$ and $\lambda_0 = 1$ is made. Clearly, by choosing n sufficiently large, Eq. (8.1) is a good approximation of the rate-independent case. This is precisely, the underlying idea of the viscous-type approximation. For dislocation slip and PD-twinning, a yield function $\phi^{(a)}$ of the type (4.20) is adopted. The remaining variables such as those

defining the hardening response (Ψ^{p}) are chosen in line with those utilized for the variational model discussed in the previous subsection. With this, the model describing the initial phase and that corresponding to the twinned phase are completed.

The final point to be addressed is a criterion for the phase transition. In principle, the energy based strategy as employed within the variational method could also be applied here. However, this would require an additional computation of the energies. Instead an equivalent strain-based criterion is employed. As explained in Section 6.2.2.1, twinning occurs, when the PD-twinning slip λ_{pd} reaches a critical threshold. Hence, for the advancing time step Δt, the final algorithm reads

$$\boldsymbol{e}_{t+\Delta t} = \begin{cases} \boldsymbol{e}_t & \text{if } (\lambda_{\mathrm{pd}} < \lambda_{\mathrm{Twin}}) \\ (-\boldsymbol{1} + 2(\boldsymbol{n} \otimes \boldsymbol{n})) \cdot \boldsymbol{e}_t & \text{if } (\lambda_{\mathrm{pd}} \geq \lambda_{\mathrm{Twin}}) \end{cases} \tag{8.2}$$

where the vector $\boldsymbol{e}$ determines the local material orientation, and the threshold λ_{Twin} corresponds to the twinning-induced shear.

8.1.1 Comparison between the variationally consistent model (Section 6.3) and its visco-plastic approximation (Section 8.1)

The numerical results reported in Chapter 7 were obtained by applying the variationally consistent model (see Section 6.3). Here, the quality of its visco-plastic approximation is analyzed. Particularly, the influence of the rate sensitivity power n is studied. Clearly, from a physical point of view, n has to be chosen sufficiently large. However, if n is too large, numerical problems can occur. The results for different rate sensitivity powers are summarized in Fig. 8.1. According to Fig. 8.1, $n = 100$ approximates the rate-independent case sufficiently accurately by not causing any numerical problems. Therefore, $n = 100$ seems to be a promising choice.

8.2 Texture evolution in a polycrystal

Having discussed the presented crystal plasticity model in detail, its application to the analysis of a polycrystal is investigated here. More precisely, the texture evolution of a polycrystal during a rolling process is considered. For that purpose, a representative volume element (RVE) consisting of $8 \times 8 \times 8 = 512$ eight-noded linear 3D hexahedron elements with 8 integration points is considered. In line with computational homogenization theory (see Miehe (2002)), periodic boundary conditions are enforced. The prescribed macroscopic strain inducing certain constraints at the boundary of the RVE (see

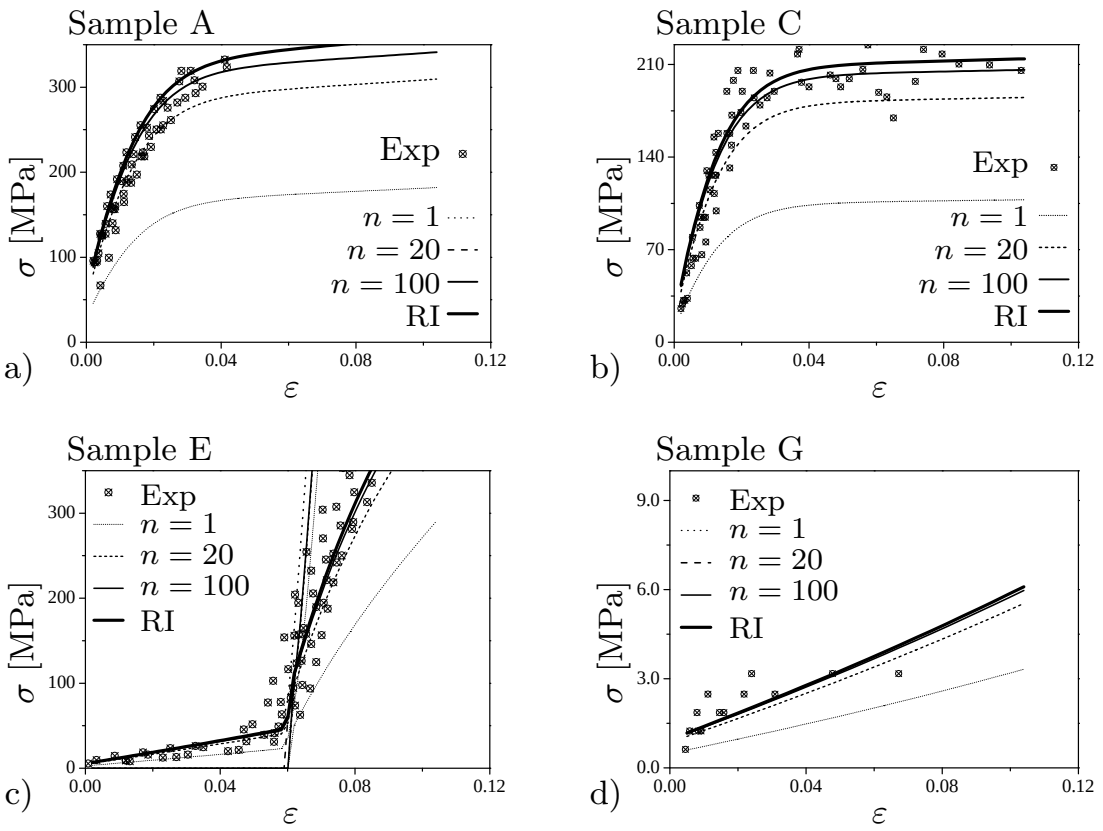

Figure 8.1: Channel die test: Comparison between the numerical results of the rate-independent variational method (Section 6.3) and the over-stress viscoplastic model (Section 8.1). n denotes the rate sensitivity power and RI denotes the rate-independent case (Section 6.3)

(Miehe, 2002; Graff et al., 2007; Levesque et al., 2010)) is assumed to be plain strain compression $\mathrm{diag}\boldsymbol{F} = \{\varepsilon; \tilde{\varepsilon}; 1\}$. The pole figure in Fig. 8.2a depicts the initial texture with 4096=512x8 randomly distributed grain orientations which represents the texture of an as-cast ingot, cf. (Agnew et al., 2001; Lee et al., 2010).

The texture evolution is governed by plastic deformations as well as by twinning. For the basal planes it is presented in Fig. 8.2a-c. The saturation of the basal poles toward the compression axis implies that basal slip is very pronounced. However, after 0.68 compression strain, the basal poles are inclined about 20 degrees out of the compression axis toward the extension direction. This is in good agreement with the results reported in Agnew et al. (2001) using a visco-plastic self consistent approach and also cf. (Agnew & Duygulu, 2005; Levesque et al., 2010; Proust et al., 2009; Beausir et al., 2008). The incremental activities of the different deformation systems versus the true compression strain are depicted in Fig. 8.3.

Fig. 8.3 also includes the total volume $V_R = \frac{n_R}{512\times 8}$ of the reoriented grains, where n_R denotes the number of those grains. According to Fig. 8.3, the contribution of basal and pyramidal slip to the total plastic deformation is about 60%. Although PD-twinning is active during the early stages of loading, further slip is bounded by the penalty function $(\Pi(\lambda_{\mathrm{pd}}))$. Consequently, the reoriented volume is bounded and reaches only 25% (at 0.6 compression strain). The deformation activities of the basal slip systems are fully consistent with the texture evolution shown in Fig. 8.2, i.e., basal slip is very pronounced.

Remark 15 *From an applicational point view, the analysis of the stress-strain-response characterizing the polycrystal is, in addition to the texture evolution, also very important. Evidently, this response depends strongly on the grain topology, e.g., the shape of the grains, cf. Lenhart (1955); Mathis et al. (2004); Gan et al. (2009). For the simulation of the polycrystal presented here, the material parameters as calibrated according to the channel die test have been used. However, the topology of the grains in the channel dies test (cubic single crystal) and that of the grains in the polycrystal are significantly different. Therefore, the results obtained from the numerical analysis of the polycrystal can only be interpreted in a qualitative manner. Consequently, for a quantitative description of a polycrystal, the material parameters have to be calibrated again for the considered grain topology.*

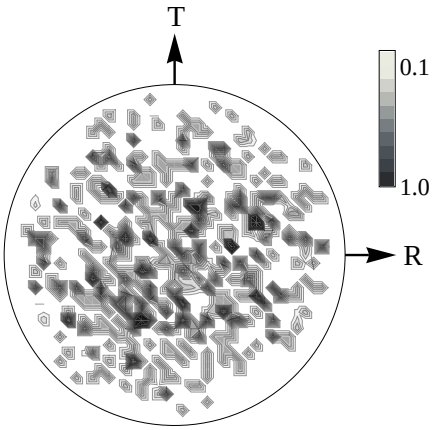

(a) $\varepsilon = 0.00$

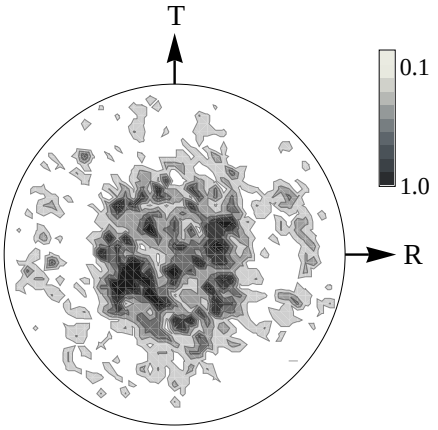

(b) $\varepsilon = -0.68$

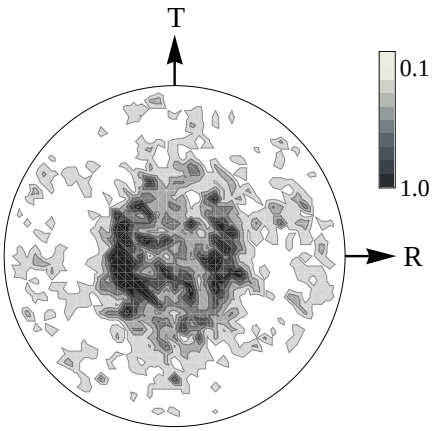

(c) $\varepsilon = -1.20$

Figure 8.2: Simulation of a rolling process: Pole figure showing the evolution of the basal texture

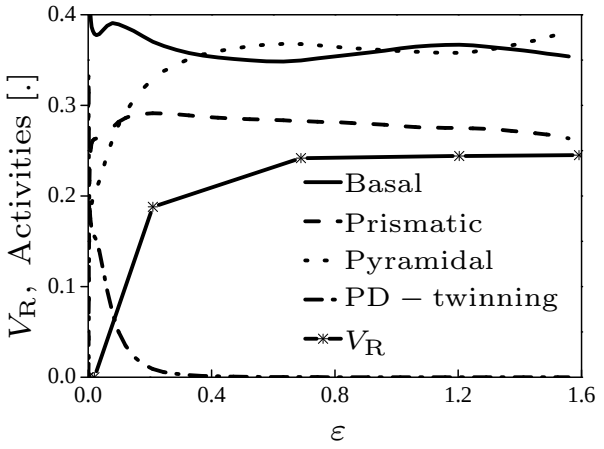

Figure 8.3: Simulation of a rolling process: Activities of the magnesium deformation systems versus the true compression strain. V_{R} denotes the volume of the rotated grains.

9 Modeling of twinning by sequential laminates

This chapter is devoted to a more detailed and physically more exact analysis of the microstructure of deformation-induced twinning in magnesium during a channel die test. For that purpose, several models including some capturing a size effect are elaborated.

9.1 Introduction

For analyzing the evolution of microstructures, models based on phase transformation represent a suitable choice, cf. James (1981); Ball & James (1987); Kohn (1991); Kohn & Müller (1992); James et al. (1995); Ortiz & Repetto (1999); Mueller (1999); James & Hane (2000); Carstensen et al. (2002); Miehe & Lambrecht (2003); Aubry & Ortiz (2003). Within such models the total deformation can be split into the physically most important parts by an enhanced multiplicative decomposition, see Boyce et al. (1992); Levitas (1998); Idesman et al. (2000); Meggyes (2001). Although the concept of phase decomposition and that of the enhanced multiplicative decomposition have been extensively used for studying phase transformation, none of these models have been developed for the irreversible deformation in magnesium.

9.2 Kinematics of twinning

In this section, the kinematics associated with deformation-induced twinning is described in a more detailed manner (compared to the previous chapters). In line with James (1981), the deformation between the initial phase and the twinning phase is coupled by a Hadamard-type compatibility condition, cf. Eq. 6.3. More precisely, twinning is considered as a certain rank-one convexification (Ortiz & Repetto, 1999; Carstensen et al., 2002). The presented framework is very general and applies also to higher-order laminates. As a matter of fact, second-order laminate structures will be analyzed within the numerical examples. Within each phase showing the original lattice structure, a standard multiplicative decomposition of the deformation gradient is adopted, while an extended decomposition is elaborated for the twinning phase. This extended decomposition accounts for the lattice re-orientation, the shear strain induced

by twinning as well as for the deformation history prior to twinning. Since the total deformation associated with the aforementioned laminate structure does not fulfill the Hadamard compatibility condition, an additional boundary layer is introduced. By doing so, a compatible deformation field can be constructed.

9.2.1 Deformation within the initial phase and the twinning phase

Analogously to the crystal plasticity model discussed in Section 4.2.1, a multiplicative decomposition of the deformation is adopted. Accordingly, for the deformation of the initial phase without twinning which is highlighted by the superscript (+) in what follows, the standard split

$$\boldsymbol{F}^{+} = \boldsymbol{F}^{\mathrm{e}+} \cdot \boldsymbol{F}^{\mathrm{p}+} \tag{9.1}$$

is used. By way of contrast, additional deformation modes have to be taken into account in the twinning phase. The first of those is the twinning-induced shear strain a.k.a. intrinsic phase distortion, see e.g., James (1981); Mueller (1999); Aubry et al. (2003). The respective deformation gradient reads

$$\boldsymbol{F}_{\mathrm{Twin}} = \boldsymbol{I} + (\boldsymbol{a} \otimes \boldsymbol{n}) \tag{9.2}$$

with $\boldsymbol{n}$ ($||\boldsymbol{n}|| = 1$) and $\boldsymbol{a}$ being two vectors corresponding to the twinning plane and the shear direction. The amplitude of twinning $||\boldsymbol{a}||$ is related to the type of crystal lattice. In the case of HCP metals, it is dictated by the crystal axial ratio, i.e., $||\boldsymbol{a}|| = f(c/a)$, see Christian & Mahajan (1995). The second deformation mode which has also to be considered within the twinning phase is the deformation history, e.g., the phase could have already experienced dislocation slip before twinning. Such deformations are represented by the deformation gradient $\boldsymbol{F}_{\mathrm{Hist}}$. Combining the aforementioned deformation modes, the deformation gradients of the different phases are decomposed according to

- Initial phase before twinning (superscript +)

$$\boldsymbol{F}^{+} = \boldsymbol{F}^{\mathrm{e}+} \cdot \boldsymbol{F}^{\mathrm{p}+} \tag{9.3}$$

- New phase after twinning (superscript −)

$$\boldsymbol{F}^{-} = \boldsymbol{F}^{\mathrm{e}-} \cdot \boldsymbol{F}^{\mathrm{p}-} \cdot \boldsymbol{F}_{\mathrm{Twin}} \cdot \boldsymbol{F}_{\mathrm{Hist}}. \tag{9.4}$$

Analogously to classical crystal plasticity theory, the ordering of the different gradients in Eq. (9.4) has been chosen in line with the deformation chronology. Clearly, even with such a motivation, many questions regarding the multiplicative decomposition of $\boldsymbol{F}$ are still open and controversially discussed in the literature, see, e.g., Xiao et al. (2006) and references cited therein. However, they are far beyond the scope of the present work. In any case, decompositions

of the type (9.4) have already been successfully applied to a broad variety of different mechanical problems, cf. Boyce et al. (1992); Levitas (1998); Idesman et al. (2000); Meggyes (2001); Mosler & Bruhns (2009b).

A closer look at Eq. (9.3) and Eq. (9.4) reveals that the model has not been completely defined yet. More precisely, the deformation gradient $\boldsymbol{F}_{\mathrm{His}}$ needs further explanation. This variable is strongly related to the interaction between already existing dislocations and twinning. Unfortunately, only little experimental information is available, cf. Kim et al. (2009). Therefore, certain assumptions are required. One such assumption is that the deformation history is completely reset by twinning. In this case, $\boldsymbol{F}_{\mathrm{His}} = \boldsymbol{1}$ and consequently,

$$\boldsymbol{F}^{-} = \boldsymbol{F}^{\mathrm{e}-} \cdot \boldsymbol{F}^{\mathrm{p}-} \cdot \boldsymbol{F}_{\mathrm{Twin}}. \tag{9.5}$$

Alternatively, one could assume that the dislocation structures is not at all affected by twinning. This implies $\boldsymbol{F}_{\mathrm{His}} = \boldsymbol{F}^{\mathrm{p}+}$ and thus,

$$\boldsymbol{F}^{-} = \boldsymbol{F}^{\mathrm{e}-} \cdot \boldsymbol{F}^{\mathrm{p}-} \cdot \boldsymbol{F}_{\mathrm{Twin}} \cdot \boldsymbol{F}^{\mathrm{p}+}. \tag{9.6}$$

During deformation of the twinning phase, $\boldsymbol{F}_{\mathrm{His}} = \boldsymbol{F}^{\mathrm{p}+}$ remains constant in this case, cf. Hansen et al. (2010). In the present thesis, Eq. (9.5) is considered, since preliminary molecular dynamical simulations are in line with this assumption.

Remark 16 *Since twinning transforms the lattice of the initial phase to a new configuration, it can also affect the elastic properties. However, the elastic anisotropy of magnesium is not very pronounced and the elastic deformation is comparably small. Thus, an isotropic constitutive model is adopted. As a result, the elastic material parameters have been assumed as twinning invariant.*

9.2.2 Compatibility of deformation between the different phases

In the previous section, the deformation within each phase has been decomposed into the physically most relevant parts. However, the deformation gradients in such phases are evidently not completely independent. More precisely, both gradients have to fulfill the compatibility condition

$$\boldsymbol{F}^{-} - \boldsymbol{F}^{+} = (\boldsymbol{a} \otimes \boldsymbol{n}). \tag{9.7}$$

of Hadamard-type, cf. James (1981). Furthermore, the volume average of both gradients has to be identical to their macroscopic counterpart, i.e.,

$$\boldsymbol{F} = (1 - {}_1\xi)\, \boldsymbol{F}^{+} + {}_1\xi\, \boldsymbol{F}^{-}. \tag{9.8}$$

Here, ${}_1\xi = \mathrm{vol}(\Omega^-)/\mathrm{vol}(\Omega) \in [0;1]$ is the relative twinning volume and $\Omega := \Omega^- \cup \Omega^+$. A graphical interpretation of the resulting deformation implied by Eqs. (9.7) and (9.8) is shown in Fig. 9.1. While in the upper part of Fig. 9.1 a

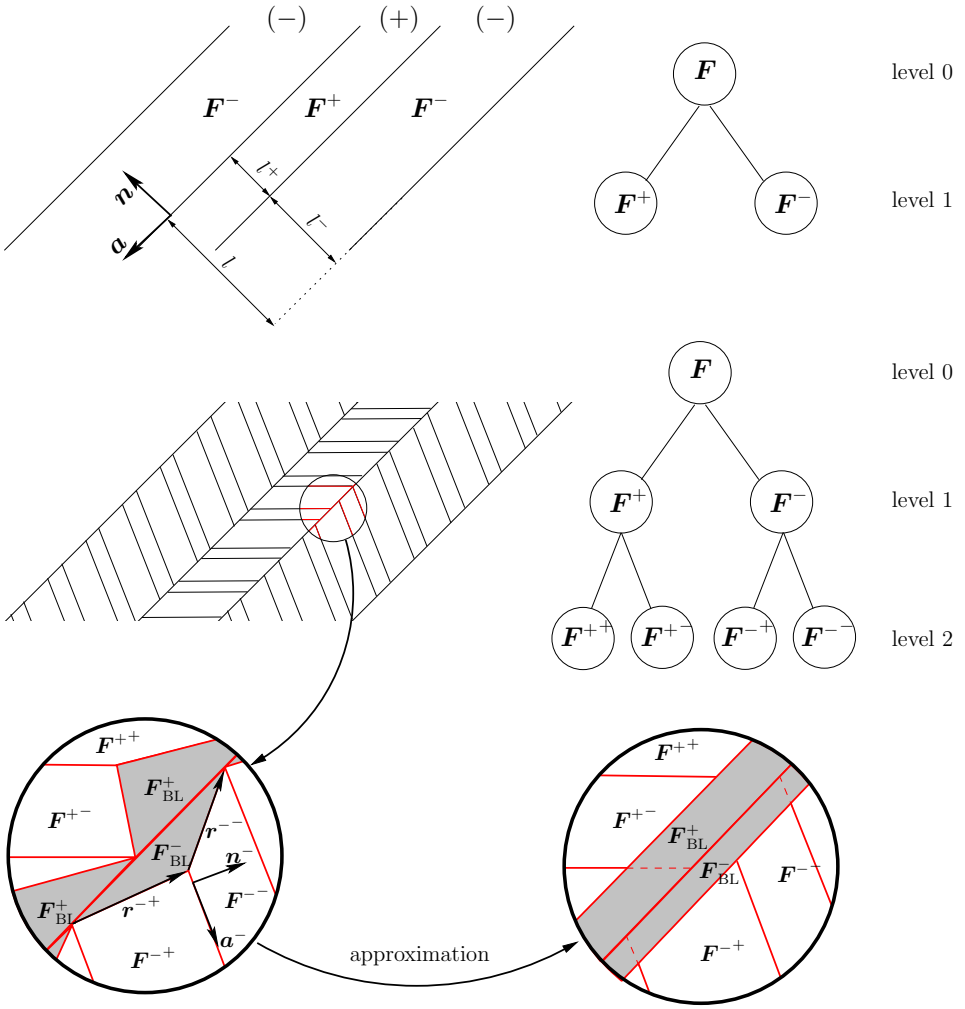

Figure 9.1: Schematic illustration of sequential laminates and their representative graph of deformation: top: rank-one laminates; middle: rank-two laminates; bottom left: magnification of the boundary layer which is necessary for a continuous deformation; bottom right: approximated boundary layer

periodic rank-one laminate is illustrated, a second-order laminate is depicted below that figure. Interestingly, such laminates have been observed in many materials, particularly in metals, cf. Mueller (1999); Ortiz & Repetto (1999); Kohn (1991); Pedregal (1993); Ortiz et al. (2000) and references cited therein. According to Fig. 9.1, twinning can be described by a binary tree structure consisting of leaves and branch joints. Each node of the tree corresponds to the deformation of one laminate $(\boldsymbol{F}^+; \boldsymbol{F}^-)$, while the deformation at the joint of two branches is associated with the volumetric average of the leaves' defor-

mations. The number of branching sequences defines the level of a laminate.

Remark 17 *In general, deformation-induced twinning can occur successively by several twinning variants. In this case, the aforementioned phase decomposition model has to be considered several times, see Fig. 9.1. For highlighting the laminate level, left subscripts will be used (${}_2\xi^-$). Alternatively, the number of superscripts of $\boldsymbol{F}$ shows this level as well. Hence, $\boldsymbol{F}^{+-}$ is a second order laminate. More precisely, the nth index of $\boldsymbol{F}$ corresponds to the nth phase decomposition.*

9.2.3 Deformation within the boundary layer

The Hadamard compatibility conditions (9.7) and (9.8) ensure that the deformation gradients associated with a rank-one laminate results from a continuous deformation. As a consequence and as shown in Fig. 9.1, the respective laminates fit perfectly together. It is well known that such a compatibility cannot be guaranteed anymore for higher-order laminates. Even if each phase decomposition fulfills the Hadamard compatibility conditions, the resulting deformation is usually not rank-one compatible. This incompatibility gives rise to the formation of boundary layers, i.e., misfits. Following Ortiz et al. (2000), the deformation gradient within such layers can be computed as

$$\boldsymbol{F}^{\pm}_{\mathrm{BL}} = \boldsymbol{F}^{\pm} + \boldsymbol{a}^{\pm} \otimes \boldsymbol{n}^{\pm}_{\mathrm{BL}} \tag{9.9}$$

with

$$\boldsymbol{n}^{\mp}_{\mathrm{BL}} = ({}_2\xi^{\mp})\ \frac{\boldsymbol{n}^{\mp} \cdot \boldsymbol{r}^{\mp+}}{|\boldsymbol{r}^{\mp+}|^2}\boldsymbol{r}^{\mp+} - (1 - {}_2\xi^{\mp})\ \frac{\boldsymbol{n}^{\mp} \cdot \boldsymbol{r}^{\mp-}}{|\boldsymbol{r}^{\mp-}|^2}\boldsymbol{r}^{\mp-}. \tag{9.10}$$

In the present manuscript and in line with Stupkiewicz & Petryk (2002); Petryk et al. (2003); Aubry et al. (2003); Kochmann & Le (2009), the deformation gradient (9.9) within the boundary layer is approximated by

$$\boldsymbol{F}^{\pm}_{\mathrm{BL}} = \boldsymbol{F}^{\pm}. \tag{9.11}$$

Accordingly, the wedge-shaped boundary layer (exact solution) is approximated by a parallelepiped. Evidently, Eq. (9.11) does not satisfy the Hadamard compatibility condition between the boundary layer and the adjacent leaves. However, if the number of laminates is sufficiently large, the difference between Eq. (9.9) and Eq. (9.11) is negligible, i.e., both gradients converge to one another. Experimental confirmation of thin boundary layers in microstructures showing twinning can be found, e.g., in Appel & Wagner (1998); Stupkiewicz & Petryk (2002), see Fig. (9.2).

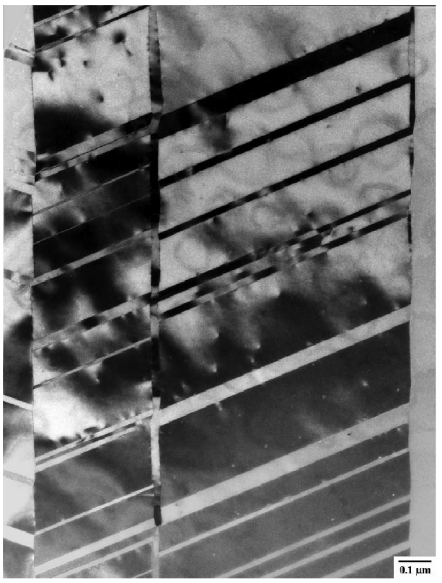

Figure 9.2: Twinning microstructure in Ti-Al alloy; see Appel & Wagner (1998) (reprint with permission)

9.2.4 Example: Kinematics associated with the channel die test (sample E)

In this section, the kinematics discussed before is specified for the channel die test, cf. Kelley & Hosford (1968). More precisely, the sample labeled as "E" is considered. For this sample, the twinning systems $\{[01\bar{1}1](0\bar{1}12)$, $[0\bar{1}11](01\bar{1}2)\}$ have been observed in the respective experiments. Furthermore, the Schmid factor of the basal system is zero and the activation energies of prismatic and pyramidal slip are much higher than that of tensile twinning, only tensile twinning is expected to be active. However, twinning reorients the parent crystal lattice about 90 degrees. As a result, it leads to different Schmid factors. For this reason, pyramidal dislocations of the type $\{[11\bar{2}\bar{3}](11\bar{2}2)$, $[\bar{1}\bar{2}\bar{1}\bar{3}](\bar{1}\bar{2}\bar{1}2)$, $[\bar{1}\bar{1}2\bar{3}](\bar{1}\bar{1}22)$, $[1\bar{2}1\bar{3}](1\bar{2}12)\}$ become active within the twinning phase.

Fig. (9.3) shows the aforementioned microstructure associated with sample "E". Accordingly, it corresponds to a second-order laminate. As discussed before, the second level of such laminates is due to twinning and consequently, the vectors $\boldsymbol{n}$ and $\boldsymbol{a}$ follow directly from crystallographic information, i.e., they are known in advance. By way of contrast, the amplitude of deformation cannot be determined a priori for the laminates of first order. Thus $||\boldsymbol{a}||$ represents an unknown in this case, see Remark 18 on page 90.

By combining the second-order laminate structure shown in Fig. 9.3 with the

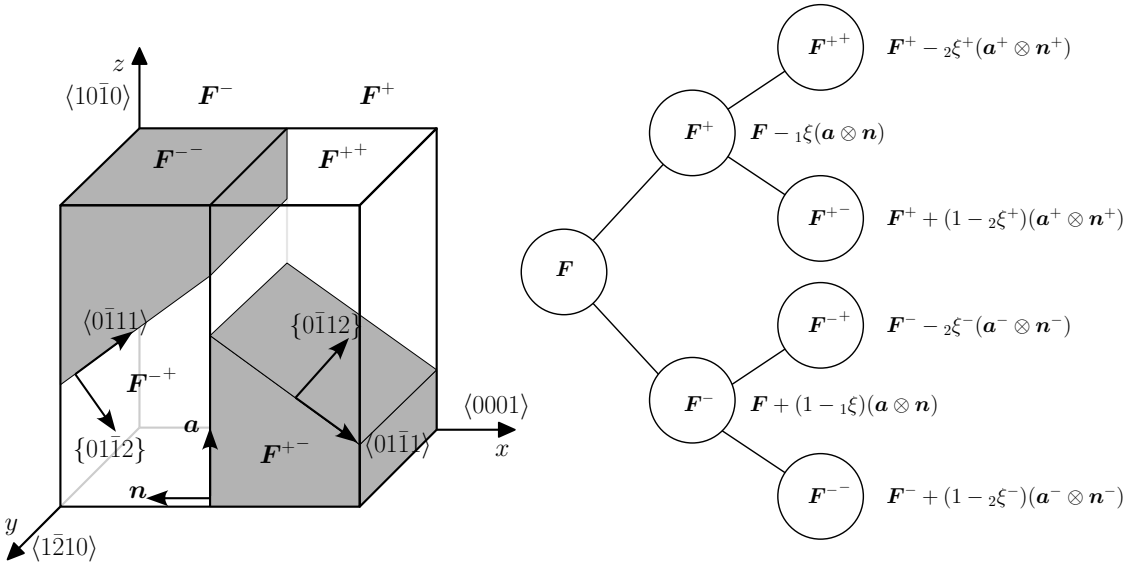

Figure 9.3: Left: schematic illustration of rank-one twinning laminates in a cubic single crystal sample; right: graph (tree) of the laminates' deformations

dislocation activities, the deformations within the different phases can be decomposed as

$$\boldsymbol{F}^{++} = \boldsymbol{F}^{\mathrm{e}++} \quad \text{and} \quad \boldsymbol{F}^{-+} = \boldsymbol{F}^{\mathrm{e}-+}, \tag{9.12}$$

$$\boldsymbol{F}^{+-} = \boldsymbol{F}^{\mathrm{e}+-} \cdot \boldsymbol{F}^{\mathrm{p}+-} \cdot \boldsymbol{F}_{\mathrm{Twin}_{\langle 01\bar{1}1\rangle\{0\bar{1}12\}}} \tag{9.13}$$

and

$$\boldsymbol{F}^{--} = \boldsymbol{F}^{\mathrm{e}--} \cdot \boldsymbol{F}^{\mathrm{p}--} \cdot \boldsymbol{F}_{\mathrm{Twin}_{\langle 0\bar{1}11\rangle\{01\bar{1}2\}}}. \tag{9.14}$$

As a consequence and in line with experimental observations, plastic deformations (dislocations) may only occur within the twinning phase. By way of contrast, the initial crystal is fully elastic for sample "E".

For describing nonlocal effects (size effects) related to the energy of the twinning interface, the number of such interfaces is defined. Neglecting other size effects, the thickness of the laminates is defined by

$$\text{level} \quad 0 \qquad l \;=:\; \text{Thickness of the sample} \tag{9.15}$$

$$\text{level} \quad 1 \qquad {}_1l^{+} \;=\; (1 - {}_1\xi)l \quad , \quad {}_1l^{-} \;=\; ({}_1\xi)l \tag{9.16}$$

$$\text{level} \quad 2 \qquad {}_2l^{++} \;=\; (1 - {}_2\xi^{+})\frac{{}_1l^{+}}{{}_2n^{+}} \quad , \quad {}_2l^{+-} \;=\; ({}_2\xi^{+})\frac{{}_1l^{+}}{{}_2n^{+}} \tag{9.17}$$

$$\text{level} \quad 2 \qquad {}_2l^{-+} \;=\; (1 - {}_2\xi^{-})\frac{{}_1l^{-}}{{}_2n^{-}} \quad , \quad {}_2l^{--} \;=\; ({}_2\xi^{-})\frac{{}_1l^{-}}{{}_2n^{-}} \tag{9.18}$$

where ${}_2n^+$ and ${}_2n^-$ indicate the number of laminates of the second level. With such definitions, the thickness of the boundary layer is obtained by using the shear distortion of the twinning laminate (see Fig. 9.4), i.e.,

$$\begin{aligned} {}_2l^+_{\mathrm{BL}} &= \frac{1}{2}\ {}_2\xi^+\ \lambda_{\mathrm{Twin}}\ {}_2l^{+-} \\ {}_2l^-_{\mathrm{BL}} &= \frac{1}{2}\ {}_2\xi^-\ \lambda_{\mathrm{Twin}}\ {}_2l^{--} \end{aligned} \tag{9.19}$$

and the volume fraction of the boundary layer can thus be described as a function of the twinning volume fraction, i.e.,

$${}_2\xi^\pm_{\mathrm{BL}} = f({}_2\xi^\pm) = \frac{1}{2}\ {}_2\xi^\pm\ \lambda_{\mathrm{Twin}}\ \sin(\theta)\ \left({}_2l^{\pm-}\right)^2\ \frac{w}{\mathrm{vol}(\Omega)}. \tag{9.20}$$

Here, w and θ are the width of the respective sample and the angle between the twinning interface and the rank-one laminate. According to Fig. (9.4), the boundary layer has been considered at the center of the specimen, cf. Kochmann & Le (2009).

Remark 18 *In general, the microstructure (order of laminate and its orientations), together with its induced deformation, is intrinsically unknown and has to be computed. As shown in the next section, it follows from minimizing the stress power of the respective solids, i.e., the energetically most favorable microstructures will form. Fortunately, due to the relatively simple boundary conditions and experimental observations, many variables can be a priori determined for sample "E" (see also Aubry et al. (2003)). For an overview, the variables defining the microstructure are summarized in Tab. 9.1.*

Table 9.1: List of microstructure related variables

${}_1\xi$	${}_2\xi^+ = {}_2\xi^-$	${}_2\xi^+_{\mathrm{BL}} = {}_2\xi^-_{\mathrm{BL}}$	${}_2n^+_{\mathrm{int}} = {}_2n^-_{\mathrm{int}}$
0.5	unknown	Eq. (9.20)	unknown

l	${}_1l^+ = {}_1l^-$	${}_2l^{++} = {}_2l^{-+}$	${}_2l^{+-} = {}_2l^{--}$
12.7 mm	$l/2$	unknown	unknown

	$\boldsymbol{a}$	$\boldsymbol{n}$	$\boldsymbol{a}^+$	$\boldsymbol{n}^+$	$\boldsymbol{a}^-$	$\boldsymbol{n}^-$
direction	$\langle\bar{1}010\rangle$	$\{000\bar{1}\}$	$\langle 01\bar{1}1\rangle$	$\{0\bar{1}12\}$	$\langle 0\bar{1}11\rangle$	$\{01\bar{1}2\}$
amplitude	unknown	1	0.35	1	0.35	1

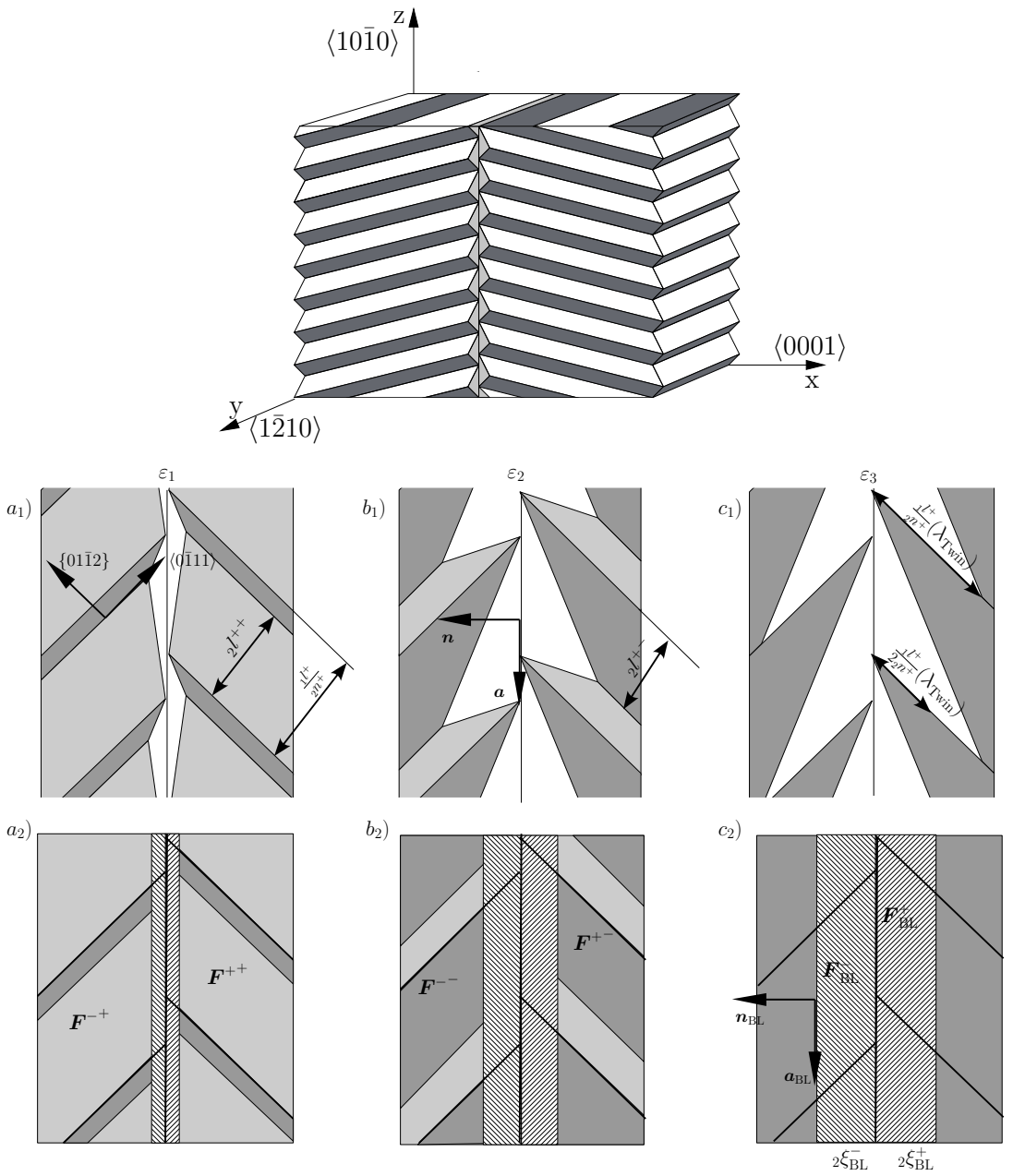

Figure 9.4: Schematic illustration of twinning evolution by means of rank-one laminates for monotonic loading (strain amplitudes: $\varepsilon_1 < \varepsilon_2 < \varepsilon_3$): Due to the misfit between higher-order laminates, wedge-shaped boundary layers are necessary for a continuous deformation (upper figure). They are approximated by a straight boundary layer (bottom figure).

9.3 Constitutive equations

Having discussed the kinematics associated with dislocation slip and deformation-induced twinning, focus is now on the constitutive equations. First, the

Helmholtz energy is elaborated in Subsection 9.3.1. Subsequently, the dissipation related to twinning is addressed in Subsection 9.3.2. The final model is summarized in Subsection 9.4 and numerical aspects concerning its implementation are also given. In line with the crystal plasticity model shown in Section 4.2.1, it is uniquely driven by energy minimization.

9.3.1 Helmholtz energy

9.3.1.1 Helmholtz energy within the different phases

Within each phase, the deformation may be purely elastic or elastoplastic as a result of dislocations. Accordingly and following Section 4.2.1, a Helmholtz energy of the type

$$\Psi = \Psi^{\mathrm{e}}(\boldsymbol{C}^{\mathrm{e}}) + \Psi^{\mathrm{p}}(\boldsymbol{\lambda}) \tag{9.21}$$

represents a suitable choice. As in the previous section, the elastic response is approximated by the neo-Hooke-type model (7.2), while the stored energy due to plastic work again is decomposed into self hardening and latent hardening effects, i.e.,

$$\Psi^{\mathrm{p}} = \Psi^{\mathrm{p}}(\boldsymbol{\lambda}) = \Psi^{\mathrm{p}}_{\mathrm{self}}(\boldsymbol{\lambda}) + \Psi^{\mathrm{p}}_{\mathrm{lat}}(\boldsymbol{\lambda}). \tag{9.22}$$

A size-dependence of the hardening parameters can be accounted for by assuming that Ψ^{p} depends also on the mean free path of dislocations, cf. Aubry et al. (2003); Hansen et al. (2010), i.e.,

$$\Psi^{\mathrm{p}} = \Psi^{\mathrm{p}}(\boldsymbol{\lambda}, \boldsymbol{h}) \tag{9.23}$$

with $\boldsymbol{h} = \{h^{(1)}, \dots h^{(n)}\}$ containing the mean free path of the n different dislocation systems. However, due to lack of experimental observation, such an enhanced model will not be used within the numerical examples presented in the next section. A size-effect of Hall-Petch-type will nevertheless be implemented by relating the yield limit $\Sigma_0^{(a)}$ to the mean free path of dislocations, cf. Eq. (9.27).

9.3.1.2 Helmholtz energy associated with the twinning interface

According to experimental measurements, the energy of twinning interfaces is relatively small compared to the elastic energy stored within the bulk, see Ball & James (1987); Morris et al. (2005). More precisely, the interface energy reported in Morris et al. (2005) is about $k = 0.140$ mJ/m^2. Based on this

measurement, the total energy of n_{int} interfaces showing a cross sectional area of A_{int} each is computed as

$$\Psi_{\mathrm{mix}}(n_{\mathrm{int}}, A_{\mathrm{ini}}) = k n_{\mathrm{int}} A_{\mathrm{int}}. \tag{9.24}$$

Clearly, a constant area specific energy is a comparably simple assumption. However, due to lack of experimental information, it seems to be appropriate. Furthermore and equally importantly, the presented constitutive framework is very general and allows also the incorporation of more complicated interface models.

9.3.1.3 Helmholtz energy associated with the boundary layer

Unfortunately, even less information is available about the boundary layer. More precisely, only the respective deformation gradient is known (see Eq. (9.9)). For this reason, a fully elastic response is assumed, i.e.,

$$\Psi_{\mathrm{BL}} = \Psi_{\mathrm{BL}}(\boldsymbol{C}). \tag{9.25}$$

In the numerical examples, the neo-Hooke-type model (7.2) is adopted. However, it bears emphasis that any elastoplastic model can easily be included as well.

9.3.1.4 Total Helmholtz energy

By summarizing the different Helmholtz energies introduced before, the total stored energy of a first-order laminate can be computed as

$$\begin{aligned}\Psi = (1-\xi_{\mathrm{BL}}) \left((1-\xi)\Psi^{+}(\boldsymbol{C}^{+}, \boldsymbol{\lambda}^{+}) + \xi\, \Psi^{-}(\boldsymbol{C}^{-}, \boldsymbol{\lambda}^{-}) \right) \\ + \xi_{\mathrm{BL}}\, \Psi_{\mathrm{BL}}(\boldsymbol{C}_{\mathrm{BL}}) + \Psi_{\mathrm{mix}}(n_{\mathrm{int}}, A_{\mathrm{int}}).\end{aligned} \tag{9.26}$$

Since the Helmholtz energy is an extensive variable, it decomposes additively. Although the Helmholtz energy has been specified here only for a first-order laminate, it can be generalized in a straightforward manner to the more general case. For that purpose, Eq. (9.26) has to be applied recursively. Further details are omitted here. However, they will be discussed in Subsection 9.4.

9.3.2 Dissipation and kinetics

9.3.2.1 Dissipation due to plastic deformation – dislocations within the different phases

In line with Section 4.2.1, dissipation due to plastic deformation is modeled by a functional being positively homogeneous of degree one. More precisely

and fully identical to Section 4.2.1,

$$\mathcal{D} = \sum_{a=1}^{n} \varsigma^{(a)}\ \Sigma_0^{(a)} \geq 0 \tag{9.27}$$

is considered. However and in sharp contrast to Section 4.2.1, a size-effect of Hall-Petch-type is accounted for. For this reason, the critical effective resolved shear stress $\tilde{\Sigma}_0$ is related to the mean free path of dislocations according to

$$\tilde{\Sigma}_0 = \Sigma_0 + \frac{T}{bh} \tag{9.28}$$

with h being the length of this path, b and T denoting material parameters (amplitude of the Burgers' vector and line tension) and Σ_0 representing the resolved shear stress of the local model (without Hall-Petch effect). Thus, the smaller this length, the higher the resolved shear stress Σ_0. Within the numerical simulations, the thickness of the laminates is taken as h.

9.3.2.2 Dissipation due to twinning nucleation

Analogously to dislocation slip, initiation of twinning lenticulars is also accommodated by elementary dislocations, see Christian & Mahajan (1995). Thus, a dissipation functional similar to Eq. (9.27) represents a suitable choice. Considering one active slip system and neglecting hardening effects, Eq. (9.27) can be re-written as

$$\varsigma^{(a)}\ \Sigma_0^{(a)} = \varsigma^{(a)}\ |\boldsymbol{\Sigma} : \left(\boldsymbol{s}^{(a)} \otimes \boldsymbol{m}^{(a)}\right)|. \tag{9.29}$$

As a result, a dissipation potential of the type

$$\mathcal{D}_{\text{int}} = \mu\, \hat{\epsilon}\, \dot{n}_{\text{int}}\, (\boldsymbol{\Sigma} : (\boldsymbol{a} \otimes \boldsymbol{n}))\,, \tag{9.30}$$

seems to be well suited for describing the kinetics associated with twinning nucleation. Here, $\hat{\epsilon}$ is a material parameter. It bears emphasis that twinning is a polar deformation system and thus, twinning initiation requires a positive resolved shear stress, see Christian & Mahajan (1995). Therefore and in contrast to Eq. (9.29), the sign of the driving force $(\boldsymbol{\Sigma} : (\boldsymbol{a} \otimes \boldsymbol{n}))$ is important. For instance, already existing twinning laminates can be annihilated under negative resolved shear stress ($\dot{n} < 0$). This is called *de-twinning*. Accordingly, n is not necessarily monotonically increasing and thus, the physical constraint $n \geq 0$ has to be carefully checked.

9.3.2.3 Dissipation due to propagation of twinning interfaces

Similarly to twinning initiation, zonal dislocations are again the underling physical mechanism associated with twinning propagation, see Christian & Mahajan (1995). Thus, the evolution equation governing such phenomena can be derived in line with those of ideal dislocation slip. Accordingly, the rate of twinning growth is assumed to be proportional to zonal dislocation slip, i.e.,

$$\xi \propto \frac{n_{\mathrm{zd}}}{\hat{n}_{\mathrm{zd}}} \tag{9.31}$$

where n_{zd} and $\hat{n}_{\mathrm{zd}}$ are the current number of zonal dislocations and the total number of zonal dislocations required for transforming the volume of the initial phase completely into the reoriented twinning phase. As a results, the total energy dissipation due to twinning propagation denoted as $\mathcal{D}_\xi$ can be formally written as

$$\int_{t_n}^{t_{n+1}} \mathcal{D}_\xi \, \mathrm{d}t \propto \Delta\xi \propto \Delta n_{\mathrm{zd}}. \tag{9.32}$$

Hence, the analogy between twinning propagation caused by zonal dislocations and dislocation slip suggests to use a dissipation functional being positively homogeneous of degree one in ξ. Summarizing this similarity and having in mind that the twinning volume can also decrease, a dissipation functional of the type

$$\mathcal{D}_\xi = \mu \, \epsilon \, \dot{\xi} \, (\boldsymbol{\Sigma} : (\boldsymbol{a} \otimes \boldsymbol{n})) \tag{9.33}$$

represents a physically sound choice. In Eq. (9.33), μ and ϵ are the elastic shear modulus and an additional material parameter, see Kochmann & Le (2009); Levitas & Ozsoy (2009). In line with twinning initiation, twinning propagation does also depend on the loading direction. More precisely, Eq. (9.33), together with the dissipation inequality $\mathcal{D}_\xi \geq 0$, leads to twinning or de-twinning depending on the sign of the driving force $\boldsymbol{\Sigma} : (\boldsymbol{a} \otimes \boldsymbol{n})$.

9.3.2.4 Total dissipation

By combining the different dissipative mechanisms analyzed within the previous paragraphs and accounting for the extensivity of energy, the total dissipation reads thus

$$\mathcal{D}_{\mathrm{total}} = \underbrace{(1 - \xi_{\mathrm{BL}}) \left((1 - \xi) \mathcal{D}^+ + \xi \, \mathcal{D}^- \right)}_{=: \, \mathcal{D}_{\mathrm{dis}}} + \mathcal{D}_\xi + \mathcal{D}_{\mathrm{int}}. \tag{9.34}$$

Accordingly, it consists of a term related to dislocation slip ($\mathcal{D}_{\text{dis}}$), a term associated with twinning initiation ($\mathcal{D}_{\text{int}}$) and a dissipation corresponding to twinning propagation ($\mathcal{D}_{\xi}$). Note that $\mathcal{D}_{\text{dis}}$ has the same structure as the Helmholtz energy of the bulk (compare $\mathcal{D}_{\text{dis}}$ to the first line in Eq. (9.26)).

9.4 The resulting nonlocal model for deformation-induced twinning – variational constitutive updates

In Section 4.2.1, standard crystal plasticity theory was recast into an equivalent variational principle. They key idea was the minimization of the stress power. The same method is also applied here. For that purpose, the stress power

$$\mathcal{E} = \dot{\Psi} + \mathcal{D}_{\text{total}} \tag{9.35}$$

is integrated over the time interval $[t_n; t_{n+1}]$ yielding the incrementally defined potential

$$I_{\text{inc}} = \int_{t_n}^{t_{n+1}} \{\dot{\Psi} + \mathcal{D}\} \, \mathrm{d}t = I_{\text{inc}}(\boldsymbol{F}, \boldsymbol{\lambda}^{-}, \boldsymbol{\lambda}^{+}, \xi, \xi_{\text{BL}}(\xi), n_{\text{int}}, \boldsymbol{a}, \boldsymbol{n}). \tag{9.36}$$

Here, a first-order laminate has been considered for the sake of simplicity. According to Eq. (9.36) and analogously to crystal plasticity, the functional depends on the macroscopic strains through $\boldsymbol{F}$ and on the internal variables related to dislocation slip ($\boldsymbol{\lambda}^{\pm}$). However, it is also affected by the microstructure $(\xi, \xi_{\text{BL}}(\xi), n_{\text{int}}, \boldsymbol{a}, \boldsymbol{n})$. As mentioned in Remark 18 on page 90, some of the microstructural parameters can be a priori computed for certain boundary value problems (e.g., due to symmetry). Based on Eq. (9.36), the unknowns are computed from the optimization problem

$$(\boldsymbol{\lambda}^{-}, \boldsymbol{\lambda}^{+}, \xi, \xi_{\text{BL}}(\xi), n_{\text{int}}, \boldsymbol{a}, \boldsymbol{n}) = \arg \inf_{\boldsymbol{\lambda}^{\pm}, \xi, \xi_{\text{BL}}(\xi), n_{\text{int}}, \boldsymbol{a}, \boldsymbol{n}} I_{\text{inc}} \tag{9.37}$$

and the stresses follow subsequently from

$$\boldsymbol{P} = \partial_{\boldsymbol{F}} \left(\inf_{\boldsymbol{\lambda}^{\pm}, \xi, \xi_{\text{BL}}(\xi), n_{\text{int}}, \boldsymbol{a}, \boldsymbol{n}} I_{\text{inc}} \right). \tag{9.38}$$

A careful analysis of Eqs. (9.35) and (9.36), together with the Helmholtz energy (9.26) and the dissipation functional (9.34), reveals that minimization principle (9.37) is indeed physically sound. More precisely, stationarity of I_{inc} with respect to the internal variables $\boldsymbol{\lambda}^{\pm}$ is equivalent to enforcing the yield functions, i.e., $\phi^{(a)} \leq 0$. This can be seen by noticing that the structure of the dissipation (9.34) and that of the Helmholtz energy (9.26) is identical for

all terms involving $\boldsymbol{\lambda}^{\pm}$. As a result, except for a factor c, this stationarity condition is equivalent to that of standard crystal plasticity, i.e.,

$$\partial_{\boldsymbol{\lambda}^+} I_{\text{inc}} = \partial_{\boldsymbol{\lambda}^+} \left\{ \underbrace{(1-\xi_{\text{BL}})\,\xi}_{=c} \underbrace{\left[\Psi^+_{n+1} + \sum_{a=1}^{n} \Delta\varsigma^{(a)}\, \Sigma_0^{(a)} \right]}_{\text{crystal plasticity}} \right\}. \tag{9.39}$$

Furthermore and as already pointed out in Ortiz et al. (2000), stability of I_{inc} with respect to the microstructural parameters $\boldsymbol{a}$, ξ and $\boldsymbol{n}$ is equivalent to traction equilibrium, configurational torque equilibrium and configurational force equilibrium at the internal interfaces, respectively. The final optimality condition with respect to the number of laminates can be physically interpreted as a balance condition between surface and bulk energies.

Based on recursively applying Eq. (9.36), the incrementally defined potential I_{inc} can also be derived for higher-order laminates. For instance, the second-order laminate analyzed within the next section is given by

$$\begin{aligned} I_{\text{inc}} = {} & (1 - {}_1\xi_{\text{BL}}) \left[(1 - {}_1\xi) I^+_{\text{inc}} + {}_1\xi\; I^-_{\text{inc}} \right] \\ & + (1 - {}_1\xi_{\text{BL}}) \int_{t_n}^{t_{n+1}} {}_1\left\{ \mathcal{D}_\xi + \mathcal{D}_{\text{int}} \right\} \, \mathrm{d}t + \int_{t_n}^{t_{n+1}} {}_1\xi_{\text{BL}}\; \Psi_{\text{BL}} \, \mathrm{d}t. \end{aligned} \tag{9.40}$$

Here, the first term is simply the volume average of the energies related to the first-order laminates, the second one is associated with dissipation due to twinning and the third terms corresponds to the boundary layer. Focusing on second-order laminates, the energies $I^{\pm}_{\text{inc}}$ are given by Eq. (9.36).

Remark 19 *For computing the incrementally defined potential I_{inc} a fully implicit time integration scheme is applied, see Eq. (9.36). While a classical backward Euler scheme is adopted for the scalar-value variables, the exponential mapping is used for integrating the flow rule, see Eq. (4.32).*

9.5 Numerical results and discussion

In this section, the novel model suitable for the prediction of the microstructure in magnesium is carefully analyzed by comparing experimental observations to numerically obtained results. For that purpose, the channel die test with the crystal orientation labeled as "E" is considered. A detailed description of the test and the induced mechanisms has already been given in Subsection 9.2.4. According to Subsection 9.2.4, the resulting deformation is approximated by a second-order laminate. The a priori known as well as the unknown parameters

describing the respective microstructure are summarized in Tab. 9.1. For highlighting the features of the model advocated in the present chapter, three different constitutive model are adopted. They are summarized below.

- Local model: size effects are excluded by neglecting the boundary layer and by fixing the number of laminates for each phase, i.e.,

$$ {}_2\xi_{\mathrm{BL}}^{\pm} = 0, \quad {}_2n^{\pm} = 1. \tag{9.41}$$

- Non-local, dislocation-free model: Dislocations within the different phases are completely neglected, i.e.,

$$ {}_2\boldsymbol{\lambda}^{\pm} = 0, \quad \boldsymbol{F}^{\pm\pm} = \boldsymbol{F}^{\mathrm{e}\pm\pm}, \quad \boldsymbol{F}^{\mathrm{p}\pm\pm} = \boldsymbol{I}. \tag{9.42}$$

- Fully nonlocal model including dislocation slip

The material parameters used within the different models are given in Tab. 9.2. By comparing Tab. 9.2 to Tab. 7.2, one can see that the parameters describing

Table 9.2: Material parameters used in the numerical analysis

Elastic Properties	$\lambda_{\mathrm{E}} = 34$(GPa)		$\mu = 17$ (GPa)	
Hardening parameters: Pyramidal system				
Σ_0 (MPa)	h_0 (MPa)	Σ_∞ (MPa)	l^{ab}	b (nm)
25	7100	105	25	6
Twinning related material parameters				
λ_{Twin}	ϵ	$\hat{\epsilon}$	k (mJ/m^2)	T (N)
0.35	2×10^{-4}	2×10^{-4}	0.140	0.03×10^{-9}

the elastoplastic response of the respective solids have not been changed.

The stress response as predicted by the different models, together with the experimentally measured data (see Kelley & Hosford (1968)), is shown in Fig. 9.5. While the left figure covers the whole loading range, a zoom in of the first loading stage is depicted on the right hand side. This magnification reveals that the difference between the models is only minor until the twinning phase becomes more dominant. More precisely, the mechanical response is predicted as slightly stiffer, if the boundary layer and the interface energy are taken into account. The relatively small increase in stiffness is due to the relatively low area specific energy k. The evolution of the twinning volume fractions ${}_{\{1,2\}}\xi^{\pm}$ is illustrated in Fig. 9.6. Accordingly, the first loading stage is associated with a transformation of the initial phase to the twinning phase. When the twinning process is completed, the new phase becomes active, resulting in a significant macroscopic hardening effect (see $\varepsilon > 0.06$ in Fig. 9.5). As evident in Fig. 9.5, all models capture this transition very well. However, the nonlocal

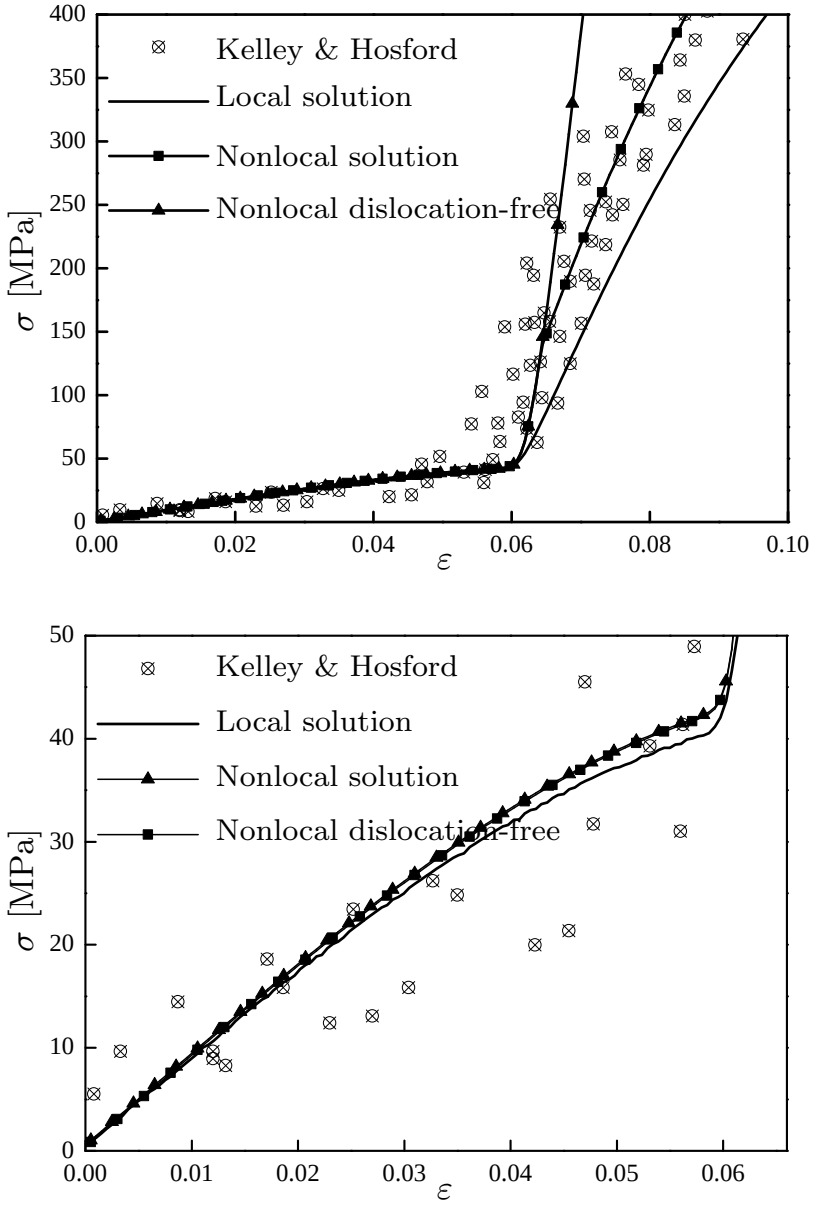

Figure 9.5: Channel die experiment (see Kelley & Hosford (1968)): comparison between experimentally measured data and computed stress-strain response. The bottom figure represents a zoom in of that on the top. Within the diagrams, the true stress vs. the true strain has been plotted.

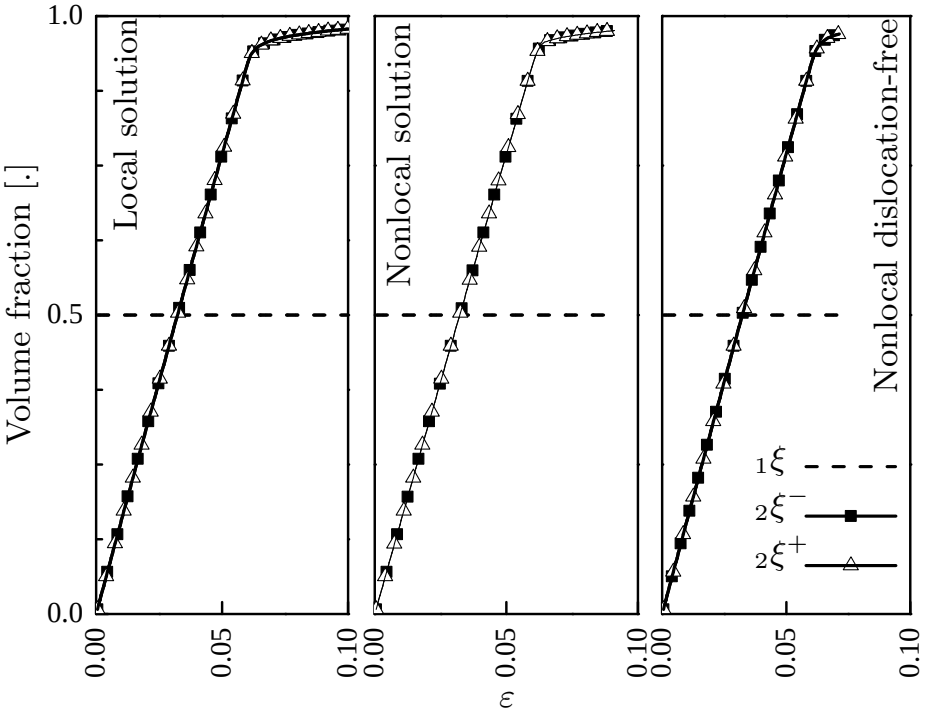

Figure 9.6: Channel die experiment (see Kelley & Hosford (1968)): evolution of the twinning volume fraction

dislocation-free model over predicts the stiffness of the twinning phase. Contrariwise, the solid is predicted as too weak, if the crystal is allowed to further relax by neglecting the boundary layer. The best stress-strain response is obtained for the fully nonlocal model taking also dislocation-related hardening effects into account. It bears emphasis that the analyzed example is relatively benign, e.g., monotonic, radial loading. Consequently, unrealistic elastic unloading as predicted by the nonlocal model without dislocation slip cannot be seen. Furthermore, since only one specimen size is investigated in Kelley & Hosford (1968) and the interface energy is relatively low, the difference between the local model and its nonlocal extension is relatively small. A key difference between the local model and its nonlocal extension can nevertheless be seen in Fig. 9.7. This figure shows the number of laminates during loading. Clearly, this number cannot be computed by means of a purely local theory. According to Fig. 9.7, the total number of laminates ($_2n^+ + {}_2n^-$) reaches 7000 at $\varepsilon_{zz} = 0.06$. Considering the initial size of the single crystal (see Kelley & Hosford (1968)) as well as the evolution of the twinning volume fractions $_{\{1,2\}}\xi^{\pm}$, the thickness of such laminates can be computed, see Fig. 9.7. As evident from Fig. 9.7, the model leads to thick laminates during the early stages of deformation. For the analyzed example, this thickness decreases monotonically. Beyond $\varepsilon = 0.06$, the microstructure consists of very fine laminates

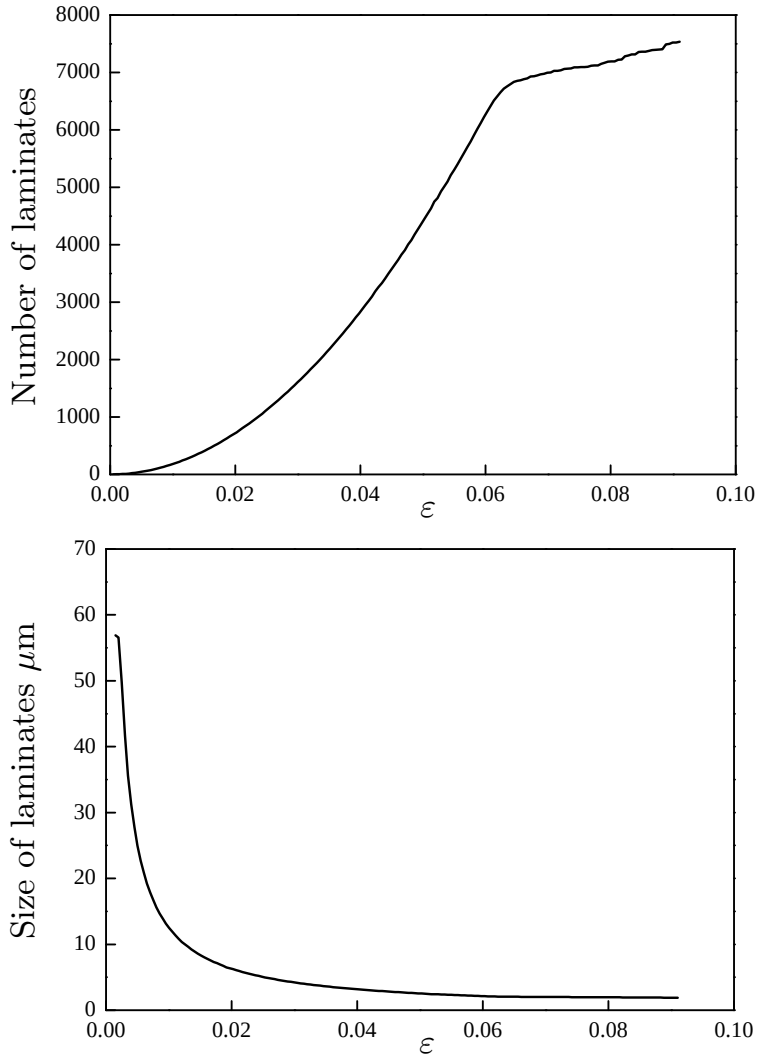

Figure 9.7: Channel die experiment (see Kelley & Hosford (1968)): top: evolution of the number of laminates of the second level ($_2n^+ + _2n^-$); bottom: numerically predicted size of the rank-two laminates layers

($< 3\mu$m) and more than 97% of the volume has been transformed to the twinning phase, cf. Fig. 9.6. Similar trends were also reported, e.g., in Hansen et al. (2010).

10 Summary and outlook

The focus of the present thesis was on the theoretical analysis of dislocation slip and deformation-induced twinning using a thermodynamically consistent framework. Particularly, the complex interplay between these deformation modes has been investigated. For that purpose, several enhanced models have been proposed. More precisely, an incremental minimization principle was derived which allows to determine the unknown dislocation slip rates by computing the stationarity conditions of a (pseudo) potential. By combining this principle within the concept of pseudo-dislocations, a novel constitutive model for magnesium was elaborated. Within this model the reorientation of the crystal lattice is applied when the part of the Helmholtz energy characterizing the pseudo-dislocation system reaches a certain threshold value.

This physically questionable decomposition of the twinning history into pseudo-dislocations followed by a reorientation of the total crystal can be naturally avoided by sequential laminate theory. The final model captures the transformation of the crystal lattice due to twinning in a continuous fashion by simultaneously taking dislocation slip within both, possibly co-existent, phases into account. The shear strain imposed by twinning as well as the deformation history were consistently included within the twinned domain by an enhanced multiplicative decomposition of the deformation gradient. Furthermore, the Helmholtz energy of the twinning interfaces and that of the boundary layer necessary for fulfilling the boundary conditions were explicitly considered. Analogously, the energy due to twinning nucleation and that related to twinning growth were also accounted for by suitable dissipation functionals. By doing so, the plastic deformation due to dislocations, the total volume of the twinning phase as well as the number of twin lamellas represent the unknowns to be computed within the resulting energy principle. Consequently, the thickness of the lamellas can be computed as well. By interpreting this thickness as the mean free path of dislocations, a size effect of Hall-Petch-type was naturally included within the novel model. Although the predictive capabilities of the final approach were only demonstrated for magnesium by analyzing the channel die test, the presented approach is very general and thus, it can also be applied to other materials showing twin lamellas.

Although the novel models proposed within the present thesis do capture the most important deformation systems in magnesium realistically, several further improvements of the constitutive laws are still needed. First of all, only rela-

tively simple boundary value problems have been considered within the model based on sequential laminates and solved numerically by a MATHEMATICA® code. For more complicated microstructures, a finite element implementation is required. A second, important enhancement of the advocated constitutive models is the incorporation of phase transformation due to recrystallization. This is of utmost importance for understanding the production-process-material-properties relation.

Bibliography

Agnew, S. R. & Duygulu, Ö. (2005): *Plastic anisotropy and the role of non-basal slip in magnesium alloy AZ31B*, in: International Journal of Plasticity, Volume 21, 1161–1193.

Agnew, S. R., Mehrotra, P., Lillo, T. M., Stoica, G. M. & Liaw, P. K. (2005): *Texture evolution of five wrought magnesium alloys during route A equal channel angular extrusion: Experiments and simulations*, in: Acta Materiala, Volume 53, 3135–3146.

Agnew, S. R., Yoo, M. H. & Tome, C. N. (2001): *Application of texture simulation to understanding mechanical behavior of Mg and solid solution alloys containing Li or Y*, in: Acta Materialia, Volume 49, 4277–4289.

Ando, S. & Tonda, H. (2000): *Non-basal slip in magnesium-lithium alloy single crystals*, in: Material Transactions, Volume 41, 1188–1191.

Appel, F. & Wagner, R. (1998): *Microstructure and deformation of two-phase γ-titanium aliminides*, in: Materials Science and Engineering, Volume 22, 187–268.

Argon, A. S. (2007): *Strengthening Mechanisms in Crystal Plasticity*, Oxford Series on Materials Modelling, Oxford University Press USA 2007.

Asaro, R. J. (1983): *Crystal plasticity*, in: Journal of Applied Mechanics, Volume 50, 921–934.

Asaro, R. J. & Needleman, A. (1985): *Texture development and strain hardening in rate dependent polycrystals*, in: Acta Metallurgica, Volume 33, 923–953.

Asaro, R. J. & Rice, J. R. (1977): *Strain localization in ductile single crystals*, in: Journal of the Mechanics and Physics of Solids, Volume 25, 309–338.

Ashby, M. F., Messler, R. W. & Asthana, R. (2009): *Engineering materials and processes desk reference*, 1 Edition, Elsevier 2009.

Aubry, S., Fago, M. & Ortiz, M. (2003): *A constrained sequential-lamination algorithm for the simulation of sub-grid microstructure in martensitic materials*, in: Computer Methods in Applied Mechanics and Engineering, Volume 192, 2823–2843.

Aubry, S. & Ortiz, M. (2003): *The mechanics of deformation-induced subgrain-dislocation structures in metallic crystals at large strains*, in: Proceeding of the Royal Society, Volume 459, 3131–3158.

Ball, J. M. (1977): *Convexity Conditions and Existence Theorems in Nonlinear Elasticity*, in: Archive for Rational Mechanics and Analysis, Volume 63, 337–403.

Ball, J. M. (1986): *Does Rank-one Convexity imply Quasicovecity*, Technical Report 262, Institute for mathematics and its applications, University of Minnesota, Minneapolls, Minesota 55455, 1986.

Ball, J. M. (2010): *Progress and puzzles in nonlinear elasticity*, Springer Wien-NewYork 2010, Volume 516 of *CISM Courses and Lectures*, pp. 1–15.

Ball, J. M. & James, R. D. (1987): *Fine phase mixtures as minimizers of energy*, in: Archive for Rational Mechanics and Analysis, Volume 100, 13–52.

Barber, D. J. & Wenk, H. R. (1979): *Deformation Twinning in Calcite, Dolomite, and Other Rhombohedral Carbonates*, in: Physics and Chemistry of Minerals, Volume 5, 141–165.

Barrett, C. S. (1949): *Cold Working of Metals*, A.S.M Cleveland 1949.

Beausir, B., Suwas, S., Tóth, L. S., Neale, K. W. & Fundenberger, J. J. (2008): *Analysis of texture evolution in magnesium during equal channel angular extrusion*, in: Acta Materialia, Volume 56, 200–214.

Bell, R. L. & Cahn, W. R. (1957): *The Dynamics of Twinning and the Interrelation of Slip and Twinning in Zinc Crystals*, in: Proceeding of the Royal Society, Volume 9, 494–521.

Bhattacharya, K., James, R. D. & Swart, P. J. (1997): *Relaxation in shape-memory alloys–Part I.*, in: Acta Materialia, Volume 45, 4547–4560.

Boyce, M. C., Montagut, E. L. & Argon, A. S. (1992): *The effects of thermomechanical coupling on the cold drawing process of glassy polymers*, in: Polymer Engineering & Science, Volume 32, 1073–1085.

Burke, E. C. (1952): *Plastic deformation of magnesium single crystals*, in: Transactions of the Metallurgical Society of AIME, Volume 194, 295–303.

Byer, C. M., Li, B., Cao, B. & Ramesh, K. T. (2010): *Microcompression of single-crystal magnesium*, in: Scripta Materialia, Volume 62, 536–539.

Carstensen, C., Hackl, K. & Mielke, A. (2002): *Non-convex potentials and microstructures in finite-strain plasticity*, in: Proceeding of the Royal Society A, Volume 458, 299–317.

Chen, S. J. & Howitt, D. G. (1998): *Observations of partial dislocations and basal twin boundaries in shock-wave-deformed sapphire*, in: Philosophical Magazine A, Volume 78, 765 –776.

Chia, K., Jung, K. & Conrad, H. (2005): *Dislocation density model for the effect of grain size on the flow stress of a Ti-15.2 at.beta-alloy at 4.2-650 K*, in: Materials Science and Engineering: A, Volume 409, 32–38.

Chin, G. Y. (1975): *Development of Deformation Textures, in Constitutive Equations in Plasticity*, The MIT Press 1975.

Christian, J. W. & Mahajan, S. (1995): *Deformation Twinning*, in: Progress in Materials Science, Volume 39, 1–157.

Ciarlet, P. (1988): *Mathematical elasticity. Volume I: Three-dimensional elasticity*, North-Holland Publishing Company 1988.

Coleman, B. D. (1964): *Thermodynamics of Materials with Memory*, in: Archive for Rational Mechanics and Analysis, Volume 17, 1–45.

Coleman, B. D. & Gurtin, M. E. (1967): *Thermodynamics with internal state variables*, in: Journal of Chemical Physics, Volume 47, 597–613.

Couling, S. L., Pashak, J. F. & Sturkey, L. (1959): *Unique Deformation and Aging Characteristics of Certain Magnesium-Base Alloys*, in: American Society for Metals Transactions, Volume 51, 94–107.

Cuitiño, A. & Ortiz, M. (1992): *Computational modeling of single crystals*, in: Modelling and Simulation in Materials Science and Engineering, Volume 1, 225–263.

Dacorogna, B. (2008): *Direct Methods in the Calculus of Variations*, Volume 78 of *Applied Mathematical Sciences*, second Edition, Springer Science New York 2008.

Dieter, G. E. (1986): *Mechanical Metallurgy*, McGraw-Hill 1986.

Ericksen, J. L. (1979): *On the symmetry of deformable crystals*, in: Archive for Rational Mechanics and Analysis, Volume 72, 1–13.

Forest, S. & Parisot, R. (2000): *Material Crystal Plasticity and Deformation Twinning*, in: Rendiconti del Seminario Matematico dell'Universita e del Politecnico di Torino, Volume 58, 99–111.

Frank, F. C. (1951): *Crystal dislocations. Elementary concepts and definitions*, in: Philosophical Magazine, Volume 42, 809–819.

Frank, F. C. & Read, W. T. (1950): *Multiplication process for slow moving dislocations*, in: Physical Review, Volume 79, 722–723.

Gan, W. M., Zheng, M. Y., Chang, H., Wang, X. J., Qiao, X. G., Wu, K., Schwebke, B. & Brokmeier, H. G. (2009): *Microstructure and tensile property of the ECAPed pure magnesium*, in: Journal of Alloys and Compounds, Volume 470, 256–262.

Ghosh, S. (1926): *On certain many valued solution of the equations of elastic equilibrium and their applications to the problem of dislocation in bodies with boundaries*, in: Bull. Calcutta Math. Soc., , 185.

Graff, S., Brocks, W. & Steglich, D. (2007): *Yielding of magnesium: From single crystal to polycrystalline aggregates*, in: International Journal of Plasticity, Volume 23, 1957–1978.

Hackl, K. & Fischer, F. D. (2008): *On the relation between the principle of maximum dissipation and inelastic evolution given by dissipation potentials*, in: Proceeding of the Royal Society A, Volume 464, 117–132.

Hadamard, J. (1903): *Leçons sur la propagation des ondes et les equations de l'hydrodynamigue*, Hermman Paris 1903.

Hansen, B. L., Bronkhorst, C. A. & Ortiz, M. (2010): *Dislocation subgrain structure and modeling the plastic hardening of metallic single crystals*, in: Modelling and Simulation in Materials Science and Engineering, Volume 18, 1–42.

Harrison, R. J., Redfern, S. A. T. & Salje, E. K. H. (2004): *Dynamical excitation and anelastic relaxation of ferroelastic domain walls in $LaAlO3$*, in: Physical Review B, Volume 69, 144101.

Haupt, P. (2000): *Continuum mechanics and theory of materials*, Springer-Verlag Berlin 2000.

Hauser, F. E., Starr, C. D., Tietz, L. & Dorn, J. E. (1955): *Deformation mechanisms in polycrystalline aggregates of magnesium*, in: Transactions of the ASM, Volume 47, 102–134.

Hill, R. (1966): *Generalized constitutive relations for incremental deformation of metal crystals by mutislip*, in: Journal of the Mechanics and Physics of Solids, Volume 14, 95–102.

Hill, R. (1968): *On constitutive inequalities for simple materials*, in: Journal of the Mechanics and Physics of Solids, Volume 16, 315–322.

Hill, R. (1972): *On Constitutive Macro-Variables for Heterogeneous Solids at Finite Strain*, in: Proceedings of the Royal Society, Volume 326, 131–147.

Hill, R. (1978): *Aspects of invariance in solid mechanics*, in: Advances in Applied Mechanics, Volume 18, 1–75.

Hirth, J. P. & Lothe, J. (1982): *Theory of Dislocations*, 2 Edition, Krieger Publishing Company Malaber, Florida 1982.

Holzapfel, A. G. (2000): *Nonlinear Solid Mechanics - A Continuum Approach for Engineering*, John Wiley & Sons Ltd., UK 2000.

Homayonifar, M. & Mosler, J. (2011): *On the coupling of plastic slip and deformation-induced twinning in magnesium: A variationally consistent approach based on energy minimization*, in: International Journal of Plasticity, Volume 27, 983–1003, in press.

Idesman, A. V., Levitas, V. I. & Stein, E. (2000): *Structural changes in elastoplastic material: a unified finite-element approach to phase transformation, twinning and fracture*, in: International Journal of Plasticity, Volume 16, 893–949.

James, R. D. (1981): *Finite Deformation by Mechanical Twinning*, in: Archive for Rational Mechanics and Analysis, Volume 77, 143–176.

James, R. D. & Hane, K. F. (2000): *Martensitic transformations and shape-memory materials*, in: Acta Materialia, Volume 48, 197–222.

James, R. D., Kohn, R. V. & Shield, T. W. (1995): *Modeling of Branched Needle Microstructures at the Edge of a martensite Laminate*, in: Journal de Physique IV, Colloque C8, supplement au Journal de Physique III, Volume 5, 253–259.

Jin, N. Y. & Winter, A. T. (1984): *Dislocation structures in cyclically deformed* [001] *copper crystals*, in: Acta Metallurgica, Volume 32, 1173–1176.

Kelley, E. W. & Hosford, W. F. (1968): *Plane-strain compression of magnesium and magnesium alloy crystals*, in: Transactions of the Metallurgical Society of AIME, Volume 242, 654–661.

Kim, G. S., Yi, S., Huang, Y. & Lilleodden, E. (2009): *Twining and Slip Activity in Magnesium* $< 11\bar{2}0 >$ *Single Crystal*, in: *Mechanical Behavior at Small Scales – Experiments and Modeling*, 2009, Volume 1224 of *MRS Proceedings*.

Kintzel, O. (2007): *Modeling of elasto-plastic material behavior and ductile micropore damage of metallic materials at large deformations*, Bochum - Germany 2007, Dissertation, Ruhr-Universität.

Kochmann, D. M. & Le, K. C. (2009): *A continuum model for initiation and evolution of deformation twinning*, in: Journal of the Mechanics and Physics of Solids, Volume 57, 987–1002.

Kohn, R. V. (1991): *The relaxation of a double-well energy*, in: Continuum Mechanics and Thermodynamics, Volume 3, 193–236.

Kohn, R. V. & Müller, S. (1992): *Branching of twins near an austenite-twinned-martensite interface*, in: Philosophical Magazine A, Volume 66, 697–715.

Kratochvil, J. & Sedlacek, R. (2004): *Energetic approach to subgrain formation*, in: Materials Science and Engineering, Volume A, 387-389, 67–71.

Lee, E. H. (1969): *Elastic-Plastic Deformations at Finite Strains*, in: ASME, Journal of Applied Mechanics, Volume 36, 1–6.

Lee, M. G., Lim, H., Adams, B. L., Hirth, J. P. & Wagoner, R. H. (2010): *A dislocation density-based single crystal constitutive equation*, in: International Journal of Plasticity, Volume 26, 925–938.

Lenhart, R. E. (1955): *The relationship of hardness measurments to the tensile and compression flow curves*, Technical Report 114, Wright Air Development Center, Ohio - USA, 1955.

Levesque, J., Inal, K., Neale, K. W. & Mishra, R. K. (2010): *Numerical modeling of formability of extruded magnesium alloy tubes*, in: International Journal of Plasticity, Volume 26, 65–83.

Levitas, V. I. (1998): *Thermomechanical theory of martensitic phase transformations in inelastic materials*, in: International Journal of Solids and Structures, Volume 35, 889–940.

Levitas, V. I. & Ozsoy, I. B. (2009): *Micromechanical modeling of stress-induced phase transformations. Part 1. Thermodynamics and kinetics of coupled interface propagation and reorientation*, in: International Journal of Plasticity, Volume 25, 239–280.

Li, B. & Ma, E. (2009): *Zonal dislocations mediating* $\{10\bar{1}1\}\langle 10\bar{1}\bar{2}\rangle$ *twinning in magnesium*, in: Acta Materialia, Volume 57, 1734–1743.

Lilleodden, E. (2010): *Microcompression study of Mg (0 0 0 1) single crystal*, in: Scripta Materialia, Volume 62, 532–535.

Lubliner, J. (1972): *On the Thermodynamic Foundation of Non-linear Solid Mechanics*, in: International Journal of Non-linear Mechanics, Volume 7, 237–254.

Lubliner, J. (1997): *Plasticity Theory*, Maxwell Macmillian International Edition 1997.

Luenberger, D. (1984): *Linear and Nonlinear Progrmming*, Addison-Wesley MA 1984.

Mandel, J. (1972): *Plasticite Classique et Viscoplasticite*, Cours and Lectures au CISM No. 97, International Center for Mechanical Science, Springer-Verlag New York 1972.

Mathis, K., Nyilas, K., Axt, A., Dragomir-Cernatescu, I., Ungar, T. & Lukac, P. (2004): *The evolution of non-basal dislocations as a function of deformation temperature in pure magnesium determined by X-ray diffraction*, in: Acta Materialia, Volume 52, 2889–2894.

McGinty, R. D. & McDowell, D. L. (2006): *A semi-implicit integration scheme for rate independent finite crystal plasticity*, in: International Journal of Plasticity, Volume 22, 996–1025.

Meggyes, A. (2001): *Multiple decomposition in finite deformation theory*, in: Acta Mechanica, Volume 146, 169–182.

Mendelson, S. (1970): *Dislocation Dissociations in hcp Metals*, in: Journal of Applied Physics, Volume 41, 1893–1910.

Miehe, C. (2002): *Strain-driven homogenization of inelastic microstructures and composites based on an incremental variational formulation*, in: International Journal for Numerical Methods in Engineering, Volume 55, 1285–1322.

Miehe, C., Apel, N. & Lambrecht, M. (2002): *Anisotropic additive plasticity in the logarithmic strain space: modular kinematic formulation and implementation based on incremental minimization principles for standard materials.*, in: Computer Methods in Applied Mechanics and Engineering, , 191, 5383–5425.

Miehe, C. & Lambrecht, M. (2003): *A two-scale finite element relaxation analysis of shear bands in non-convex inelastic solids: small-strain theory for standard dissipative materials*, in: International Journal for Numerical Methods in Engineering, Volume 58, 1–41.

Mielke, A. (2004): *Deriving new evolution equations for microstructures via relaxation of variational incremental problems*, in: Computer Methods in Applied Mechanics and Engineering, Volume 193, 5095–5127.

Mielke, A., Theil, F. & I., L. V. (2002): *A Variational Formulation of Rate-Independent Phase Transformations Using an Extremum Principle*, in: Archive for rational mechanics and analysis, Volume 162, 137–177.

Morrey, C. B. (1952): *Quasi-Convexity and the Lower Semicontinuity of Multiple Integrals*, in: Pacific Journal of Mathematics, Volume 2, 25–53.

Morris, J. R., Ye, Z. & Yoo, M. H. (2005): *First-principles examination of the twin boundary in hcp metals*, in: Philosophical Magazine, Volume 85, 2, 233–238.

Mosler, J. (2007): *On the numerical modeling of localized material failure at finite strains by means of variational mesh adaption and cohesive elements*, D-44780 Bochum 2007, Dissertation, Ruhr-Universität Bochum.

Mosler, J.: *Lecture notes on Engineering Mechanics*, Kiel Universität - Germany, 2008.

Mosler, J. & Bruhns, O. T. (2009a): *On the implementation of variational constitutive updates at finite strain*, in: Hackl, K. (Ed.): *Variational Concepts with Application to the Mechanics of Materials*, Springer 2009, in press.

Mosler, J. & Bruhns, O. T. (2009b): *Towards variational constitutive updates for non-associative plasticity models at finite strain: models based on a volumetric-deviatoric split*, in: International Journal of Solids and Structures, Volume 49, 1676–1685.

Mosler, J. & Cirak, F. (2009): *A variational formulation for finite deformation wrinkling analysis of inelastic membranes*, in: Computer Methods in Applied Mechanics and Engineering, Volume 198, 2087–2098.

Mueller, S. (1999): *Variational models for microstructure and phase transitions*, in: Calculus of Variations and Geometric Evolution Problems, Volume 1713, 85–210.

Obara, T., Yoshinga, H. & Morozumi, S. (1973): {*11-22*} {*-1-123*} *Slip system in magnesium*, in: Acta Metallurgica, Volume 21, 845–853.

Orowan, E. (1934): *Zur kristallplastizität III. Über den mechanismus des gleitvorganges*, in: Zeitschrift für Physik, Volume 89, 634–659.

Orowan, E. (1954): *Dislocation in Metals*, AIME New York 1954.

Ortiz, M. & Repetto, E. A. (1999): *Nonconvex energy minimization and dislocation structures in ductile single crystals*, in: Journal of the Mechanics and Physics of Solids, Volume 47, 397–462.

Ortiz, M., Repetto, E. A. & Stainier, L. (2000): *A theory of subgrain dislocation structures*, in: Journal of the Mechanics and Physics of Solids, Volume 48, 2077–2114.

Ortiz, M. & Stainier, L. (1999): *The variational formulation of viscoplastic constitutive updates*, in: Computer Methods in Applied Mechanics and Engineering, Volume 171, 419–444.

Peach, M. O. & Köhler, J. S. (1950): *The force exerted on dislocations and the stress fields produced by them*, in: Physical Review, Volume 80, 436–439.

Pedregal, P. (1993): *Laminates and microstructure*, in: European Journal of Applied Mathematics, Volume 4, 121–149.

Peirce, D., Asaro, R. J. & Needleman, A. (1982): *An analysis of nonuniform and localized deformation in ductile single crystals*, in: Acta Metallurgica, Volume 30, 1087–1119.

Perez, N. (2004): *Fracture mechanics*, Kluwer Academic Publishers USA 2004.

Petryk, H., Fischer, F. D., Marketz, W., Clemens, H. & Appel, F. (2003): *An Energy Approach to the Formation of Twins in TiAl*, in: Metallurgical and Materials Transactions, Volume 34, 2827–2836.

Pitteri, M. (1985): *On the kinematics of mechanical twinning in crystals*, in: Archive for Rational Mechanics and Analysis, Volume 88, 25–57.

Polanyi, M. (1934): *Gitterstörung die einen kristall plastisch machen könnte*, in: Zeitschrift für Physik, Volume 89, 660–664.

Price, P. B. (1960): *On the growth of cadmium crystals from the vapour*, in: Philosophical Magazine, Volume 5, 473–484.

Proust, G., Tome, C. N., Jain, A. & Agnew, S. R. (2009): *Modeling the effect of twinning and detwinning during strain-path changes of magnesium alloy AZ31*, in: International Journal of Plasticity, Volume 25, 861–880.

Rajagopal, K. R. & Srinivasa, A. R. (1995): *On the inelastic behavior of solids – Part 1: Twinning*, in: International Journal of Plasticity, Volume 11, 653–678.

Raoult, A. (2010): *Quasiconvex envelopes in nonlinear elasticity*, Springer Wien-NewYork 2010, Volume 516 of *CISM Courses and Lectures*, pp. 17–52.

Rasmussen, K. & Pedersen, O. (1980): *Fatigue of copper polycrystals at low plastic strain amplitudes*, in: Acta Metallurgica, Volume 28, 1467–1478.

Reed-Hill, R. E. (1960): in: Transactions of the Metallurgical Society of AIME, Volume 2I8, 554–558.

Reed-Hill, R. E. & Robertson, W. D. (1957a): *Additional modes of deformation twinning in magnesium*, in: Acta Metallurgica, Volume 5, 717–727.

Reed-Hill, R. E. & Robertson, W. D. (1957b): *Deformation of magnesium single crystals by nonbasal slip*, in: Journal of Metals - Transactions AIME, Volume 220, 496–502.

Rice, J. R. (1971): *Inelastic constitutive relations for solids: an internal variable theory and its application to metal plasticity*, in: Journal of the Mechanics and Physics of Solids, Volume 19, 433–455.

Roberts, E. & Partridge, P. G. (1966): *The accomodation around* $\{10-12\} < -1011 >$ *twins in magnesium*, in: Acta Metallurgica, Volume 14, 513–527.

Rockafellar, R. T. (1970): *Convex Analysis*, Princeton University Press Princeton 1970.

Roters, F., Eisenlohr, P., Hantcherli, L., Tjahjanto, D. D. & Bieler, T. R. R. D. (2010): *Overview of constitutive laws, kinematics, homogenization and multiscale methods in crystal plasticity finite-element modeling: Theory, experiments, applications*, in: Acta Materiala, Volume 58, 1152–1211.

Saimoto, S. (1963): *Low temperature tensile deformation of copper single crystals oriented for multiple slip*, Cambridge 1963, Dissertation, M.I.T.

Salje, E. K. H., Koppensteiner, J., Reinecker, M., Schranz, W. & Planes, A. (2009): *Jerky elasticity: Avalanches and the martensitic transition in* $Cu_{74.08}Al_{23.13}Be_{2.79}$ *shape-memory alloy*, in: Applied Physics Letters, Volume 95, 2319081–3.

Schmid, E. (1924): *Yield point of crystals, Critical shear stress law*, in: *Proceedings of the First International Congress for Applied Mechanics, Delft*, 1924.

Schmidt-Baldassari, M. (2003): *Numerical concepts for rate-independent single crystal plasticity*, in: Computer Methods in Applied Mechanics and Engineering, Volume 192, 1261–1280.

Schröder, J. & Neff, P. (2010): *Poly-,Quasi and Rank-one Convexity in Applied Mechanics*, Volume 516 of *CIAM Courses and Lectures*, Springer Wien-NewYork 2010.

Siebel, G. (1939): *Magnesium und seine Legierungen*, Springer Berlin 1939.

Siegel, R. W. (1978): *Vacancy Concentrations in Metals*, in: Journal of Nuclear Materials, Volume 69-70, 117–146.

Silhavy, M. (1997): *The Mechanics and Thermodynamics of Continuous Media*, Springer, Berlin, Heidelberg, New York 1997.

Simha, N. K. (1997): *Twin and habit plane microstructures due to the tetragonal to monoclinic transformation of zirconia*, in: Journal of the Mechanics and Physics of Solids, Volume 45, 261–263.

Simo, J. C. (1998): *Numerical analysis of classical plasticity*, Volume IV of *Handbook for numerical analysis*, Elsevier Amsterdam 1998.

Simo, J. C. & Hughes, T. J. R. (1998): *Computational Inelasticity*, Springer, New York 1998.

Simo, J. C. & Pister, K. S. (1984): *Remarks on rate constitutive equations for finite deformation problems*, in: Computer Methods in Applied Mechanics and Engineering, Volume 46, 210–215.

Staroselsky, A. & Anand, L. (2003): *A constitutive model for hcp materials deforming by slip and twinning: application to magnesium alloy AZ31B*, in: International Journal of Plasticity, Volume 19, 1843–1864.

Stein, E. & Barthold, F. J. (1995): *Elastizitätstheorie*.

Stupkiewicz, S. & Petryk, H. (2002): *Modelling of laminated microstructures in stress-induced martensitic transformations*, in: Journal of the Mechanics and Physics of Solids, Volume 50, 2303–2331.

Sue, P. L. & Havner, K. S. (1984): *Theoretical-Analysis of the Channel Die Compression Test .1. General-Considerations and Finite Deformation of Fcc Crystals in Stable Lattice Orientations*, in: Journal of the Mechanics and Physics of Solids, Volume 32, 417–442.

Szczerba, M. S., Bojar, T. & Tokarski, T. (2004): *Is there a critical resolved shear stress for twinning in face-centred cubic crystals*, in: Philosophical Magazine, Volume 84, 481–502.

Taylor, G. I. (1934): *The mechanism of plastic deformation of crystals part I*, in: Proceeding of the Royal Society, Volume A145, 362–387.

Taylor, G. I. (1938): *Plastic strain in metals*, in: Journal of the Institute of Metals, Volume 62, 307–324.

Tegart, W. J. M. (1964): *Independent slip systems and ductility of hexagonal polycrystals*, in: Philosophical Magazine, Volume 9, 339–341.

Terlinde, G. & Luetjering, G. (1982): *Influence of Grain-Size and Age-Hardening on Dislocation Pile-Ups and Tensile Fracture for a Ti-Al Alloy*, in: Metallurgical Transactions a-Physical Metallurgy and Materials Science, Volume 13, 1283–1292.

Thompson, N. & Millard, D. J. (1952): *Twin Formation in Cadmium*, in: Philosophical Magazine, Volume 43, 422–440.

Timpe, A. (1905): *Probleme der Spannungsverteilung in ebenen Systemen einfach geloest mit Hilfe de Airyschen Function*, in: Zeitschrift fuer Math. und Phys., Volume 52, 348–383.

Truesdell, C. & Noll, W. (1965a): *The nonlinear field theories*, Volume 3 of *Handbuch der Physik*, Springer-Verlag Berlin 1965.

Truesdell, C. & Noll, W. (1965b): *The nonlinear field theories*, Volume 3 of *Handbuch der Physik*, Springer-Verlag Berlin 1965.

Van Houtte, P. (1978): *Simulation of the Rolling and Shear Texture of Brass by the Taylor Theory adapted for Mechanical Twinning*, in: Acta Metallurgica, Volume 26, 591–604.

Volterra, V. C. (1907): *Sur l'equilibre des Crops elastiques multiplement connexes*, in: Annales Scientifiques De L'E.N.S., Volume 24, 401–517.

Wang, J., Hoagland, R. G., Hirth, J. P., Capolungo, L., Beyerlein, I. J. & Tome, C. N. (2009): *Nucleation of a $(\bar{1}012)$ twin in hexagonal close-packed crystals*, in: Scripta Materialia, Volume 61, 903–906.

Weingarten, G. (1901): *Sulle Superficie di discontinuita nella teoria della elasticita dei corpi Solidi*, in: Rend. Roma Acc. Linc., Volume 5, 57.

Wonsiewicz, B. C. & Backofen, W. A. (1967): *Independent slip systems and ductility of hexagonal polycrystals*, in: Transaction of Metallurgical Soc. AIME, Volume 239, 1422–1433.

Xiao, H., Bruhns, O. T. & Meyers, A. (2006): *Elastoplasticity beyond small deformations*, in: Acta Mechanica, Volume 182, 31–111.

Yoo, M. H. (1981): *Slip, Twinning, and Fracture in Hexagonal Close-Packed Metals*, in: Metallurgical Transactions, Volume 12, 409–418.

Yoo, M. H., Morris, J. R., Ho, K. M. & Agnew, S. R. (2002): *Nonbasal Deformation Modes of HCP Metals and Alloys: Role of Dislocation Source and Mobility*, in: Metallurgical and Materials Transactions A, Volume 33, 813–822.

Yoshida, K., Yamamoto, M., Gotoh, Y. & Onozuka, T. (1968): *Plastic Deformation of Copper and Iron Whiskers*, in: Transactions of the Japan Institute of Metals, Volume 9, 863.

Yoshinaga, H. & Horiuchi, R. (1963): *On the nonbasal slip in magnesium crystals*, in: Transactions of the Japan Institute of Metals, Volume 5, 14–21.

Yu, D. Y. W. & Spaepen, F. (2004): *The yield strength of thin copper films on Kapton*, in: Journal of Applied Physics, Volume 95, 2991–2997.

Yu, Q., Shan, Z. W., Huand, X., Xiao, L., Sun, J. & Ma, E. (2009): *Strong crystal size effect on deformation twinning*, in: Nature, Volume 463, 335–338.

Zamiri, A., Pourboghrat, F. & Barlat, F. (2007): *An effective computational algorithm for rate-independent crystal plasticity based on a single crystal yield surface with an application to tube hydroforming*, in: International Journal of Plasticity, Volume 23, 1126–1147.

Zupan, M. & Hemker, K. J. (2003): *Yielding behavior of aluminum-rich single crystalline γ-TiAl*, in: Acta Materialia, Volume 51, 6277–6290.